University of California
Santa Barbara

# Soft Matter in Motion: 3D Active Nematics, Active Phase Separations and Vesicle Closure

A dissertation submitted in partial satisfaction
of the requirements for the degree

Doctor of Philosophy
in
Physics

by

Raymond Adkins

Committee in charge:

Professor Zvonimir Dogic, Chair
Professor M. Cristina Marchetti
Professor Sebastian Streichan

June 2023

The Dissertation of Raymond Adkins is approved.

---

Professor M. Cristina Marchetti

---

Professor Sebastian Streichan

---

Professor Zvonimir Dogic, Committee Chair

May 2023

Soft Matter in Motion: 3D Active Nematics, Active Phase Separations and Vesicle Closure



by

Raymond Adkins

To my wife, Elvia.

## Acknowledgements

I would like to thank my advisor, Prof. Zvonimir Dogic, who has been an supportive mentor throughout my PhD. He has helped to guide me through the work presented here, taught me essential scientific skills, and supported my curiosity. I am grateful to have had the opportunity to have worked in his lab. I am also thankful to the rest of the Dogic lab, who together have made an excellent work environment, and who I have enjoyed learning from and collaborating with.

This thesis is the result of work with several collaborators, who I am extremely thankful for the opportunity to have worked with. I am grateful for Prof. Cristina Marchetti, Prof. Sebastian Streichan, Prof. Tom Powers, Prof. Gualliume Duclos, Prof. Dan Beller and their students. Without them, the work presented in this thesis would not have been possible.

Thanks to Dr. Chuck Rosenblatt, who supported and mentored me through my undergraduate years. Thanks also to Jim Beil, whose engaging teaching at Lorain County Community College first sparked my interest in science. I am thankful to Robby Nadler, who has spent many hours providing critical feedback on my writing.

# Curriculum Vitæ

Raymond Adkins

## Education

| | |
|---|---|
| 2023 | Ph.D. in Physics (Expected), University of California, Santa Barbara. |
| 2018 | M.S. in Physics, Case Western Reserve University. |
| 2018 | B.S. in Physics, Case Western Reserve University. |

## Awards and Honors

| | |
|---|---|
| 2023 | Schmidt Science Fellowship |
| 2022 | Fionna and Michael Goodchild Graduate Mentoring Award, University of California Santa Barbara |
| 2019-2022 | National Science Foundation Graduate Research Fellowship |
| 2018 | Guenter Ahlers Fellowship, University of California Santa Barbara |
| 2018 | The Polykarp Kusch Prize, Case Western Reserve University |
| 2017 | The Albert A. Michelson Prize, Case Western Reserve University |

## Publications

R. Adkins[†], I. Kolvin[†], Z. You[†], S. Witthaus, M. C. Marchetti and Z. Dogic. Dynamics of active liquid interfaces. *Science*, **377**, (2022).

J. Colen, M. Han, et. Al. Machine learning active-nematic hydrodynamics. *PNAS*, **118**, (2021).

P. Corona, K. Silmore, R. Adkins, et. Al. Bayesian estimations of orientation distribution functions from small-angle scattering *Phys. Rev. Mat.*, **5**, (2021).

G. Duclos[†], R. Adkins[†], D. Banerjee et. Al. Topological structure and dynamics of three-dimensional active nematics. *Science*, **367**, (2020).

R. Adkins[†], E.M. Shelton[†], M. C. Renoult, P. Carles and C. Rosenblatt. Interface Coupling and growth rate measurements in multilayer Rayleigh-Taylor instabilities. *Phys. Rev. Fluids*, **2**, 062001 (2017).

O. Cohen, A. J. Ferris, R. Adkins, R. P. Lemieux, D. Avnir, D. Gelman and C. Rosenblatt. Chiral organosilica particles and their use as inducers of conformational deracemization of liquid crystal phases. *Chem. Phys. Lett.*, **696**, (2017).

[†] Indicates co-first author.

**Abstract**

Soft Matter in Motion: 3D Active Nematics, Active Phase Separations and Vesicle Closure

by

Raymond Adkins

The field of soft matter seeks to understand materials which easily deform in response to applied stresses. Several systems have served as foundational models in soft matter, including liquid crystals, liquid phase separations and membranes. In this thesis, I investigated the dynamics of these classic soft materials, by building and characterizing new several model systems.

First, I detail initial work on a 3D active nematic. I doped a three-dimensional liquid crystal with biologically-based active filaments that produced turbulent-like mixing of the material. These chaotic flows generated neutral disclination lines, which we show behave in accordance with nematic hydrodynamic models.

Next, I developed a model system to study an actively-driven liquid-liquid phase separations. This system consisted of an active phase that contained microtubule bundles, and a passive phase, separated by a soft interface. The active bundles generated stresses that resulted in complex interfacial dynamics. We used this system to measure values of the active stress generated by the microtubule bundles, a defining measurement that has eluded the field.

Lastly, I quantitatively studied vesicle formation using colloidal membranes as a model system. I observed the transformation from a flat membrane to a closed vesicle via a gravity-assisted pathway. Subsequently, I showed that the shape change accompanying vesicle closure can be understood by minimizing the elastic energy. Additionally, I

investigated membrane disassembly caused by continuous vesicle shrinking. I demonstrated that the shape change dynamics associated with vesicle shrinking followed an energy-minimizing pathway through the area-dependent energy landscape.

# Contents

# Chapter 1

# Introduction

Soft materials easily deform in response to applied stresses. In these systems, dynamics occur at low energy scales, comparable to thermal energy at room temperature. Examples of soft matter range from everyday systems like liquid interfaces, soap bubbles, and polymer suspensions, to more unusual materials like liquid crystals. Many biological building blocks including DNA, proteins and cell membranes, can form soft materials. Importantly, these biological examples exist in a non-equilibrium environment, where they are actively mixed or undergoing large-scale shape change.

This dissertation describes my research developing and characterizing several biologically-based soft materials that are driven out of equilibrium either by internal drive of external forces. Chapter 2 discusses the structure and interactions of topological defects that arise in a three-dimensional active nematic. Chapter 3 describes an active liquid-liquid phase separation that we used to measure the stress generated by the microtubule-based active fluid. Finally, Chapter 4 introduces a new model system for studying vesicles formation, and investigates pathways of topological transformation as flat colloidal membranes close into vesicles. To establish proper background, concepts of soft and active matter as well as membrane physics must be introduced.

## 1.1 Background

### 1.1.1 Nematic liquid crystals

One of the most commonly studied systems in soft matter is the nematic liquid crystal. A nematic comprises of anisotropic molecules, which locally align with their neighbors along an axis called the 'director'. Nematics are head-tail symmetric, and lack positional order between molecules.

The long-range orientational order in a nematic is disrupted by singularities, called topological defects, where the director field winds around a single point. In 2D nematics, topological defects are characterized by their topological charge; the number of counter-clockwise rotations of the director field that encircles the defect. These defects take on a number of half integer rotations and can be positive or negative. At the cost of increased in elasitc distortion energy, defects can nucleate in pairs from an aligned background, if the sum of their topological charge is zero 1.1.

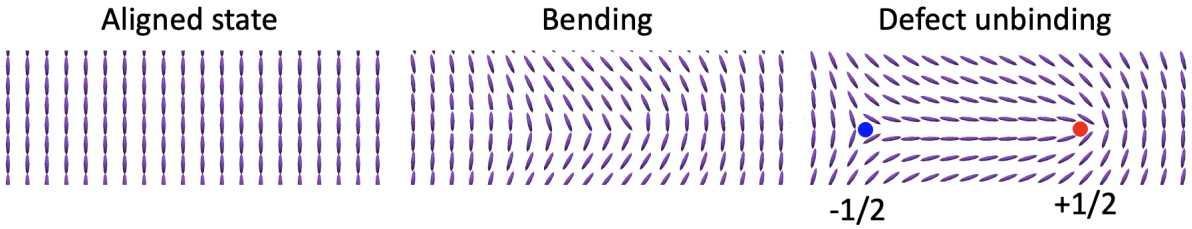


Figure 1.1: **Schematic of defect pair unbinding** A pair of $+1/2$ and $-1/2$ defects are able to unbind from an originally aligned state.

Liquid crystals have become a foundational model system in soft matter. Models of how rod-like particles with excluded volume interactions spontaneously form nematic liquid crystals began over 70 years ago [1]. A significant amount of work has studied how various molecular structure induce increasingly more complex phases [2, 3, 4, 5], and how liquid crystalline order alters hydrodynamics [6, 7, 8]. A section of this dissertation will introduce a model system for studying the dynamics of a 3D nematic liquid crystal made

from from biological components, which generates its own spontaneous flows by locally consuming energy microscopic motors. We will preform the first study of the structure and interactions of topological defects in 3D, and compare with hydrodynamic models and simulations.

### 1.1.2 Liquid phase separation

Liquid-liquid phase separations (LLPS) are a phenomena where a homogeneous solution separates into two fluids. One such example which is common to everyday experience is a mixture of oil and water. When mixed together, oil and water rapidly demix into two bulk liquid phases, separated by an interface. Similar LLPS occur in polymer-polymer and polymer-salt mixtures.

Recently, LLPS have been shown to be a fundamental organizing principle in cells. These 'membraneless organelles' are collections of proteins and RNA that phase separate from the cytoplasm, to localizing proteins and regulate genes [9, 10]. These LLPS exist in the highly dynamic environment of the cytoplasm, and are acted on by cellular forces, which alter the phase separation dynamics [11]. In this dissertation, I explore the dynamics of LLPS which undergo a stress applied by active microtubule bundles, as a model to study the general physics of out-of-equilibrium LLPS.

### 1.1.3 Filamentous phages

Filamentous phages are semi-flexible rod-like viruses, composed of coat proteins packed around a loop of single-stranded DNA. One commonly studied wild-type phage, fd-wt, is 6.6 nm wide, 880 nm long and has a persistence length of several microns [12]. This makes fd-wt, and other filamentous phages, ideal hard-rod colloids. At low concentration, these rods form an isotropic phase with uniformly distributed orientations. As

the concentration of phages increases, the virus transitions to a nematic phase, making filamentous phages an excellent model to study liquid crystals [13].

### 1.1.4 Colloidal membranes

Tuning the intermolecular forces between filamentous phages can be used to produce self-assembled structures. Phages are negatively charged, causing particles to electrostatically repel each other. To produce self-assembled structures, we screen these charges by adding salt. An attractive force can be induced by the addition of a depleting polymer [Fig. 1.2A]. Together, this causes phages to latterly align and condense into flat disks having a thickness equal to the length of the virus and with a interparticle spacing of several nanometers [14] [Fig. 1.2B].

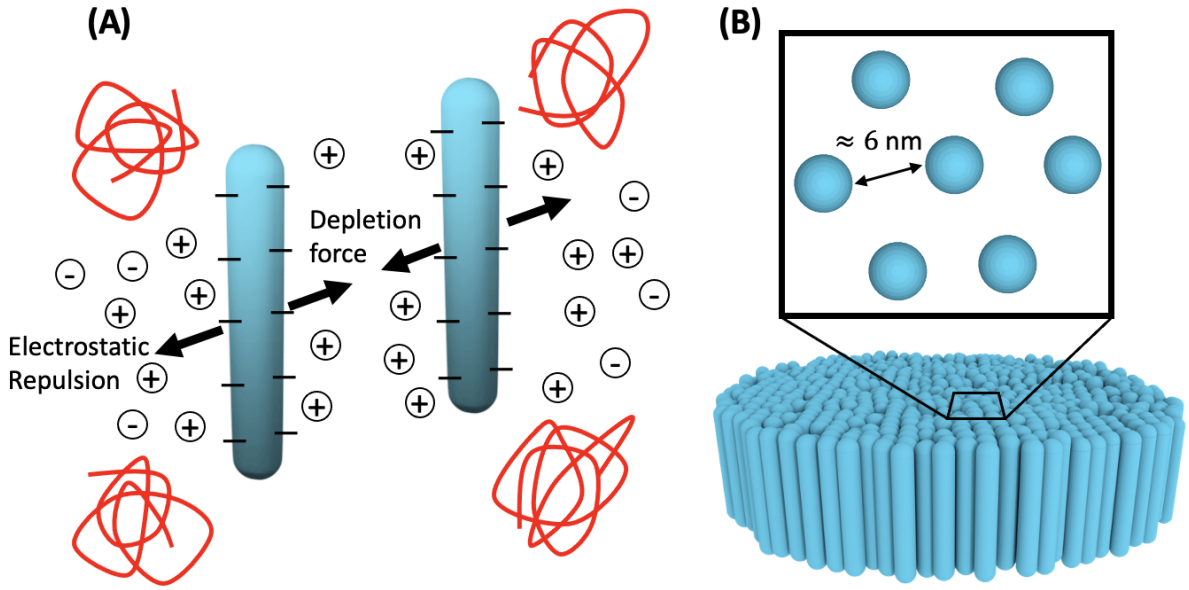


Figure 1.2: **Schematic of colloidal membrane formation.** (**A**) In the presence of salt and a depletant, phages align and attract. (**B**) Groups of thouands of phages organize into a flat disk with an interparticle spacing of several nanometers.

The resulting membranes are 2D fluid sheets which are described using the Helfrich Hamiltonian, exactly like lipid membranes [15, 14, 16]. However, colloidal membranes

are $\approx 1\mu m$ in thickness and are hundreds of microns in diameter. These length and time scales are orders of magnitude larger than lipid membranes, enabling high-resolution imaging and quantitative study of membrane dynamics. Additionally, genetic engineering techniques can be used to change the physical properties of the phages to adjust the energy landscape of the membranes, to produce various self-assembled structures like catenoids, membranes containing rafts and sponge phases [17, 18]. In this dissertation, we leverage the size and control over colloidal membranes to study colloidal vesicle formation.

## 1.2 Active matter

The field of active matter studies materials comprising energy-consuming motile components. Examples of active systems are animal flocks, dense bacterial suspensions and driven colloidal particles [19, 20, 21, 22, 23]. The unifying feature of all these systems is that each are made of components that consume energy to produce motion. This motion of constituent objects cascades up length scales, resulting in large scale dynamics. For example, the flocking motion of starlings can be modeled as particles that interact through nearest neighbor interactions [24, 20, 23]. However, generic modeling of active systems remains a significant challenge. Because of the immense number of components in these systems, predicting how they self-organize is difficult. Further, the local energy consumption precludes any understanding from equilibrium statistical mechanics.

To progress toward understanding these systems, several well-controlled active materials have been developed. These systems are either synthetic, like driven colloidal particles [22, 25, 26], or based on biological components, like reconstituted protein mixtures [27, 28, 29, 30]. Being simpler than biological systems, synthetic systems are more straightforward for making direct comparison with models. On the other hand, while biologically-based systems have direct relevance to biological systems. The work pre-

sented in this dissertation consist entirely of biologically-based materials.

### 1.2.1 Microtubule-based active matter

In this dissertation, we study active materials based on cytoskeletal proteins. The cytoskeleton is a network of filamentous proteins which gives the cell structure, and enables cell motility. One major cytoskeletal component are microtubules, which are filaments formed by repeating dimers of $\alpha$ and $\beta$ tubulin. These dimers assemble into a polarized hollow filament that is 22 nm in diameter. Microtubules polymerize by hydrolyzing Guanosine Triphosphate (GTP) as dimers are added to the filament, while periodically undergoing 'catastrophe', which are periods of rapid shortening. In our system, we have stabilized microtubules to prevent catastrophe using the non-hydrolyzable GMPCPP in place of GTP.

The motion of microtubule-based active matter system is driven by molecular motor proteins. Kinesin-1 is one of the most well studied molecular motors, having been the subject of single molecule studies for decades [31, 32, 33]. Kinesin-1 molecular motors consist of a cargo domain at one end and a head domain that binds to and walks along microtubules at the other end, connected together by a long flexible stalk. These motors hydrolyze Adenosine Triphosphayte (ATP) to step hand-over-hand in 8 nm steps [34].

To form microtubule-based active matter, we use kinesin motor clusters (KSA). We start with Kinesin-1 which have been modified to keep their first 401 amino acids, and have been fused to a biotin-binding domain [Fig. 1.3A] [35]. This biotin conjugates are connected with streptavidin tetramer, so that pairs of kinesin motors bind end-to-end, with their heads facing outward. Kinesin-streptavidin motor clusters bind to multiple microtubules and walk along each producing a relative sliding force. Adding a depletant induces an entropic attraction between pairs of microtubules, producing bundles that

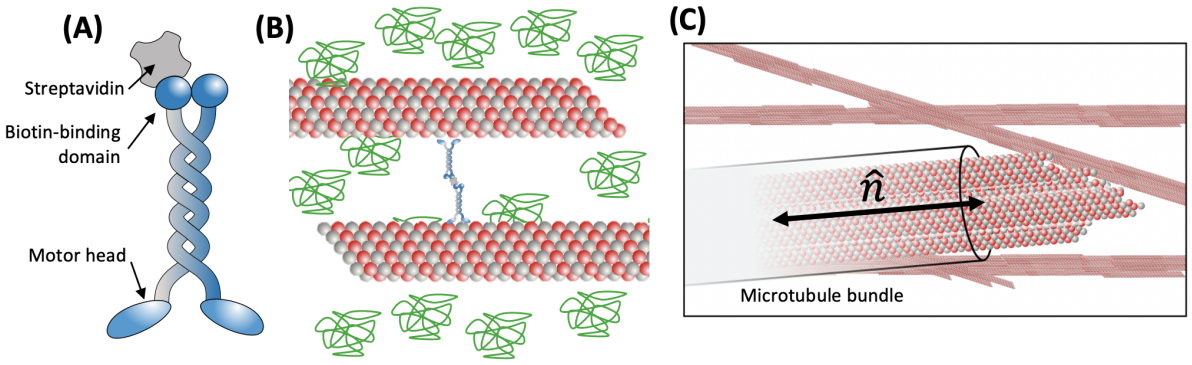


Figure 1.3: **Schematic of active microtubule bundles.** (**A**) Kinesin used in microtubule-based active matter. Dimers of the truncated motor protein k401, bound to streptavidin. (**B**) The polymer depletant (green) entropically drives microtubules to together. Kinein motor clusters attach to and walk along pairs of microtubules, causing extension of large-scale bundles (**C**) containing many hundreds of mictotubules.

containing hundreds of microtubules and KSA clusters [Fig. 1.3B,C]. The collective motion of these motors causes the entire bundle to extend, bend and fracture. On the millimeter length scale, the motion of the microtubule bundles leads to turbulent-like dynamics [29, 36, 37].

## 1.3 Scope of the dissertation

Having reviewed the main topics, we are able to outline the main results described in this dissertation. Chapter 2 discuses the development and characterization of a model system for studying three dimensional active nematics [38]. We construct a three-dimensional nematic using filamentous phages, and disperse active microtubule bundles throughout the solution, which renders it active. The system is imagd using light-sheet microscopy, a technique common in developmental biology [39]. We characterize the system by studying the structure and interactions of the topological disclinations that arise in three-dimensions as a result of active flows.

Chapter 3 is based on work in [40], and details the development of an active liquid-

liquid phase separation (active-LLPS). The active-LLPS is formed by combining a well characterized polymer-based phase separation with active microtubule bundles. The polymer mixture separates into two phases, separated by a soft interface, with the active bundles segregated to one phase. The turbulent motion of the active bundles drives deformations of the interface, resulting in a range of dynamics which depend on the sample geometry. Active-LLPS provides a means to quantify active stresses generated by microtubule bundles, a defining measurement that has long eluded the field.

Chapter 4 discusses colloidal membranes that spontaneously close to form colloidal vesicles. We detail the development of this system, first studying a pathway of gravity-assisted vesicle closure. Initially curved membranes are suspended and pulled by gravity to form tether-like structures, which then tear and close into a vesicle. We derive a model for the dynamics of vesicle shape, and show that it agrees with the observed membrane shape, with no free parameters. We then study the shape change which occurs during vesicle shrinking by induced evaporation. As vesicles shrink, the energy landscape leads to shape change, eventually causing the vesicles to revert back into a flat membrane. We show that the observed shape change can be understood as the instantaneous positions of the minima in the energy landscape of the shrinking vesicle. This framework gives a simple mechanism to understand the complex observed shape changes.

# Chapter 2

# Topological defects in three dimensional active nematics

Topological structures are effective descriptors of the nonequilibrium dynamics of diverse many-body systems. For example, motile, point-like topological defects capture the salient features of two-dimensional active liquid crystals composed of energy-consuming anisotropic units. We dispersed force-generating microtubule bundles in a passive colloidal liquid crystal to form a three-dimensional active nematic. Light-sheet microscopy revealed the temporal evolution of the millimeter-scale structure of these active nematics with single-bundle resolution. The primary topological excitations are extended, charge-neutral disclination loops that undergo complex dynamics and recombination events. Our work suggests a framework for analyzing the nonequilibrium dynamics of bulk anisotropic systems as diverse as driven complex fluids, active metamaterials, biological tissues, and collections of robots or organisms.

## 2.1 Introduction

The sinuous change in the orientation of birds flocking is a common but startling sight. Even if one can track the orientation of each bird, making sense of such large datasets is difficult. Similar challenges arise in disparate contexts from magnetohydrodynamics [41] to turbulent cultures of elongated cells [19], where oriented fields coupled to velocity undergo complex dynamics. To make progress with such extensive three-dimensional (3D) data, it is useful to identify effective degrees of freedom that allow a coarsegrained description of the collective nonequilibrium phenomena. Promising candidates are singular field configurations locally protected by topological rules [42, 43, 44, 45, 46, 47, 48]. Examples of such singularities in 2D are the topological defects that appear at the north and south poles when covering the Earth's surface with parallel lines of longitude or latitude. These point defects are characterized by the winding number of the corresponding orientation field.

The quintessential systems with orientational order are nematic liquid crystals, which are fluids composed of anisotropic molecules. In equilibrium, nematics tend to minimize energy by uniformly aligning their anisotropic constituents, which annihilates topological defects. By contrast, in active nematic materials, which are internally driven away from equilibrium, the continual injection of energy destabilizes defect-free alignment [49, 50]. The resulting chaotic dynamics are effectively represented in 2D by point-like topological defects that behave as self-propelled particles [51, 52, 37, 53, 54]. The defect-driven dynamics of 2D active nematics have been observed in many systems ranging from millimeter-sized shaken granular rods and micrometer-sized motile biological cells to nanoscale motor-driven biological filaments [29, 55, 56, 57, 58, 27, 59] . Several obstacles have hindered generalizing topological dynamics of active nematics to 3D. The higher dimensionality expands the space of possible defect configurations. Discriminating

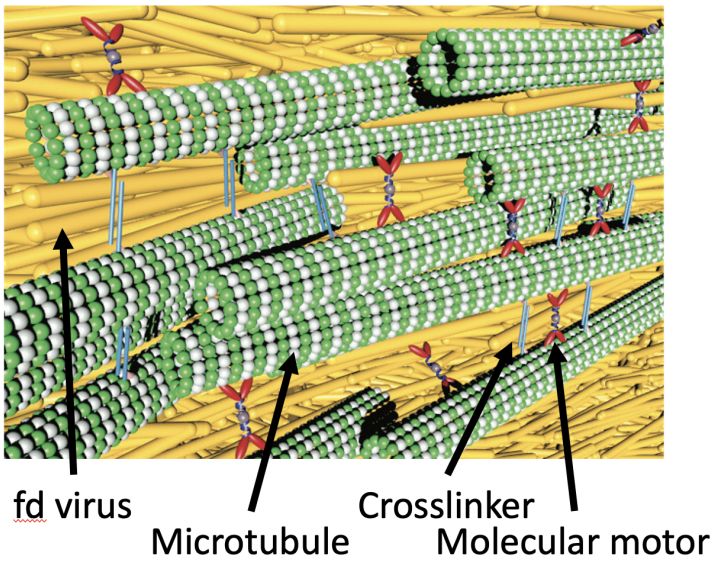


Figure 2.1: Schematic of 3D nematic system. Active microtubule bundles are dispersed in a passive colloidal liquid crystal.

between different defect types requires measurement of the spatiotemporal evolution of the director field on macroscopic scales using materials that can be rendered active away from surfaces.

## 2.2 Experimental system

The 3D active nematics that we assembled are based on microtubules and kinesin molecular motors. In the presence of a depleting agent, these components assemble into isotropic active fluids that exhibit persistent spontaneous flows [29]. Replacing a broadly acting depletant with a specific microtubule cross-linker, PRC1-NS, enabled assembly of a composite mixture of low-density extensile microtubule bundles ($\approx 0.1$ % volume fraction) and a passive colloidal nematic based on filamentous viruses [Fig. 2.1], a strategy that is similar to work on the living liquid crystal [58]. Adenosine 5'-triphosphate (ATP)–fueled stepping of kinesin motors generates microtubule bundle extension and active stresses that drive the chaotic dynamics of the entire system.

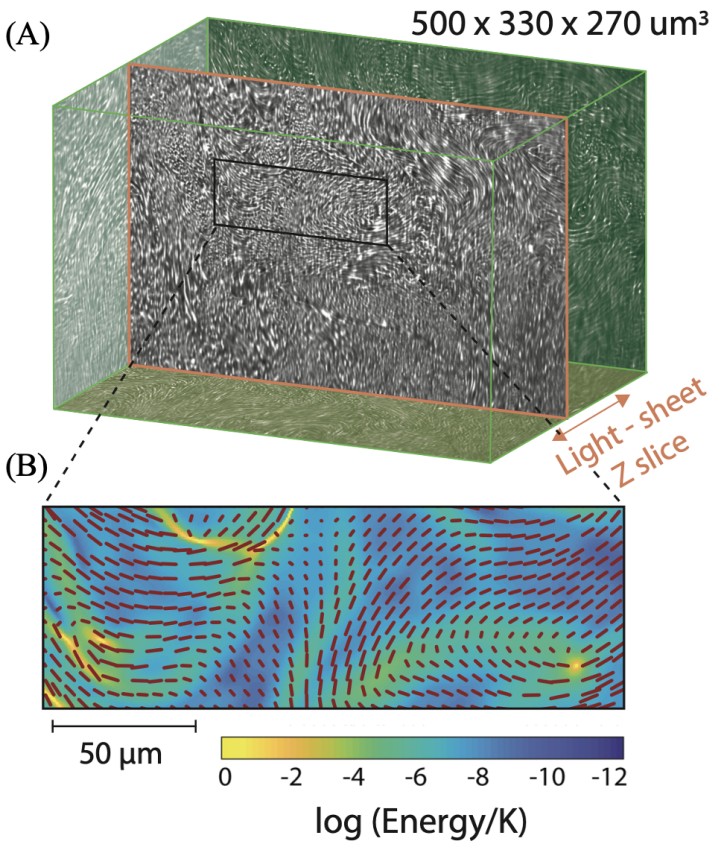


Figure 2.2: **3D nematic volume with director field.** (**A**) Multi-view light sheet microscopy allows for 3D imaging of millimeter sized samples with single-bundle resolution. (**B**) A 2D slice of the elastic distortion energy map, with an overlaid nematic director field (red).

Elucidating the spatial structure of a 3D active nematic requires measurement of the nematic director field on scales from micrometers to millimeters. Furthermore, uncovering its dynamics requires acquisition of the director field with high temporal resolution. To overcome these constraints, we used a multiview light sheet microscope [Fig. 2.2A] [39]. The spatiotemporal evolution of the nematic director field $n(x, y, z, t)$ was extracted from a stack of fluorescent images using the structure tensor method. Spatial gradients of the director field identified regions with large elastic distortions [Fig. 2.2B]. Three-dimensional reconstruction of such maps revealed that large elastic distortions mainly formed curvilinear structures, which could either be isolated loops or belong

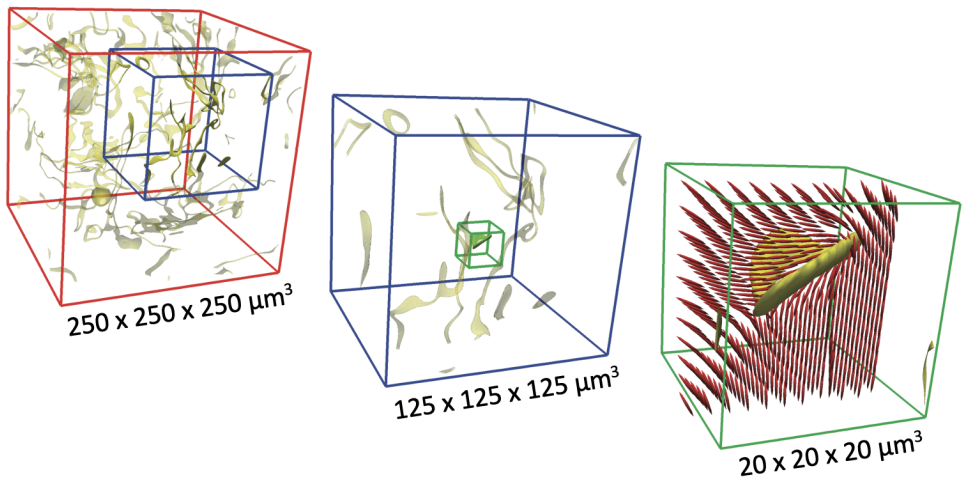


Figure 2.3: Thresholding the three-dimensional elastic distortion reveals curvilinear defects (left). Sequentially zooming in on the entangled network of lines reveals isolated loop defects (right). A slice of the orientation field (red) shows high nematic distortion near the loop defect.

to a complex network of system-spanning lines [Fig. 2.3]. These curvilinear distortions are topological disclination lines characteristic of 3D nematics. Similar structures were observed in numerical simulations of 3D active nematic dynamics using either a hybrid lattice Boltzmann method or a finite difference Stokes solver numerical approach.

## 2.3 Characterization of topological defect

Reducing the ATP concentration slowed down the chaotic flows, which revealed the temporal dynamics of the nematic director field. In turn, this identified the basic events governing the dynamics of disclination lines. We focused on characterizing the closed loop disclinations because they are the objects seen to arise or annihilate in the bulk. Isolated loops nucleated and grew from undistorted, uniformly aligned regions [Fig. 2.4A, figs. A.5.3 and A.2]. Likewise, loops also contracted and self-annihilated, leaving behind a uniform region [Fig. 2.4B, figs. A.5.3 and A.2]. Furthermore, expanding loops frequently encountered and subsequently merged with the system-spanning network of distortion

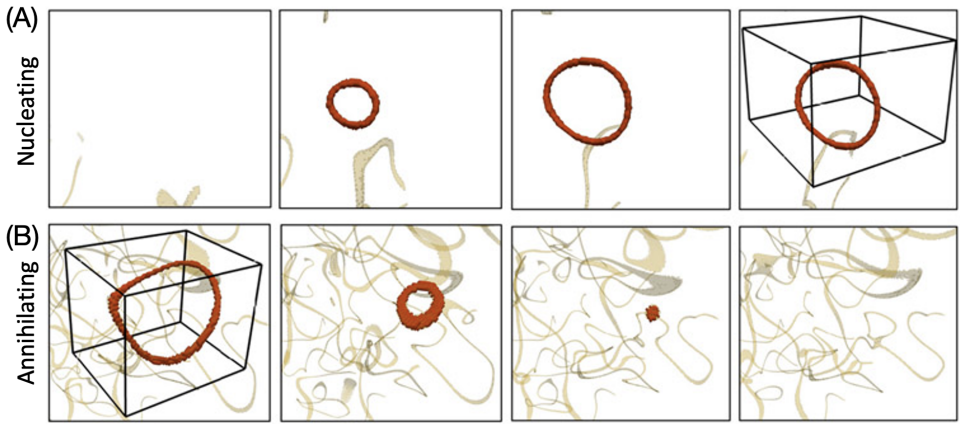


Figure 2.4: **Dynamics of experimentally observed isolated disclination loops.** (**A**) Loop nucleation from a defect-free region. (**B**) Loop self-annihilation leaves behind a defect-free nematic. Each bounding box is 30 $\mu$m x 30 $\mu$m x 38 $\mu$m. The time interval between frames is 12 seconds.

lines, whereas the distortion lines in the network self-intersected and reconnected to emit a new isolated loop [Fig. 2.5A,B; figs. A.5.3 and A.2].

Topological constraints require that topological defects can only be created in sets that are, collectively, topologically neutral. Point-like defects in 2D active nematics thus always nucleate as pairs of opposite winding number [52]. In 3D active nematics, an isolated disclination loop as a whole has two topological possibilities: It can either carry a monopole charge or be topologically neutral, depending on its director winding structure. Because charged topological loops can only appear in pairs, nucleation of isolated loops as observed in our system implies their topological neutrality.

To establish that the closed-loop distortions are nematic disclination loops with no net charge, we characterized their topological structure. In 2D nematics, point-like disclination defects are characterized by the winding number or topological charge(s). The lowest-energy disclinations have $s = \pm 1/2$, which corresponds to a $\pi$ rotation of the director field in the same sense or the opposite sense, respectively, as the traversal of any closed path encircling only the defect of interest. In 3D nematics, point-like defects from 2D systems are generalized to disclination lines, where the director similarly has

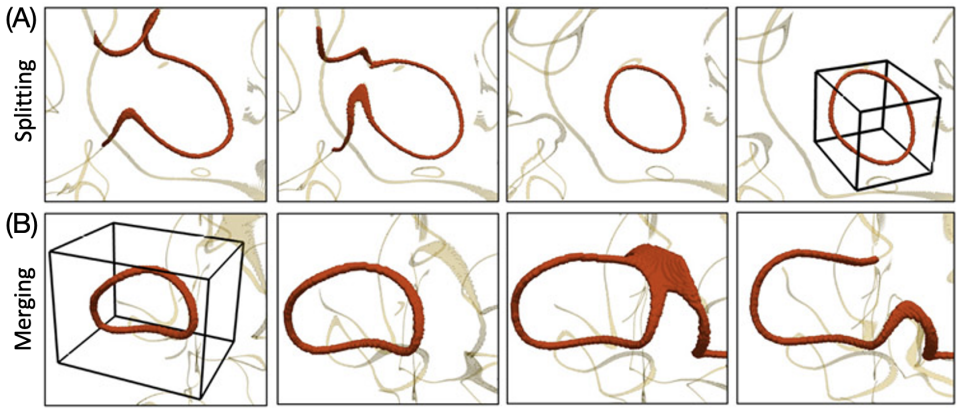


Figure 2.5: **Dynamics of experimentally observed disclination loops interacting with lines.** (**A**) A disclination line self-intersects, reconnects, and emits a loop. (**B**) A disclination loop intersects, reconnects and merges with a disclination line. Each bounding box is 30 $\mu$m x 30 $\mu$m x 38 $\mu$m. The time interval between frames is 12 seconds.

a $\pi$ winding, affording a broader variety of director configurations. We define $\mathbf{t}$ to be the disclination line's local tangent unit vector. The director field winds by $\pi$ about a direction specified by $\mathbf{\Omega}$, the rotation vector, which can make an arbitrary angle $\beta$ with $t$ [60]. If $\mathbf{\Omega}$ points antiparallel or parallel to $\mathbf{t}$, then the local director field rotates in the plane orthogonal to $\mathbf{t}$, assuming the disclination profiles familiar from 2D nematics. These configurations in which $\beta$ is equal to 0 or $\pi$ are said to have a local wedge winding [Fig. 2.6]. If $\mathbf{\Omega}$ is perpendicular to $\mathbf{t}$, then $\beta = \pi/2$ and the director forms a spatially varying angle away from the orthogonal plane, locally creating what is called a twist winding. Because $\mathbf{\Omega}$ may point in any direction relative to $\mathbf{t}$, both $\mathbf{\Omega}$ and $\beta$ can vary continuously along a disclination line.

For disclination lines forming loops, $\mathbf{\Omega}$ can vary continuously providing it returns to its original orientation upon closure, leading to a broad range of possible winding variations. A family of loops of particular relevance to 3D active nematics is characterized by a spatially uniform $\mathbf{\Omega}$, interpolating between two emblematic geometries: wedge-twist and pure-twist loops. In the wedge-twist loop, $\mathbf{\Omega}$ makes an angle $\gamma = \pi/2$ with the loop

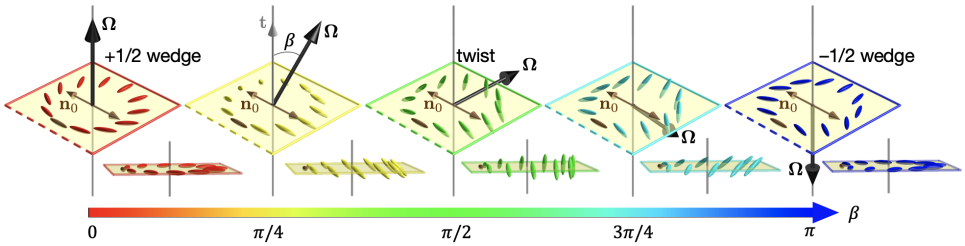


Figure 2.6: **Cross-sectional structure of disclinations** A local +1/2 wedge winding continuously transforms into -1/2 wedge through an intermediate twist winding. The director field winds by $\pi$ about the rotation vector $\Omega$ (black arrows), which makes angle $\beta$ with the tangent t, and which is orthogonal to director field everywhere in each slice. For $\pm 1/2$ wedge windings, $\beta$=0 and $\pi$. $\beta$=$\pi/2$ indicates local twist winding. Reference director $n_0$ (brown) is held fixed. The color map indicates angle $\beta$.

normal **N** [Fig. 2.7A]. As the disclination's tangent t rotates by $2\pi$ upon traveling around the loop, the angle $\beta$ varies from 0 (+1/2 wedge) to $\pi/2$ (twist), to $\pi$ (–1/2 wedge), then back to $\pi/2$, and finally returning to 0 [60, 61]. The pure-twist loop has $\mathbf{\Omega}$ uniformly parallel to **N**, so $\gamma = 0$ and $\mathbf{\Omega}$ is perpendicular to t ($\beta = \pi/2$, twist profile) at all points on the loop [Fig. 2.7B] [60, 62]. In this family of loops, the director just outside the loop, $\mathbf{n_{out}}$, is also uniform. The lack of winding of both $\mathbf{\Omega}$ and $\mathbf{n_{out}}$ implies that both wedge-twist and pure-twist loops are topologically neutral [63, 64].

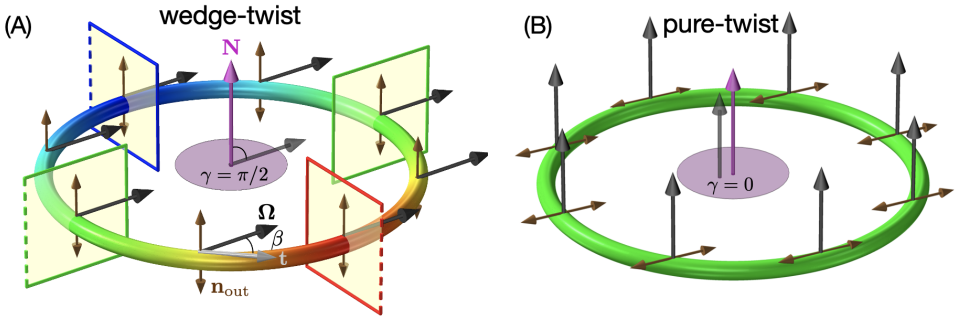


Figure 2.7: **Structure of wedge-twist and pure-twist disclination loops.** (**A**) The wedge-twist loop where local winding as reflected by angle $\gamma$ varies along the loop. $\mathbf{\Omega}$ is spatially uniform and forms an angle $\gamma = \pi/2$ with the loop's normal, **N**. Double-headed brown arrows indicate $\mathbf{n}_{out}$, the director just outside the loop. (**B**) Pure-twist loop, with $\mathbf{\Omega}$ both uniformly parallel to loop normal **N** ($\gamma$=0) and perpendicular to the tangent vector.

## 2.4 Topology of experimental loops

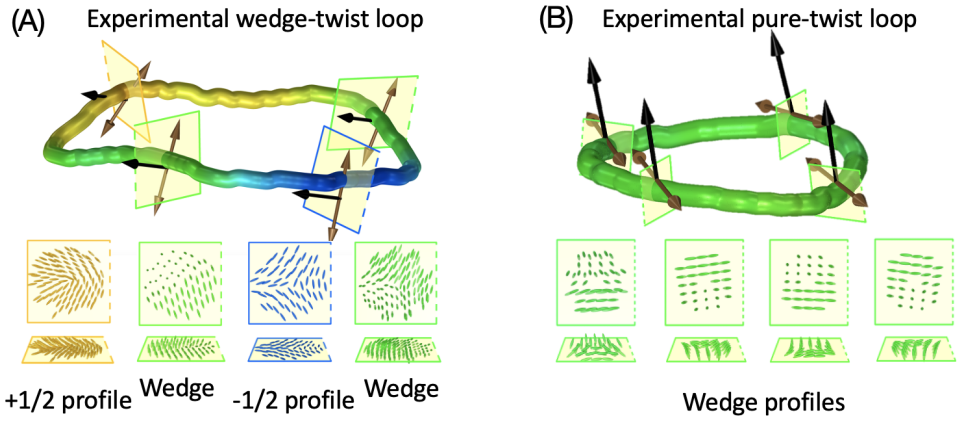


Figure 2.8: **Structure of disclination loops in experiments.** (**A**) Structure of wedge-twist disclination loops and (**B**) pure-twist disclination loops. Panels show the director field's winding in the corresponding cross-sections. Coloring of loops indicates the angle $\beta$.

Experimental measurements of the director field allowed us to fully characterize the topological structure of the disclination loops [Fig. 2.8]. Analysis of the director field indicated that the distortion lines and loops have the $\pi$ winding indicative of disclinations [Fig. 2.3], with continuous variation of $\beta$, which indicates local winding. Furthermore, most of the analyzed loops were well approximated by the family of curves where $\mathbf{\Omega}$ and $\mathbf{n_{out}}$ varied little along the loop circumferences. Categorizing loops according to their $\gamma$ values revealed that the entire continuous family from wedge-twist [Fig. 2.8A] to pure-twist [Fig. 2.8B] was represented, with the latter being more prevalent [Fig. 2.9]. Structural analysis revealed topological neutrality, as all 268 experimental loops and all 94 loops extracted from hybrid lattice Boltzmann simulations carried no charge. This demonstrates that among many possible configurations, topologically neutral loops are the dominant excitation mode of 3D active nematics. The same class of loop geometries also dominated the dynamics in our numerical simulations of bulk 3D active nematics and in confined active nematics [65, 66]. The phenomenology observed is a direct consequence

of activity-induced flows and is insensitive to backflows induced by reactive stresses. This conclusion is supported by the agreement of results from the mechanical model considered in the hybrid lattice Boltzmann method and the purely kinematic Stokes method.

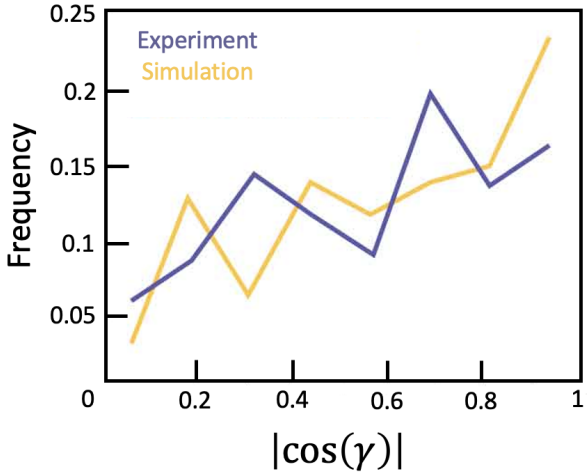


Figure 2.9: Distribution of loop types extracted from experiment (N=268) and hybrid lattice Boltzmann simulations (N=94). $|\cos(\gamma)| = 0$ for wedge-twist loops and 1 for pure-twist loops.

## 2.5 Loop nucleation dynamics

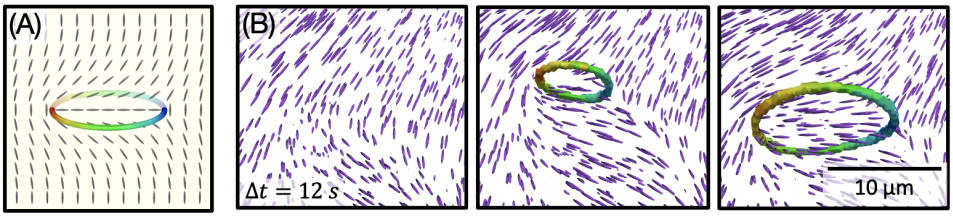


Figure 2.10: **Nucleation mechanism for wedge twist loops** (**A**) Schematic of a wedge-twist loop and the director field in the plane that intersects ±1/2 wedge profiles. (**B**) Nucleation and growth of a wedge-twist disclination loop through a self-amplifying bend distortion. Purple rods represent the 2D director field through the local ±1/2 wedge profiles.

In 2D active nematics, self-amplifying bend distortions give rise to the nucleation of a pair of topological defects of opposite charge [51, 52, 37, 53, 54, 29, 55]. Nucleation

of isolated, topologically neutral wedge-twist loops are the 3D analog of the 2D defect-creation process. Specifically, a cross-section through the +1/2 and –1/2 wedge profiles recalls unbinding of a pair of point disclinations in 2D [Fig. 2.10 A,B]. The +1/2 wedge profile typically appears on the side of the growing bend distortion, oriented away from the –1/2 wedge profile. Similarly, wedgetwist loops with the +1/2 wedge profile oriented inward toward the –1/2 wedge are driven to shrink by active and passive stresses. Unlike in 2D active nematics, after nucleation, the wedge profiles remain bound to each other through a disclination loop that includes points with a local twist winding. It is possible that some analyzed pure-twist loops have evolved from wedge-twist loops by continuous deformation of local winding character. However, both simulations and experiments showed cases of loop nucleation in nearly pure-twist ($\gamma \approx 0$) geometries from previously defect-free regions. Local active nematic stresses alone are not expected to drive growth of a pure-twist loop [Fig. 2.11A,B]. One possibility is that long-range hydrodynamic flows build up twist distortions that locally relax through creation of a pure-twist loop [Fig. 2.11C].

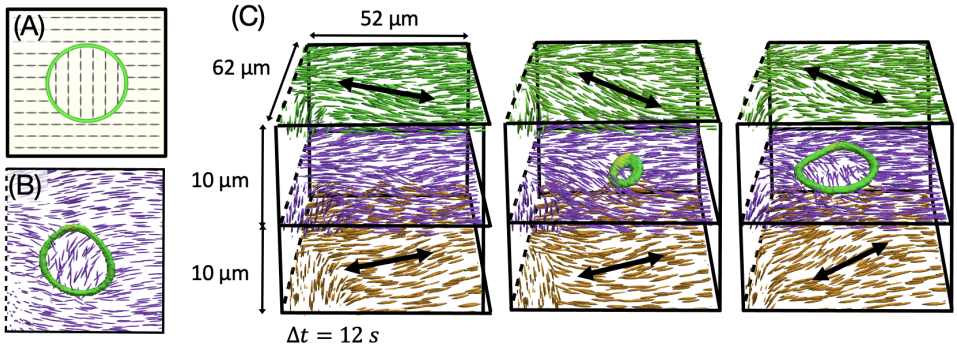


Figure 2.11: **Nucleation mechanism of pure-twist loops.** (**A**) Schematic of a pure-twist loop and the director field in the loop's plane. (**B**) Experimental view of pure-twist loop and director field in the loop's plane. (**C**) A pure-twist disclination loop nucleates and grows from a local twist distortion. Black arrows indicate the local buildup of the twist distortion.

## 2.6 Summary

By coupling a flow field to an orientational order parameter with curvilinear topological defects, 3D active nematics display dynamics even more complex than the chaotic flows of 2D active systems. Combined with emerging theoretical work [65, 66], the experimental model system described herein offers a platform with which to investigate the role of topology, dimensionality, and material order in the chaotic internally driven flows of active soft matter. Furthermore, the use of a multiview light sheet imaging technique demonstrates its potential to unravel dynamical processes in diverse nonequilibrium soft materials, such as relaxation of nematic liquid crystals upon a quench or their deformation under external shear flow [42, 67].

# Chapter 3

# ALLPS

Controlling interfaces of phase separating fluid mixtures is key to creating diverse functional soft materials. Traditionally, this is accomplished with surface-modifying chemical agents. Using experiment and theory, we study how mechanical activity shapes soft interfaces that separate an active and a passive fluid. Chaotic flows in the active fluid give rise to giant interfacial fluctuations and non-inertial propagating active waves. At high activities, stresses disrupt interface continuity and drive droplet generation, producing an emulsion-like active state comprised of finite-sized droplets. When in contact with a solid boundary, active interfaces exhibit non-equilibrium wetting transitions, wherein the fluid climbs the wall against gravity. These results demonstrate the promise of mechanically driven interfaces for creating a new class of soft active matter.

## 3.1 Introduction to system

Liquid-liquid phase separation (LLPS) is a ubiquitous phase transition, with examples abounding throughout material science, biology and everyday life [68, 69]. Immiscible liquid phases are separated by sharp, but deformable, interfaces that strongly couple to

flows and the input of mechanical energy. For example, gentle shaking of an oil-water mixture induces gravity-capillary interfacial waves, while more vigorous perturbations break up the entire interface, reinitializing the phase separation [70, 71, 72, 73]. Active matter provides an alternative method of continuously stirring a fluid [49, 74]. In such systems, mechanical energy, inputted locally through the motion of microscopic constituents, cascades upward to generate large-scale turbulent-like dynamics [29, 75, 58]. We study how active stresses and associated flows perturb soft interfaces and LLPS. Using experiment and theory, we identify universal features of active-LLPS, including giant interfacial fluctuations, traveling interfacial waves, activity-arrested phase separation and activity-induced wetting transitions. These results demonstrate how active matter drives liquid interfaces to configurations that are not accessible in equilibrium. In turn, active interfaces are elastic probes that provide insight into the forces driving active fluids, for example by allowing for the measurement of the active stresses.

The active liquid interfaces studied here belong to a wider class of activity-driven boundaries, that includes lipid bilayers, colloidal chiral fluids and interfaces between motile and immotile bacteria in a swarm [76, 25, 77, 78, 79]. From a biology perspective, LLPS has emerged as a ubiquitous organizational principle [69, 80]. How cytoskeletal active stresses couple to self-organization of membraneless organelles remains an open question. Studies of simplified systems can shed light on these phenomena. Relatedly, active wetting plays a potential role in the development and shaping of tissues [81].

## 3.2 Materials and methods

To explore how activity modifies soft interfaces, we combined poly(ethylene-glycol) (PEG) and polysaccharide dextran with stabilized microtubule filaments and clusters of kinesin molecular motors. Above a critical polymer concentration, the passive PEG-

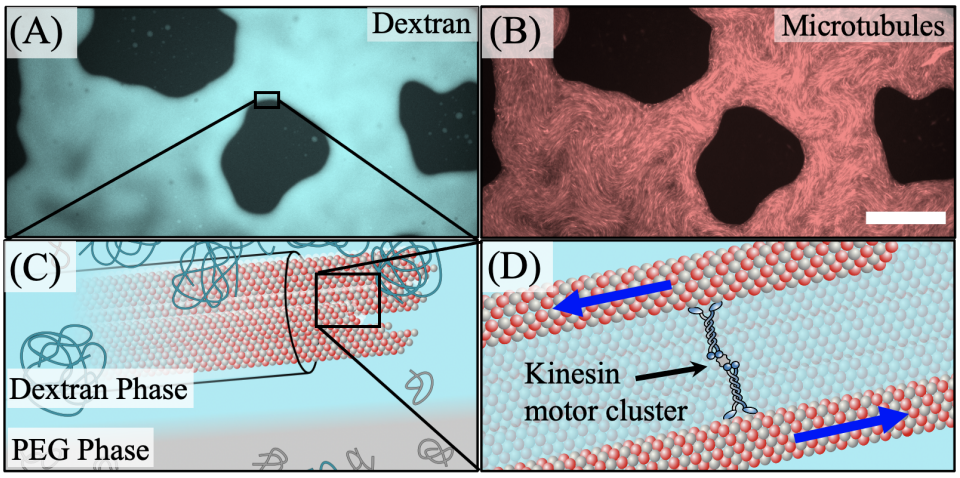


Figure 3.1: **Composition of active-LLPS** (**A**) Coexisting PEG-rich (dark) and dextran-rich (cyan) domains. (**B**) Labeled microtubules (red) are dispersed in the dextran phase. Scale bar, 75mm. (**C**) Microscopic-scale depiction of phase separation. Minority PEG polymers (gray) in the dextran-rich phase induce microtubule bundling. (**D**) Kinesin clusters drive interfilament sliding.

dextran mixture phase separated [82]. Microtubules and kinesin clusters exclusively partitioned into the dextran phase, where depletion forces promoted microtubule bundling [Fig. 3.1A-C]. Streptavidin-bound kinesin clusters (KSA) stepped along adjacent microtubules within a bundle, driving interfilament sliding. The kinesin-powered bundle extensions continuously reconfigured the filamentous network, generating large-scale turbulent-like flows, similar to those previously studied [29] [Fig. 3.1D]. The PEG-dextran interfaces were susceptible to large deformations by active stresses generated within the dextran phase, due to their ultra-low interfacial tension ($< 1$ $\mu$N/m) [82].

## 3.3 Droplet coarsening is modified by activity

We first visualized the phase separation dynamics of active-LLPS in $\sim$30 $\mu$m thick horizontal microscopy chambers. In such samples, PEG-dextran interfaces had a nearly-flat vertical profile [Fig. B.1]. The quasi-2D nature of the system was supported by a

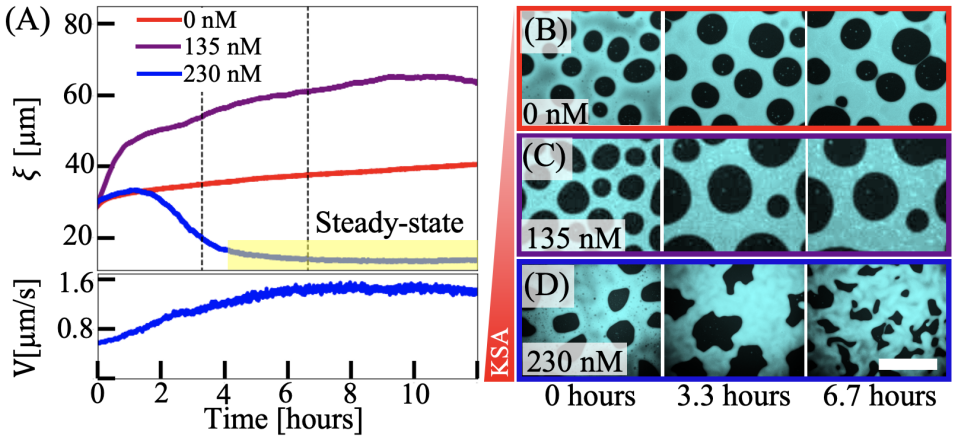


Figure 3.2: **Coarsening dynamics of active-LLPS** (**A**) Correlation length evolution, $\xi$(t) for three KSA concentrations (Top). For 230 nM KSA, $\xi$ plateaus at long time (yellow highlight).(Bottom) Root mean square velocity of turbulent flows in the dextran phase at 230 nM KSA. (**B-D**) Time series of the active LLPS at three KSA concentrations. Scale bar, 350mm.

nearly constant area fraction of the PEG-rich domains [Fig. B.2]. In a passive system with microtubules but no kinesin motors, the droplets coalesced slowly [Fig. 3.2B]. The addition of motors altered the coarsening kinetics. At intermediate KSA concentrations, active flows powered droplet motility, which increased the probability of droplets encountering each other and coalescing, thus speeding up coarsening dynamics [Fig. 3.2C]. Higher KSA concentrations accelerated buildup of interfacial fluctuations leading to an entirely different dynamical state where droplets incessantly fused and fissioned with each other [Figs. 3.2D, 3.3].

To quantify the influence of activity on the PEG-dextran phase separation, we measured the equal-time two-point correlation function $C(\mathbf{\Delta r}, t) = \langle I(\mathbf{r} + \mathbf{\Delta r}, t) I(\mathbf{r}, t) \rangle_{\mathbf{r}}$, where $I = 1$ in the dextran phase and $-1$ otherwise [Fig. B.3]. Spatial correlations decayed over a length scale $\xi$, defined by $C(\xi) = 0.5$, which is comparable to the average droplet size [Fig. B.4]. For passive samples, $\xi$ increased slowly in time [Fig. 3.2A (top)]. Enhanced coarsening at intermediate KSA concentration was reflected by a much faster initial growth of $\xi$ than the passive case. At high motor concentration, $\xi$ peaked at $\sim 1$

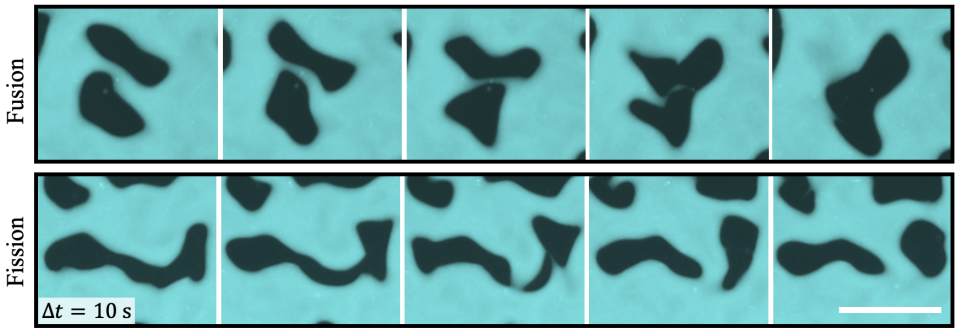


Figure 3.3: Fusion (top) and fission (bottom) of PEG droplets. Sample chamber thickness, 30mm. Scale bar, 100 $\mu$m.

hour and subsequently decayed to a finite plateau, $\xi_{steady}$. In parallel, average interface curvature $\kappa$ monotonically grew, reaching sufficient large value to cause droplet fission [Fig. B.5]. The steady-state lengthscale $\xi_{steady}$, was maintained by the balance of droplet fission and fusion events, where $\xi_{steady}$ was comparable to the inverse of the average interface curvature $\kappa_{steady}$. Concomitantly with the plateauing of $\xi$, active flow speed became constant [Fig. 3.2A (bottom)]. These results demonstrate activity-suppressed coarsening dynamics, which created an emulsion-like state wherein finite-sized droplets continuously merge, break apart and exchange their content [Fig. 3.3]. The volume fraction of the active and passive phases were nearly equal [Fig. B.2]. Low volume fraction of active fluid generated similar steady states. Finite-sized domains are reminiscent of theoretical prediction in motility-induced-phase-separation of isotropic active particles [83]. However, in contrast to theory, the active fluid in our experiments is anisotropic and perturbs an underlying equilibrium phase separation.

## 3.4 Active stresses drive interfacial fluctuations

To gain insight into how active stresses drive interfacial fluctuations we formed a macroscopic interface by gravity-induced bulk phase separation [Fig. 3.4A]. In equilib-

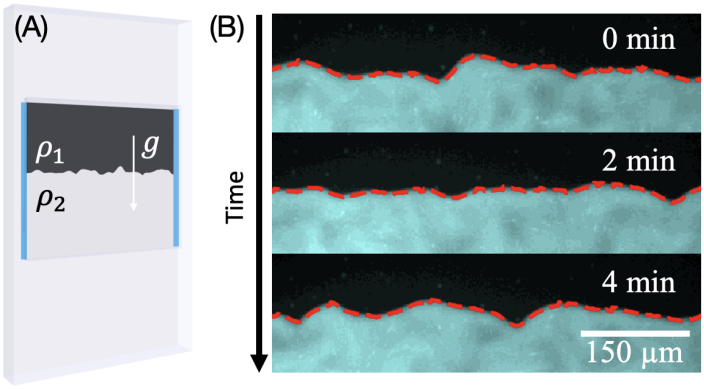


Figure 3.4: **Configuration of fluctuation experiments.** (**A**) Schematic of chamber in fluctuation experiments. The active dextran phase sediments below the passive PEG phase. (**B**) Example of a time series of fluctuations typically seen in experiment.

rium, molecular motion works against the density difference $\Delta\rho$ and interfacial tension $\gamma$ to roughen the liquid-liquid interface. Typical disturbances of PEG-dextran interfaces, bereft of activity, are $\sim$ 100 nm in amplitude, resulting in boundaries that appear flat when viewed with our imaging setup [Fig. 3.4B]. When driven out of equilibrium, however, interfaces exhibited giant undulations that were visible by naked eye. As motor concentration increased, interfaces became multivalued with frequent overhangs, indicating that active stresses directly control interface configurations [Fig. 3.5A].

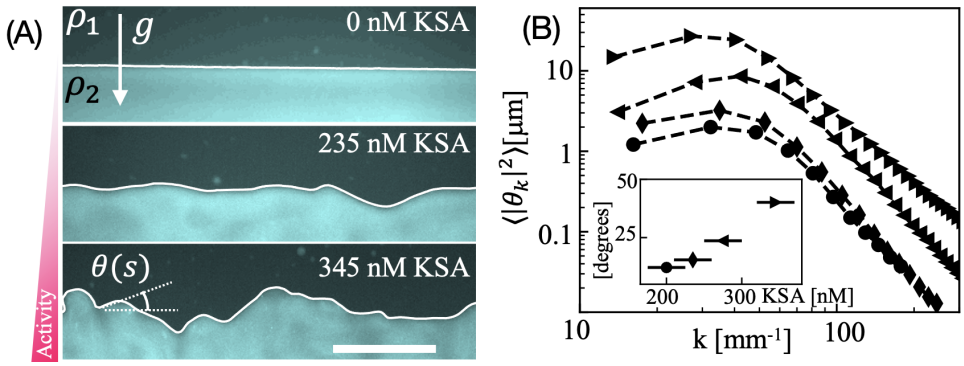


Figure 3.5: **Fluctuations of the interface with increasing KSA concentration.** (**A**) Conformations of bulk phase–separated interfaces with increasing motor (KSA) concentration. $\theta$(s) defines the local interface tangent angle as a function of arc length. Chamber thickness, 60 $\mu$m. Scale bar, 150mm. (**B**) $\theta$ power spectra obtained by averaging over 3-mm interface length, 6 to 8 hours after sample preparation. (Inset) Root mean square $\theta$ versus KSA concentration.

The interplay of activity and capillarity is clarified by measuring the interfacial fluctuation spectrum. To this end, local interface tangent angles $\theta(s,t)$ were sampled at a time $t$ as a function of the arc-length distance $s$ along the interface [Fig. 3.5A]. Interfacial fluctuations were described by time-averaged power spectra $S(k) = \langle|\theta_k|^2\rangle_t$, with $\theta_k = \int \mathrm{d}s\, \theta(s,t)e^{-iks}$. Due to equipartition of thermal energy among Fourier modes, the spectrum of equilibrium interfaces is $S(k) \sim Tk^2/(k^2 + k_c^2)$, where $T$ denotes temperature . The capillary wave-number $k_c = \sqrt{\Delta\rho g/\gamma}$, sets a crossover from a gravity dominated regime at large scales $S(k) \sim k^2$ to a plateau at small scales where surface tension attenuates fluctuations. Active interfacial fluctuations were markedly different. Active spectrum $S(k)$ increased for small wave-numbers [Figs. 3.5B]. After reaching a maximum for $k_m \sim 30\, mm^{-1}$, it decayed as $S(k) \sim k^{-3}$, instead of plateauing as in equilibrium. While the shape of $S(k)$ remained the same for all KSA concentrations, the root-mean-square tangent angle $\theta_{rms}$ increased linearly with activity [Fig. 3.5B, inset]. Using the crossover at $k_m$ as a determinant of the fluctuation amplitude, it would take an effective temperature of $\sim 10^{11}K$ to achieve equilibrium interfaces whose roughness is comparable to those measured at the lowest activities.

## 3.5 Activity produces propagating waves

The dynamics of activity-driven interfacial fluctuations exhibit non-trivial spatiotemporal correlations. To gather sufficient statistics, we imaged ∼10 mm-long active interfaces over a 2 hour interval [Fig. 3.6A]. Space-time maps of local interface height $h(x,t)$ exhibited diagonally streaked crests and troughs that were suggestive of propagating waves [Fig. 3.6B]. To characterize these modes, we measured the dynamic structure factor (DSF) of the interface height $D(k,\omega) = \int \mathrm{d}x\mathrm{d}t\, e^{ikx+i\omega t}\langle h(x',t')h(x'+x,t'+t)\rangle_{x',t'}$ [Fig. 3.6C]. Over a finite range of wave numbers, the DSF exhibited peaks at finite fre-

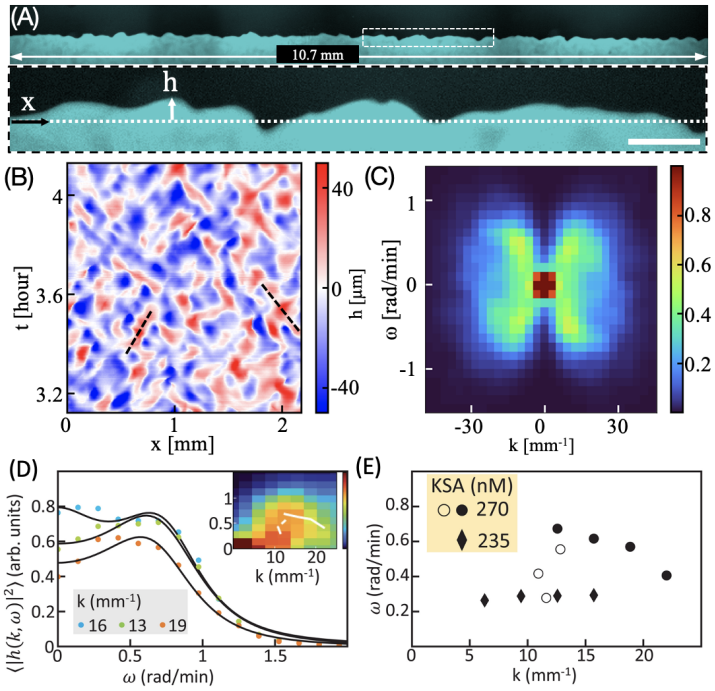


Figure 3.6: **Activity generates interfacial waves** (**A**) Example of a single interface configuration used to calculate the dynamic structure factor. (**B**) Space-time map of h(x). Disturbances propagating along the interface (dashed lines). Interfaces were corrected for drift and tilt. (**C**) The square-root DSF averaged 4 to 6 hours after sample preparation. Maximum lag distance, 1000 $\mu$m; maximum lag time 1800 sec. (**D**) DSF sections at constant wave-number (colored dots). Black lines are best approximations with $F(\omega) = a\left((\omega/\omega_1)^2+1\right)^{-1} + b\left[\left((\omega/\omega_0)^2-1\right)^2 + (\omega\Delta\omega/\omega_0^2)^2\right]^{-1}$, where $a, b, \omega_1, \omega_0, \Delta\omega$ are adjustable parameters. Data taken over 2-4 hours after sample preparation. Inset: Frequency peaks $\omega_p = \sqrt{\omega_0^2 - \Delta\omega^2/2}$ overlayed on DSF intensity (full line). DSF maxima for constant $\omega$ (dashed line). For (**A-D**), KSA concentration, 270 nM. (**E**) Peak frequencies of the propagating modes $\omega_p$ (full symbols). DSF maxima at constant frequency sections (empty symbols).

quencies $\omega_p$, confirming the presence of propagating modes [Fig. 3.6D]. Increased KSA concentration resulted in higher $\omega_p$ for the same wave-numbers; thus, activity controlled the phase velocity [Fig. 3.6E].

The giant non-equilibrium fluctuations and propagating wave modes result from the interaction of active flows in the bulk dextran phase with interfacial elasticity. To elucidate the processes driving active interfaces, we numerically integrated 2D hydrodynamic equations that describe a bulk-phase-separated active fluid [84, 85]. The two coexisting

phases were modelled as incompressible Newtonian fluids under gravity that experience confinement friction in the low Reynolds number limit. The top phase was passive, while the velocity of the bottom phase $\mathbf{v}$ was governed by

$$\gamma_v \mathbf{v} - \eta \nabla^2 \mathbf{v} = -\boldsymbol{\nabla} P + \boldsymbol{\nabla} \cdot \boldsymbol{\sigma} \,, \tag{3.1}$$

with $P$ the pressure, $\eta$ the viscosity, and $\gamma_v$ the confinement friction. The stresses $\boldsymbol{\sigma}$ driving the flows were assumed to be generated by an active liquid crystal producing extensile active stresses, $\boldsymbol{\sigma}^a = \alpha \mathbf{Q}$, with $\alpha < 0$.. The local orientational order was quantified by a traceless tensor $Q_{ij} = \langle \hat{n}_i \hat{n}_j - \delta_{ij}/2 \rangle$ averaged over molecular orientations $\hat{\mathbf{n}}$. Active shear flows engendered orientational order via flow-induced alignment. These assumptions are summarized in the continuum equation

$$\frac{D\mathbf{Q}}{Dt} + [\boldsymbol{\omega}, \mathbf{Q}] = \lambda \mathbf{u} + \frac{1}{\gamma_Q} \mathbf{H} \,, \tag{3.2}$$

with $\boldsymbol{\omega}$ the vorticity tensor, $\mathbf{u}$ the strain rate and $\lambda$ the flow alignment parameter. $\mathbf{H}$ denotes elastic forces that arise from the liquid crystal free energy, and $\gamma_Q$ the rotational viscosity of microtubule bundles. In the absence of activity the liquid crystal is in the isotropic phase, consistent with the microtubule density used in experiments.

The hydrodynamic model reproduces key experimental observations. Finite-sized chaotic flows, driven by active stresses, continuously deform the liquid-liquid interface [Fig. 3.7A]. Similarly to experiments, the interfacial power spectra showed a crossover between growth at small wave-numbers and decay at large wave-numbers, while the root-mean-square tangent angle increased linearly with $|\alpha|$ [Fig. 3.7B]. The numerically obtained DSF also exhibited signatures of active travelling waves [Fig. 3.7C-E], as in the

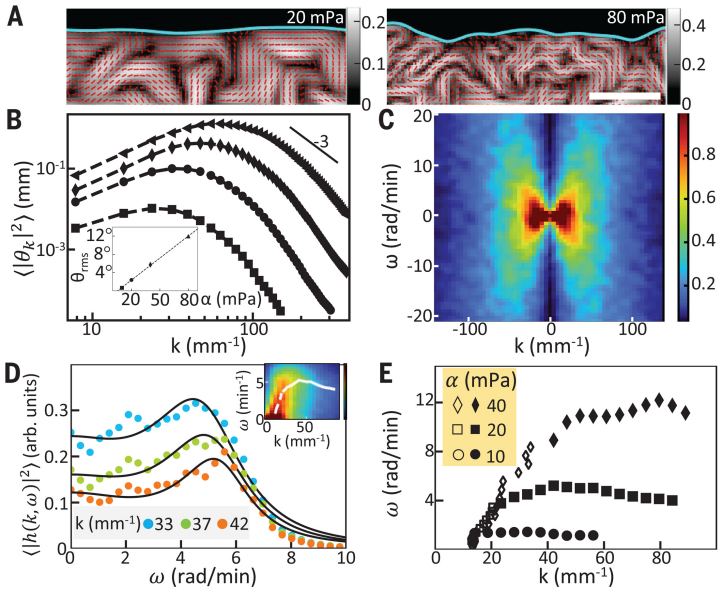


Figure 3.7: **Numerical hydrodynamics of active interfaces.** (**A**) Phase boundary (cyan) separating a passive fluid (black) and the active phase, depicted with local order parameter (grayscale) and orientation (red lines). Scale bar, 100 $\mu$m. (**B**) $\theta$ power spectra. Simulation interval, 2 mm. Correlation maximum lag distance, 400 $\mu$m. Inset: Root-mean-square $\theta$ vs. $|\alpha|$. (**C**) Square root DSF. $|\alpha| = 40$ mPa. Maximum lag time, 270 sec. Maximum lag distance, 670 $\mu m$. Total simulation time, 3 hours. Simulation interval, 2 mm. (**D**) Constant wave-number sections of DSF intensity(filled circles). Best approximations $F(\omega)$, as in Fig. 2E (black lines). $|\alpha| = 20$ mPa. Inset: $\omega_p(k)$ overlay on DSF intensity (full line). DSF maxima for constant $\omega$ (dashed line). (**E**) Peak frequencies of the propagating modes $\omega_p$ (full symbols). DSF maxima for constant $\omega$ (empty symbols).

experiment. The wave frequencies $\omega_p(k)$ increased with activity, showing active-stress-dependent wave velocity. Our numerical model also suggests a non-inertial mechanism of active waves [76], which differs from conventional inertia-dominated capillary waves [86, 87]. In the context of our hydrodynamic model, the active waves arise from the coupling between the interface vertical displacement $h$ and orientational order $Q$ in the interfacial region [85]. Stress balance at the interface predicts that the orientational order drives interfacial deformation as $\partial_t h \sim v_\perp^a \sim \alpha Q$, where $v_\perp^a$ is the active contribution to the flow velocity normal to the interface. In turn, passive flows $v_\perp^p$ relaxing the interface at a wave-number dependent rate $\nu(k)$ feed back to induce local liquid crystalline order

$\partial_t Q \sim \lambda i k v_\perp^p \sim -\nu(k)h$. Consequently, interface height obeys a wave equation $\partial_t^2 h \sim -\alpha\nu(k)h$. Accordingly, travelling wave velocities increase with active stress, which is in agreement with both experiments and numerics.

Propagating waves might be a generic feature of active boundaries [76, 25]. More broadly, the active-stress-dependent wave dispersion mirror those of elastic waves in entangled polymers solutions [88]. While the numerical hydrodynamics reproduced qualitative features of the experimentally observed active fluctuations and waves, there were important quantitative differences. In particular, with increasing activity, numerics predict increase in both interface fluctuations and bulk velocity. In contrast, in experiments active flows remain constant between 200 and 350 nM KSA, while interfacial fluctuations increase [Fig. B.9]. Moreover, in numerics, the maximum wave-number $k_m$ increased with activity, while remaining constant in experiments [Figs. 3.5B, 3.7B, B.10].

## 3.6 Activity induced wetting at a hard wall

To demonstrate the unique properties of active interfaces, we studied their structure next to a solid boundary [Fig. 3.8 A,B]. In the absence of motors, the interface assumed an exponential profile $h \propto e^{-x/\ell_e}$ with a decay length of $\ell_e \sim 45$ $\mu$m, which we identified with the capillary length $\ell_c = \sqrt{\gamma/\Delta\rho g}$. At the wall, the rise in the interface height was $\sim 70$ $\mu$m, which is close to the maximum capillary rise of $\sqrt{2}\ell_c$, indicating complete wetting [B.7.1]. At intermediate KSA concentrations, the capillary rise exhibited active fluctuations around the equilibrium exponential height profile, and the time-averaged center-of-mass height of the wetting region increased slowly [Fig. 3.8C]. Above a critical value of 300 nM KSA, activity generated a new interfacial structure. Specifically, we observed formation of a $\sim$20 $\mu$m thick dynamical wetting layer, which climbed several hundred microns above the equilibrium capillary rise [Fig. 3.8A]. Within this layer,

microtubule bundles preferentially aligned with the wall [Fig. 3.8B]. Coinciding with the appearance of the microtubule-rich wetting layer, the capillary rise sharply increased [Fig. 3.8C]. These observations demonstrate an activity driven wetting transition beyond the complete wetting of a passive fluid.

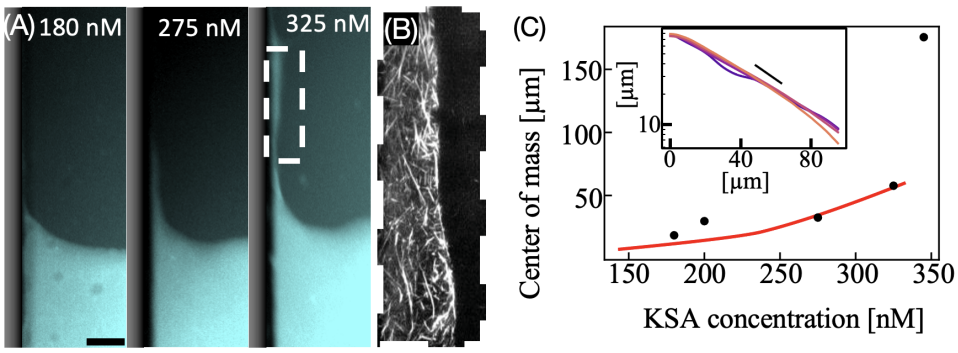


Figure 3.8: **Active wetting transition.** (**A**) Active fluid wetting on a polyacrylamide-coated vertical boundary at three KSA concentrations. Scale bar, 50 $\mu$m. (**B**) Confocal image of wetting layer aligned with acrylimide-coated wall. (**C**) Average center-of-mass height of active fluid within $5\ell_e$ of the vertical boundary, where $\ell_e = 45\mu m$. Zero height is defined as the average bulk interface position. Each point is the mean of two experiments. Uncertainty in sample preparation is indicated with horizontal bars.(Inset) Average wetting height profiles as a function of distance from the vertical boundary. KSA concentrations, 180 nM (blue) to 270 nM (red). Black line indicates $\sim e^{-x/\ell_e}$.

We performed numerical simulations of the active-interface adjacent to a vertical boundary. The liquid crystal director was anchored parallel to the wall, and the surface-liquid energy $\gamma_w$ corresponds to an equilibrium contact angle 10° [Fig. 3.9A]. Similar to experiments, the average height profile had an exponential decay [Fig. 3.9B, inset]. As the activity $\alpha$ increased from zero, the height of the contact point increased. Furthermore, above $|\alpha| = 10$ mPa, the active fluid generated a thin wall-adjacent layer, indicating a transition from partial to complete wetting [Fig. 3.9A]. The capillary rise was supported by a $\ell_w \sim 3\,\mu$m thick, vertically aligned liquid crystalline domain with $Q \sim 1$. This domain generated coherent active stress along the wall $\sigma^a = \alpha$, which supported the interface rise. Balancing the active tension $\gamma_a \equiv |\sigma^a|\ell_w$ at the contact point with wall

adhesion $\gamma_w$, surface tension $\gamma \cos\theta_a$, and gravity $F_g$ resulted in a boundary condition for the climbing interface [Fig. B.7.3, B.7.2],

$$|\sigma^a|\ell_w + \gamma_w = \gamma\cos\theta_a + F_g\,. \tag{3.3}$$

Predictions of the center-of-mass height of the capillary rise, using Eq. 3.3, show a crossover from slow to fast growth at $\alpha = 10$ mPa which is in agreement with the partial to complete wetting transition seen in simulations [Figs. 3.9B, B.12].

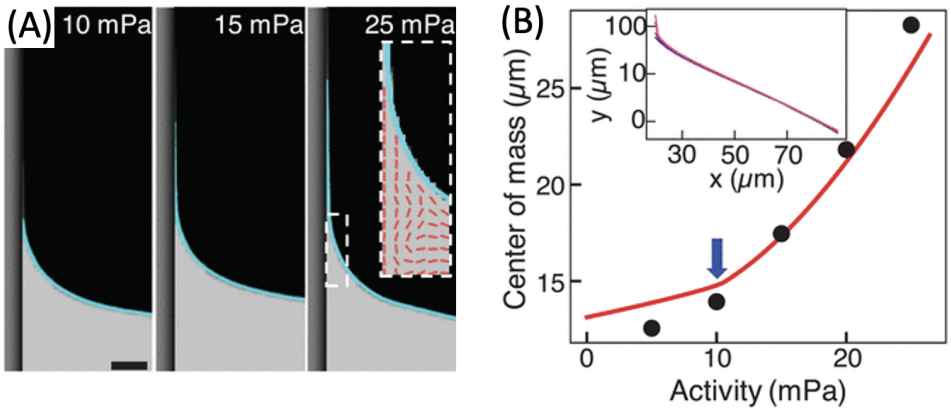


Figure 3.9: **Active wetting transition in simulation.** (**A**) Wetting profiles from numerical simulations. Equilibrium contact angle, $\theta_e = 10°$. Interface position (cyan). Scale bar, 50 $\mu$m. Inset: Local liquid crystalline orientation (red lines). (**B**) Center-of-mass height of the numerical wetting profile. Red line, prediction of Eq. 3.3 with $l_w = 2.5\,\mu$m. Onset of complete wetting (blue arrow). Inset: Average numerical wetting profiles. Activities, 10 (blue) to 40 (red) mPa.

## 3.7 Measuring active stress

Active interfaces provide a unique experimental probe to estimate the magnitude of the active stress, a critical parameter that governs dynamics of active fluids. To avoid resorting to various assumptions on the numerical model, we analytically solved Eq. 3.1 treating the stress $\sigma$ as a random field with correlations $\langle\sigma_{ij}(\mathbf{r},t)\sigma_{ij}(\mathbf{0},0)\rangle =$

$\sigma^2_{rms} e^{-|\mathbf{r}|/\ell_a - |t|/\tau_a}$, where correlation length $\ell_a$ and time $\tau_a$ are identified with those of the bulk active flow [Fig. B.13]. The analytical model captured the interface fluctuations spectrum $S(k)$ without fitting parameters, revealing that its non-monotonic shape resulted from active flows with scale-dependent kinetic energy spectrum [Figs. 3.10A, B.10, Eq. B.32] [89]. In contrast, fluctuations of equilibrium interfaces are driven by thermal energy $\sim k_B T$ that is equally distributed among all scales. By integrating $S(k)$ over all wave numbers, the active stress is predicted to increase proportionally to tangent angle fluctuations $\sigma_{rms} = p\theta_{rms}$, with $p \simeq 9$ mPa/rad [Fig. 3.10B, Eq. B.35].

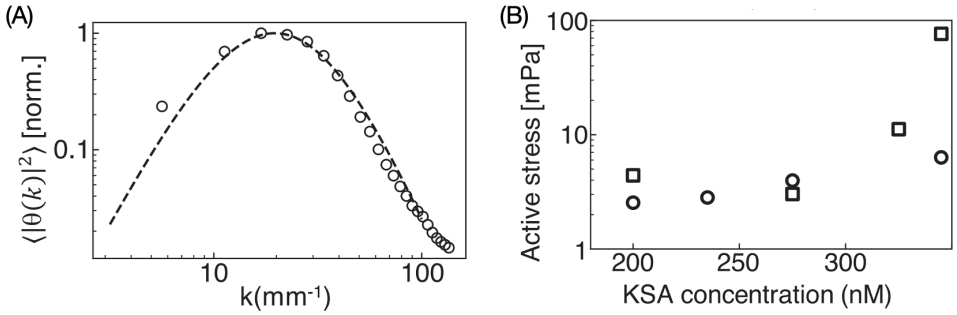


Figure 3.10: **Measurement of the active stress** (**A**) The normalized tangent power spectrum for a 200 nM KSA sample (circles), plotted with the hydrodynamic prediction from equation B.35 (dashed line). (**B**) $\sigma_{rms}$ estimate from the interfacial fluctuations (circles) plotted with the active stress estimate from active wetting.

To independently verify these numbers we note that the force balance Eq. 3.3, associated with active wetting, provides an alternative method of estimating active stress. For intermediate KSA values, prior to the appearance of the active wetting layer, the active stress estimated from wetting is comparable to those extracted from interface fluctuations [Fig. 3.10B]. Above 300 nM KSA, active stresses are a few times larger than those obtained from interface fluctuations. These large values might be a consequence of flow-enhanced alignment of microtubule bundles within the thin wetting layer. The formation of the active wetting layer at finite activity, however, is outside the scope of the static stress balance embodied in Eq. 3.3. A more complete description of the wetting

transition would include dynamical considerations, such as active wave propagation and gravitational sedimentation, that appear to be essential for the formation and turnover of the wetting layer.

## 3.8 Summary

In summary, we demonstrated a rich interplay between active fluids and soft deformable interfaces. On the one hand, liquid interfaces provide a quantitative probe that can reveal intrinsic properties of the active fluids, such as active stress. On the other hand, bulk active fluids drive the extreme interfacial deformations that yield intriguing non-equilibrium dynamics, including arrested phase separation, stress-dependent non-inertial propagating waves and activity-controlled wetting transitions. Our findings provide a promising experimental platform to design shape-changing adaptable soft materials and machines whose capabilities begin to match those observed in biology [90, 91, 92].

# Chapter 4

# Vesicle formation

## 4.1 Introduction

A remarkable feature of lipid membranes is the ability to undergo dramatic topological transformation with little energetic cost. A foundational example of such topological change is vesicle formation, where a locally flat membrane curves, budding off a spherical vesicle. Vesicles formed by budding processes are essential to cellular mechanics, facilitating transport within the cell and compartmentalizing the cytoplasm. Although of fundamental importance, studying vesicle formation in lipid bilayers is difficult due to the short length and time scales associated with vesicle closure, precluding direct visualization of the mechanics of budding with the resolution necessary to test physical mechanisms. Understanding these dynamics is critical, both to gain an understanding of membrane physics and for its relevance to biological and engineered systems.

An alternate candidate for studying the physics of membrane closure is colloidal membranes. Colloidal membranes are composed of filamentous phages, which are semi-flexible rod-like viruses that are several nanometers in diameter and hundreds of nanometers long [12]. In the presence of salt to screen electrostatic charges, and a depleting poly-

mer, phages align and self-assemble into structures. Within a range of salt and depletant concentration, filamentous phages form monolayer membranes having a thickness approximately equal to the length of the virus, and with an average particle spacing of several nanometers [Fig. 4.1A,B] [14]. These 2D fluid sheets have an identical energy functional as lipid membranes [14, 16, 15, 93], but are hundreds of microns in diameter and deform on length and time scales several orders of magnitude larger than lipid membranes. With few exceptions [17, 18], colloidal membranes appear in a flat disk-like configuration that minimizes the energy. In this chapter we detail the modification of the phage to form membranes that favor closed vesicle formation, and use these membranes to understand mechanistic pathways of vesicle closure and disassembly. The long time and length scales associated with colloidal vesicle formation, enables direct study of the energy landscape an how it relates to the observed shape change of the vesicle.

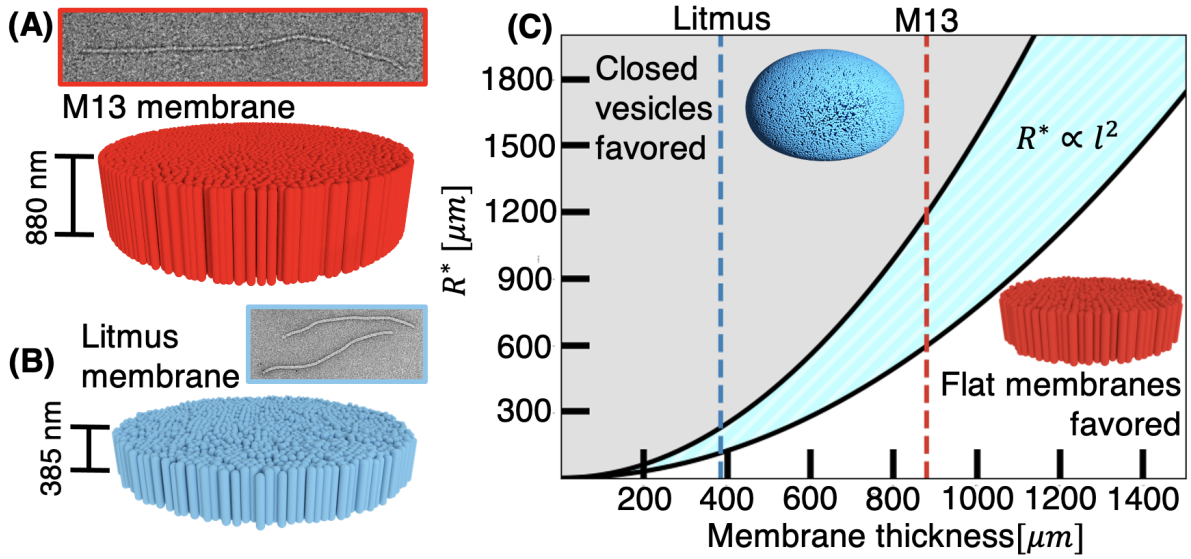


Figure 4.1: **Stability of flat disks vs edgeless vesicles.** Both (**A**) Wild-type M13 and (**B**) Litmus align and assemble into membranes whose thickness is set by the rod length. (**C**) Phase diagram of membrane thickness and area showing where flat membranes (white) or closed vesicles (gray) are favored in experiment. The shaded region is a metastable region. The vertical lines corresponds to M13 membranes (red) and Litmus membranes (cyan).

## 4.2 Background

The size and composition of colloidal membranes make them ideal for studying the physical principals of models that underpin our understanding of membranes. By leveraging genetic engineering techniques, previous work has altered the physical properties of phage particles, modifying the length [94], chirality and rigidity [12]. Membranes made from mixtures of phage types has enabled study of processes like membrane raft formation, where domains of small rods separate from the membrane to form circular domains [18], a process known to be important in cellular membranes [95]. Similarly, changes in phage structure can alter the energy landscape of the assembled membranes, producing structures like ribbons, catenoids and sponge phases [96, 17]. Aside from these few exceptions, colloidal membranes assemble as flat sheets that minimize curvature energy. However, lipid membranes most often appear as closed vesicles. Assembling colloidal vesicles would provides an unique opportunity to study the topological transformations that underpin closure of lipid membranes.

The Helfrich Hamiltonian provides theoretical insight into the vesicle to disk transition, considering only the curvature and edge tension terms [97, 98]:

$$E = \gamma \int dL + \frac{\kappa_c}{2} \int (2H)^2 dA \tag{4.1}$$

where $\kappa_c$ the mean curvature modulus and $\gamma$, the edge tension. In this approximation, we have ignored the Gaussian curvature, as the Gaussian bending modulus is generally much smaller than the mean bending modulus in colloidal membranes [16]. To estimate membrane stability, we consider the energy of both a flat membrane and a closed spherical vesicle. A flat membrane has no bending energy contributions

$$E_{mem} = 2\pi R\gamma \tag{4.2}$$

while closed spherical vesicle does not have an edge tension energetic contribution, but has a bending energy of

$$E_{vesicle} = 8\pi\kappa_c. \tag{4.3}$$

The flat membrane conformations is favored over the closed vesicle when $E_{vesicle} > E_{mem}$, which occurs when

$$A^* \geq 4\pi(2\frac{\kappa_c}{\gamma})^2. \tag{4.4}$$

For membranes larger than this area, the curvature energy of the vesicle configuration becomes smaller than the line tension of a flat disc, favoring the formation of a closed vesicle [Fig. 4.1C] [14]. To decrease $A^*$, we recognize that both $\gamma$ and $\kappa_c$ depend on the viral length, $l$, with $\gamma \propto l$ and $\kappa_c \propto l^3$, so that $R^* \propto l^2$ [98]. This strong dependence on viral length predicts that shortening the virus will dramatically increase the likelihood of forming closed colloidal vesicles.

Analogous work studying the disk to vesicle transition has been preformed in molecular dynamics simulations of lipid bilayers. Flat bilayers that are initialized as a spherical cap, will close into a vesicle with a probability dependent on both the area and curvature moduli [99]. More detailed analysis has correlated bilayer thickness and stiffness with spontaneous curvature and the critical area to form a vesicle [100]. However, these analyses also reveal that vesicle closure is expected in lipid bilayers with a radius of $\approx 20nm$, far below the resolution of optical microscopes.

## 4.3 Colloidal vesicles take on an energy-minimizing shape

We will begin by studying the shape of static colloidal vesicles. First, will form closed colloidal vesicles, and image their three-dimensional structure. We will then extracting the surface that contours the vesicles from the raw images. Finally, we will compare the vesicle surface with shapes predicted by minimizing the Helfrich Hamiltonian. This will serve as an initial test of whether colloidal vesicles can be described using the Helfrich Hamiltonian, and therefore whether they behave like lipid vesicles.

To form colloidal vesicles, we used the 385 nm long phagemid Litmus 38i [101] to make membranes. We found that the single substitution of a shorter phage was sufficient to produce colloidal vesicles. After making samples according to C.1.1, we found vesicles resting on the bottom of the chamber. Using spinning-disk confocal microscopy, we recorded the three-dimensional shape of the resulting vesicles [Fig. 4.2A]. Vesicles were only imaged if they were not in contact with other membrane structures and were therefore axisymmetric [Fig. 4.2B]. Such vesicles can be completely described by their cross-sectional contour [Fig. 4.2C]. We observed a wide distribution of colloidal vesicles shapes and sizes, with diameters ranging from $\approx 100\ \mu m$ to $\approx 350\ \mu m$. Small vesicles were usually found to be nearly spherical is shape [Fig. 4.2D,E], while larger vesicle would often sag in the middle [Fig. 4.2F].

To describe the shape of experimentally observed vesicles, we use an axisymmetric parameterization $r(s)$ and $z(s)$, for arclength $s$, which simplifies the energy of the vesicle

$$E = \int (\frac{\kappa_c}{2}(2H)^2 + \bar{\kappa}G + \sigma g z + \mu) r ds + P \int r^2 \cos\phi ds \tag{4.5}$$

where $\sigma$ is the arial density, $g$ is the gravitational constant, $\bar{\kappa}$ is the Gaussian modulus,

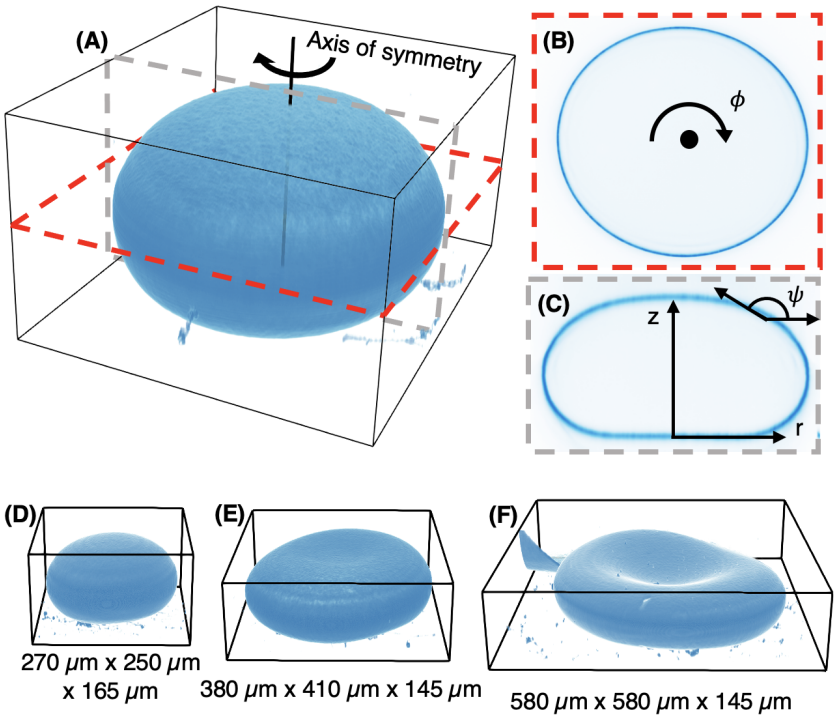


Figure 4.2: **3D images of colloidal vesicles** (**A**) A typical Litmus vesicle seen in experiment. (**B-C**) Cross sections of this vesicle with overlaid coordinate system. (**D-F**) Renderings of several vesicles showing the variation of vesicle size and shape observed in experiment.

$G$ is the Gaussian curvature, $\mu$ is a Lagrange multiplier to enforce a constant area and $P$ is a Lagrange multiplier to enforce a constant volume. Term $P$ is a pressure, accounting for the possibility that a closed vesicle may be inflated or deflated. The possibility for a vesicle to remain inflated or deflated is due to the several nanometer spacing between viral rods [16]. Pores of this size would easily allow the volume to change by exchanging water with the surrounding fluid, but the dextran, with a radius of gyration of 20 nm, cannot be exchanged through the vesicle [102]. Once the vesicle is closed, it is prevented from changing its volume, since inflating of deflating would alter the concentration of dextran inside the vesicle, producing an osmotic pressure difference across the membrane.

Taking the deviation of the energy functional in $r$, $z$ and $\psi$ leads to several Euler-Lagrange equations. These equations transform into a set of eleven first-order ordinary

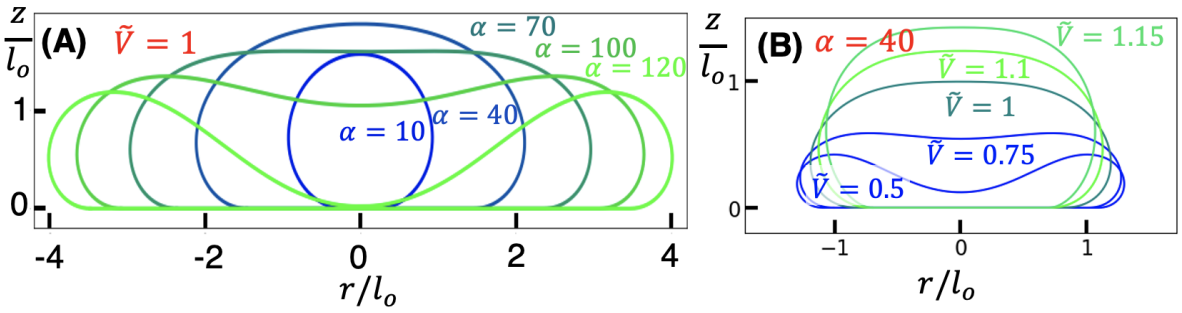


Figure 4.3: **Numerical solutions for closed vesicles.** (**A**) Predicted curves with varying $\alpha$ values with $\tilde{V} = 1$. (**B**) Predicted curves varying $\tilde{V}$ with fixed $\alpha = 40$.

differential equations that are solved numerically C.6. In this model, the shape of the vesicle is set by two adjustable dimensionless parameters $\alpha = A(\frac{\sigma g}{\kappa_c})^{2/3}$, and $\tilde{V} = \frac{V}{V_0}$, where $A$ and $V$ are the area and volume and $V_0$ is the volume at $P = 0$. Small $\alpha$ values correspond to vesicles having a small area. In this limit, the vesicle shape is dominated by the curvature energy and is roughly spherical. At large $\alpha$ values the gravitational energy significantly affects the vesicle shape, causing them to sag under their own weight [Fig. 4.3A]. Similarly, $\tilde{V}$ alters the vesicle shape from sagging deflated vesicles at small $\tilde{V}$ to contours that are inflated and rounded at large $\tilde{V}$ [Fig. 4.3B].

Our model predicts that the vesicle shape is completely defined by $\kappa_c$, the surface area and the volume of each vesicle. We will measure these quantities to predict the vesicle shape, and overlay with the experimental images. Since, the equations do not have any adjustable parameters, comparing the predicted shape with the images will serve as a rigorous test for our model. The area and volume are measured directly after converting the confocal images into a mesh, as described in C.1.4. The bending modulus $\kappa_c$ was measured by fitting the out-of-plane fluctuation spectrum of flat membranes [97], as described in C.2.3. The value of $\kappa_c$ was found to be $11000 \pm 1000 k_B T$ is four orders of magnitude larger than the typical bending modulus of a lipid bilayer [103, 104] and consistent with previous measurements of fd-wt membranes [16]. Since $\kappa_c \propto l^3$, it is

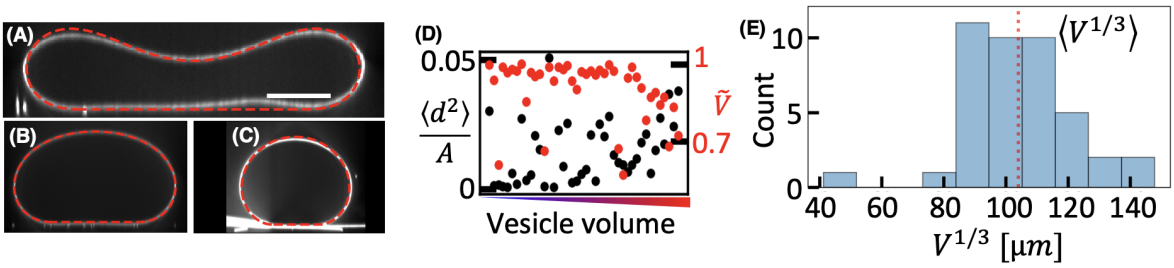


Figure 4.4: **Comparison of predicted shape with experimental vesicles** (**A-C**) Examples of cross sections of observed vesicles using measured values of $\kappa_c$, $V$ and $A$. Scale bar 80 $\mu m$ (**D**) $\frac{\langle d^2 \rangle}{A}$ value of vesicle fit and $\tilde{V}$ for N=42 vesicles. (**E**) Histogram of $V^{1/3}$ for all 42 vesicles in experiment, with red dashed line showing the average.

unsurprising that thick colloidal membranes have a large bending modulus.

After determining all necessary parameters experimentally, we compare the vesicle cross sections with the predicted vesicle shape. We imaged 42 isolated vesicles, converted each into a mesh and measuring the area and volume. We then solved the numerical equations for each vesicle, an overlaid the predicted contours over a cross section of the vesicle [Fig. 4.4A-C]. The contours predicted by the Euler-Lagrange equations fit well over the experimental data, with no free fitting parameters. This demonstrates that the shape of vesicles minimizes the energy, given a fixed volume and area. To measure the goodness-of-fit between the predicted contour and the exact shape of the vesicle cross sections we detected the bright region of the image using a standard active contouring scheme. The fit for each vesicle in experiment was characterized by the average squared distance between the predicted contour and the actual contour, $\langle d^2 \rangle$ normalized by the total area of the vesicle. The normalized squared distance between curves averaged across all vesicles was $\frac{\langle d^2 \rangle}{A} = 0.015$ with the largest value being $max(\frac{\langle d^2 \rangle}{A}) = 0.05$ [Fig. 4.4D]. Plotting $\tilde{V}$ s a function of vesicle volume, one notices that large vesicles tend to be underinflated, while smaller vesicles are not [Fig. 4.4D], measured across a wide range of vesicle [Fig. 4.4E]. This demonstrates that the volume term is essential to describe colloidal vesicle shape.

## 4.4 Dynamics of gravity-assisted vesicle formation

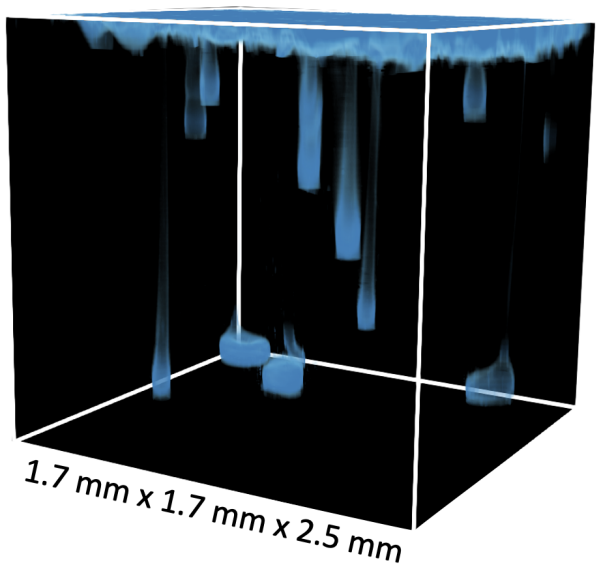


Figure 4.5: Snapshot of entire chamber, showing both pendent membranes and closed vesicles at the chamber bottom.

We observe colloidal vesicles that form after being suspended from the top of the chamber. However, the analysis in section 4.2 does not take into account gravitational energy, and so will not accurately describe the vesicle formation observed here. We find the formation of colloidal vesicles is a two step process. The first step is an hours-long elongation from a curved membrane into a tube-like membrane. The second more rapid step, is initiated by a small crack near the attachment point with the top surface. Just after inverting the chamber, curved pendent-shaped membranes were found suspended from the upper chamber surface [Figs. 4.5, 4.6A]. These membranes had attachment points with the top glass surface, preventing them from immediately sedimenting to the bottom of the chamber. The suspended membranes had different extension and shapes, which slowly evolved over time.

We seek to explain these pendent membranes, using a similar framework as before. To predict the membrane shape, we solved the the Euler-Lagrange equations associated

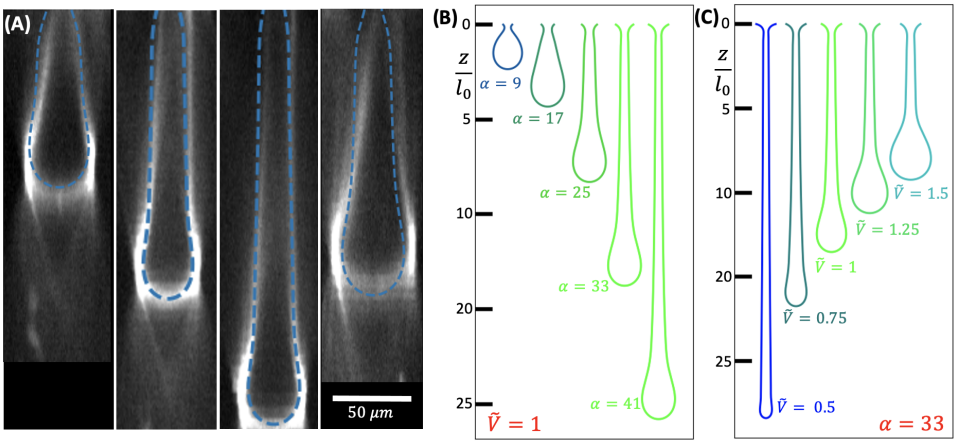


Figure 4.6: **Shape of pendent membranes.** (**A**) Cross sections of several pendent membranes at single time point with predicted fit. (**B**) Predicted vesicle shape at $\tilde{V} = 1$ with varying values of $\alpha$. (**C**) Vesicle shape at $\alpha = 33$ with variable $\tilde{V}$.

with a pendent membrane C.3.3. These equations are identical to closed vesicles, with alternate boundary conditions to account for the opening at the top. Solving these equations predict a family of shapes as a function of $\alpha$ and $\tilde{V}$. With increasing $\alpha$, associated with a larger area, pendent membranes become more elongated [Fig. 4.6B]. Altering $\tilde{V}$ changes the volume inside the pendent membrane, making the contour thin and elongated at small $\tilde{V}$, or rounded and retracted at large $\tilde{V}$ [Fig. 4.6C]. Similar to closed vesicles, the area and volume completely define the membrane shape.

To predict the shape of the pendent membranes, we extract the mesh from the raw images. The area and volume were measured from these meshes for each membrane. The predicted shapes were plotted over the images and found to match the experimentally observed shape well, with no fitting parameters [Fig. 4.6A]. This shows that, similar to the above-described vesicles, the pendent membranes also minimize the energy for a given area.

It is surprising that the shape of pendent membranes agree with an energy minimizing contour, considering pendent membranes are not static, but slowly extend under gravity. The slow dynamics of the colloidal membranes allow the 3D shape of pendent membrane

to be visualized over several hours. Pendent membranes were observed to extend to the chamber bottom, stretching hundreds of microns [Fig. 4.7A], while others stabilized at a finite length [Fig. 4.7B].

To understand the observed extension dynamics of these pendent membranes, we first modeled them as a viscous cylinder that extends under gravity. As a simple model, we can consider the pendents to be a viscous cylinder with thickness d, radius $rt$ and length $l(t)$. For an extension rate of $\dot{l}$, the viscous dissipation is $\dot{E} = \eta_m \int (\nabla V)^2 d^3x = 4\pi\eta_m r d\frac{\dot{l}}{l}$. The bending and gravitational energy of a cylindrical membrane is $E = \frac{\kappa_b}{2}\int (2H)^2 dA + \Delta\sigma g \int z dA = \Delta\sigma g A\frac{l}{2} + \frac{2\kappa_b l^2\pi^2}{A}$. Setting the time derivative of the energy equal to the viscous dissipation, gives $\dot{l} = \frac{\Delta\sigma g}{4\eta_m d}l^2 + \frac{2\kappa_b\pi^2}{A^2\eta_m d}l^3$. Inputting experimentally measured numbers into this equation, we find that a viscous cylinder will extend from l = 200 $\mu m$ to l = 800$\mu m$ in $\approx$ 20 s, which is several orders of magnitude faster than is seen in experiment [Fig. 4.7C]. This suggests the existence of an alternate mechanism that controls the extension rate.

To understand the extension of pendent membranes, the area and volume of the pendent membranes were tracked over time [Fig. 4.8B]. We calculated fits of the pendent membranes, using the measured area as an input parameter and the volume as a fitting parameter. The resulting contours overlay the raw images well, indicating that throughout the extension process, the pendent membrane minimizes energy [Fig. 4.8A]. We note that $\tilde{V} \approx 1$ throughout pendent extension, indicating that pendant membranes extend by recruiting material to increase their surface area, while extending slowly enough to maintain zero pressure and minimize their energy throughout extension [Fig. 4.8C]. The pendent membranes maintain this zero pressure state by exchanging dextran with the surrounding fluid through opening at the top. These membranes also have a relatively short time scale associated with shape relaxation when compared with the hours-long extension time, giving them time to relax their to their energetic minima throughout

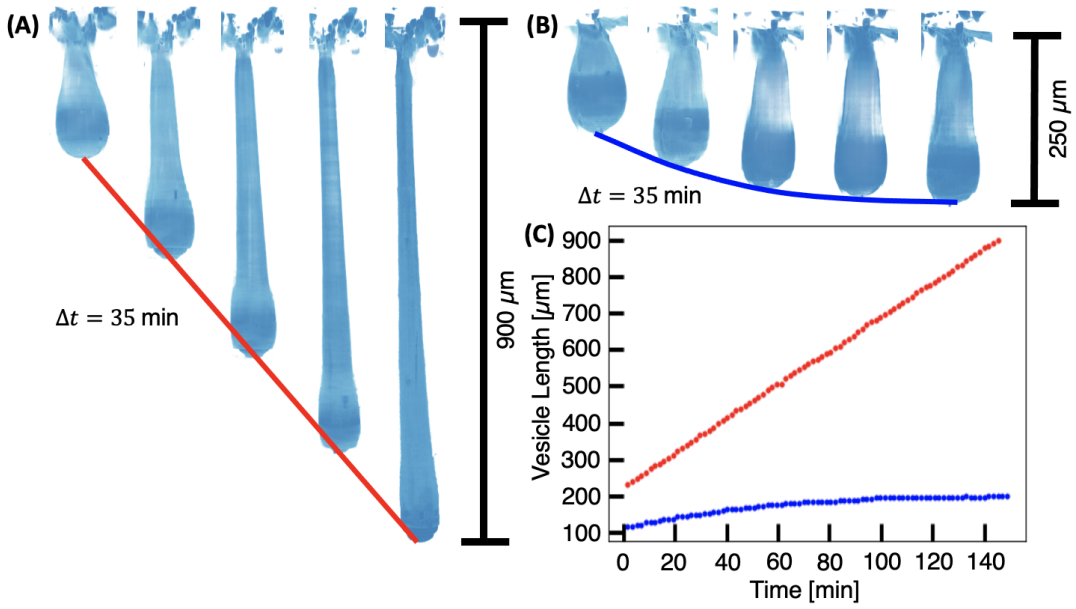


Figure 4.7: **Time series of pendent membranes.** (**A**) Pendent membrane extending toward chamber bottom. (**B**) Pendent membrane that stabilizes after a finite time. (**C**) Rates of falling for both membranes.

the extension process. In this way pendent membranes pass through a series of energy minimizing surfaces as they recruit material, extending toward the chamber bottom.

In the second regime of vesicle formation, the membrane tears away from the top surface of the chamber before forming a closed vesicle [Fig. 4.9A]. Initially, a small crack forms near the attachment point where gravitational stresses are largest, which propagates downward. This crack remains roughly parabolic when small, but as it propagates, the tear unwraps the pendent neck, leaving a flat tether connecting the extending membrane to the top of the chamber. The membranes continue extending to the bottom of the chamber for several millimeters, driven by the stretching of this tether, before reaching chamber bottom. The membrane then remains attached to the top of the chamber by this tether, holding a single pore of the membrane open. Within several hours, the tether continues to thin, eventually snapping and pulling away from the vesicle. The pore then rapidly closes, leaving an isolated vesicle at the chamber bottom [Fig. 4.9B].

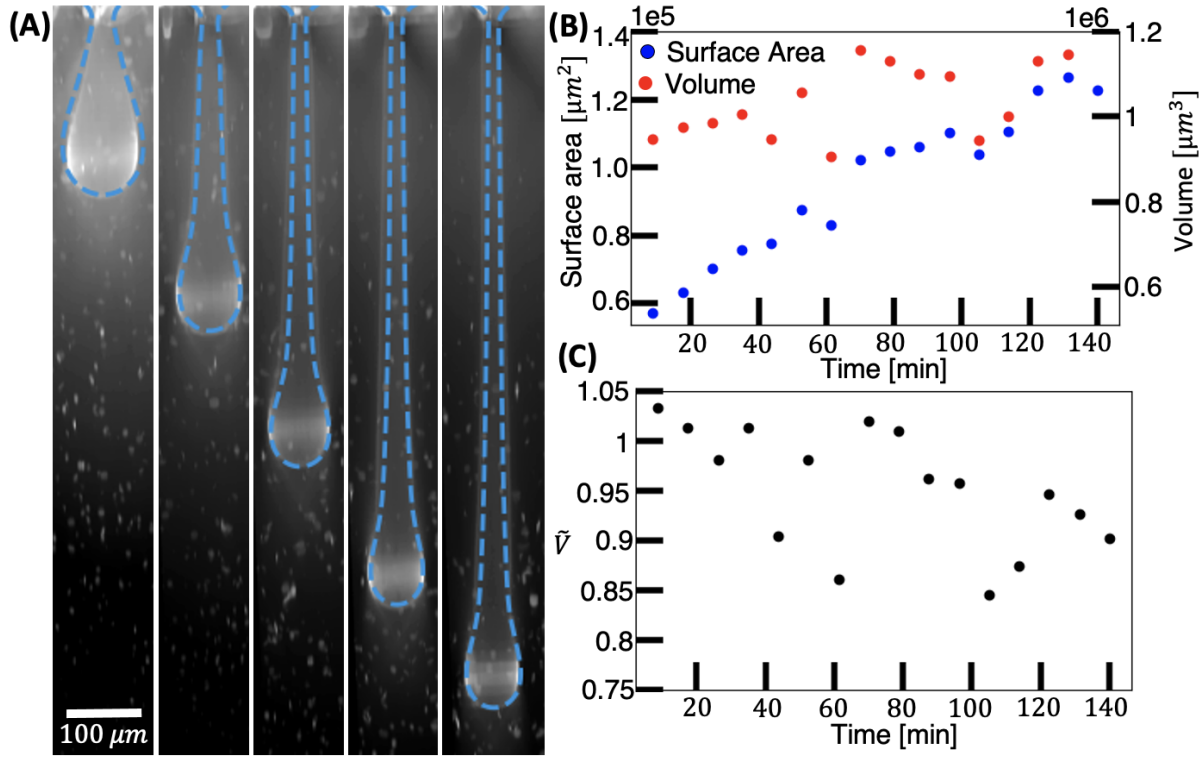


Figure 4.8: **Pendent membrane extending over several hours** (**A**) Cross sections of membranes with predicted profiles overlaid. (**B**) The surface area and volume of this membrane increases throughout extension, while (**C**) $\tilde{V}$ remains near 1.

The two relevant time scale associated with this pore closure are the time associated with vesicle closure and the time associated with the exchange of dextran to reduce the pressure across membrane. We hypothesize that the magnitude of these time scales is similar and that explains the deviation from $\tilde{V} = 1$ observed in closed vesicles. Since large vesicles take more time to exchange dextran with their surrounding, they are most likely to deviate from $\tilde{V} = 1$.

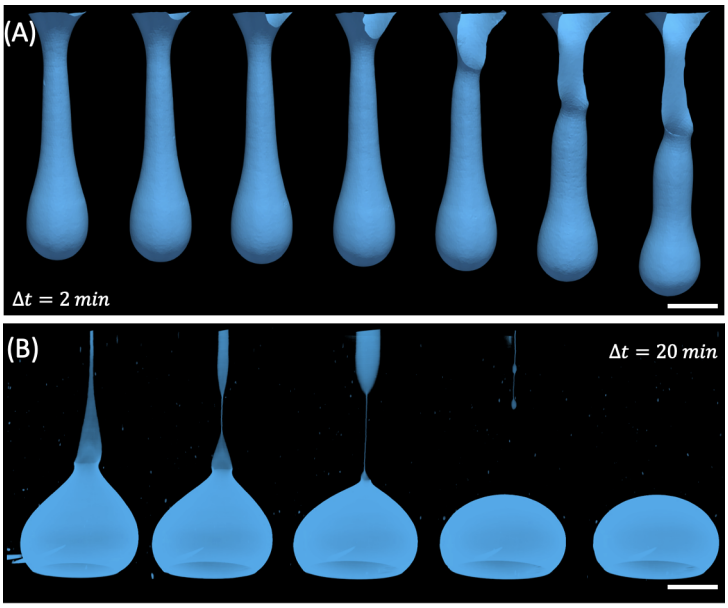


Figure 4.9: **Pendent membranes tear before extending.** (**A**) Time series of membrane after tear forms. (**B**) Tether pulling away, leaving a closed vesicle. Scale bars 100 $\mu m$

## 4.5 Kinetic pathways of vesicle disassembly follow the energy landscape

So far, we have described the equilibrium shape of colloidal vesicles and the gravity-assisted process that leads to their formation. In this section, we will induce continuous shrinking of closed vesicles. Elastic energy arguments demonstrate that, below a critical size, closed vesicles become unstable and will transform into a flat sheet 4.1. This opens the possibility to track the dynamics of vesicle disassembly.

To probe the phenomena of vesicle disassembly into a flat membrane, we formed colloidal vesicles as before. Subsequently, we used a dialysis chamber to reduce the salt concentration in the sample, thereby reducing the electrostatic screening between phages [Fig. C.5]. The increased electrostatic repulsion between the particles caused their evaporation from the 2D membrane surface into the background solvent. The

consequence of this is a continuous reduction in the vesicle area.

Throughout the reduction of vesicle area, we observe two stages of vesicle disassembly. In the first stage, transient pores nucleate on the surface of the vesicle [Fig. 4.10A]. These pores remain open for several minutes before closing again. The transient pore formation is indirectly caused by the area decrease of the vesicles. As the vesicles shrink, dextran is concentrated inside, since vesicles are impermeable to the 500 kDa dextran. Consequently, there is a buildup in the pressure difference between the inside and outside of the vesicle. This pressure difference increases the surface tension, which allows for the nucleation of the pore. The dextran is then able to escape through this open pore, equilibrating the pressure and allowing the pore to reseal.

With continued shrinking, one approaches the limit of vesicle stability. At this critical area, the pores do not close again, but remain open throughout the remainder of vesicle shrinking. This is the second stage of vesicle disassembly. With continued shrinking, one pore remains open, and the vesicle takes on a bulbous shape. This is followed by the opening of a second pore which is diametrically opposed to the first. Both holes continue to grow while the membrane decreases in area, yielding an intermediate tube-like structure. On longer time scales, the configuration breaks symmetry, with one pores growing while the other shrinks, inverting the tube into a flat membrane [Fig. 4.10B].

Membranes were also observed which did not open a second pore, but instead followed a simpler pathway toward vesicle disassembly. The single pore remained on the surface, until the membrane reached a critical area, at which point, the pore opened completely, unwrapping the membrane into a flat sheet [Fig. 4.10C]. All vesicles were observed to shrink continually, and followed one of these two pathways [Fig. 4.10D,E].

The instantaneous membrane shape can be understood as a local energy minimum. The energy of membranes with pores can again be found by solving the associated Euler-Lagrange equation for one pore (C.3.4) or two pores (C.3.5). Constructing this energy

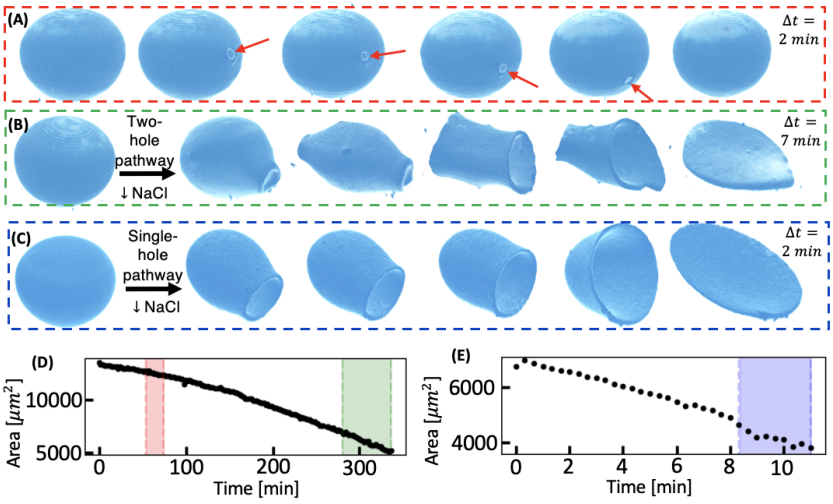


Figure 4.10: **Shrinking vesicles undergo shape change.** (**A**) Time series showing spontaneous pore opening. (**B**) Time series of vesicle unwrapping via the two pore and (**C**) single pore pathway. (**D**) Surface area of vesicles, with highlighted region showing the regime of transient pores (red) and the two pore unwrapping (green). (**E**) Surface area of the vesicle undergoing single pore unwrapping.

landscape required three input variables; the vesicle area, $\kappa_c$ and the line tension $\gamma$. Since $\kappa_c$ has already been measured, and the area can be measured from meshes as before, only $\gamma$ is left to measure. The line tension of the membranes was extracted from the in-plane fluctuations thermal fluctuation spectrum of flat colloidal membranes, described in C.2.4. This was done for nine separate membranes, to measure an average of $\gamma = 350 \pm 20 k_B T/\mu m$ [Fig. C.6C].

The dynamic of disassembly is slow, determined by the rate of vesicle evaporation. Studying intermediate points along this pathway are quantitatively described by minimizng the energy, given the boundary conditions measured from experiment. The shapes found by minimizing the energy match the membrane cross section with no free parameters [Fig. 4.11]. This demonstrates that the change in area is sufficiently slow that the vesicle is constantly in a local energy minimum for a given area. The membrane shape change is then determined by the rate of change of the area.

To explain the shape transformation as the vesicle shrinks, we construct the energy

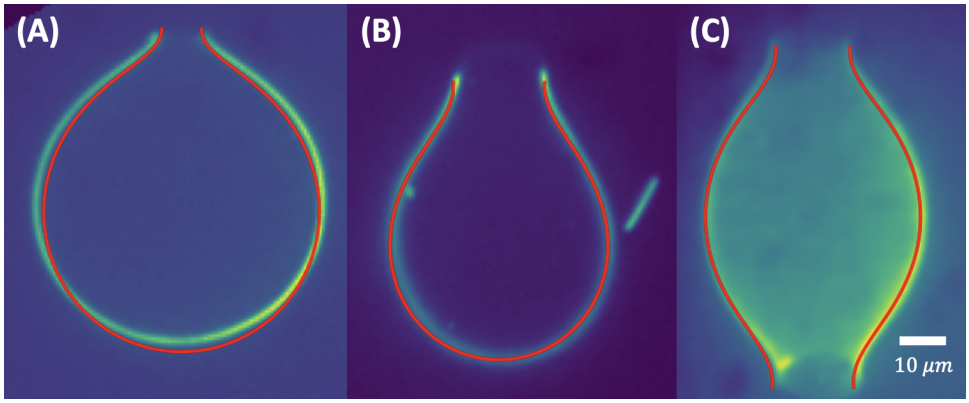


Figure 4.11: **Predicted one and two pore membrane shape plotted over experimental data.** Membrane shape (**A**) one minute and (**B**) 15 minutes after a single hole nucleates. (**C**) two-hole contour over experimental data. All predicted shapes are in good agreement with the experimentally-observed shapes.

landscape as a function of membrane size. We numerically found the energy-minimizing contour for a fixed area, $A$, and pores radii $r_1$ and $r_2$. By sweeping through all possible values of the two radii at an area, $A$, the full energy landscape $E(r_1, r_2, A)$ at several vesicle areas was constructed. Motivated by the observation that vesicles appeared in a configuration that locally minimize the energy, we studied the minima of these energy landscapes, beginning by considering only membranes with two pores. Large membranes ($\approx$ 10,000 $\mu m^2$) had a global energy minima at zero pore size [Fig. 4.12A], indicating that at this surface area, vesicles are universally stable. For intermediate sized membranes ($\approx$ 7200 $\mu m^2$) the local energy minimum moves away from zero, producing a shape with two stable finite-sized pores [Fig. 4.12B]. This local energy minimum is a symmetric configuration, with both pores being identical. At this area, the global minimum is in a flat-membrane configuration (located in phase space at $r_1 = 0, r_2 = 1$ or $r_1 = 1, r_2 = 0$), but the vesicle is prevented from unwrapping to a disk by a large energy barrier. With continued area decrease this energy barrier disappears ($\approx$ 6000 $\mu m^2$), so that the vesicle will unwrap to a flat membrane from any configuration in the energy landscape. Beginning from a membrane with two symmetric pores, the steepest energetic descent

will drive the shape of the membrane toward the saddle point, corresponding to a tube configuration. This configuration will spontaneously breaking symmetry to unwrap into a flat membrane [Figs. 4.12 C,D, 4.13]. Taking equally-spaced configurations along gradient decent pathways of the energy landscape produces expected membrane shapes that qualitatively agrees with those seen in experiment [Fig. 4.15].

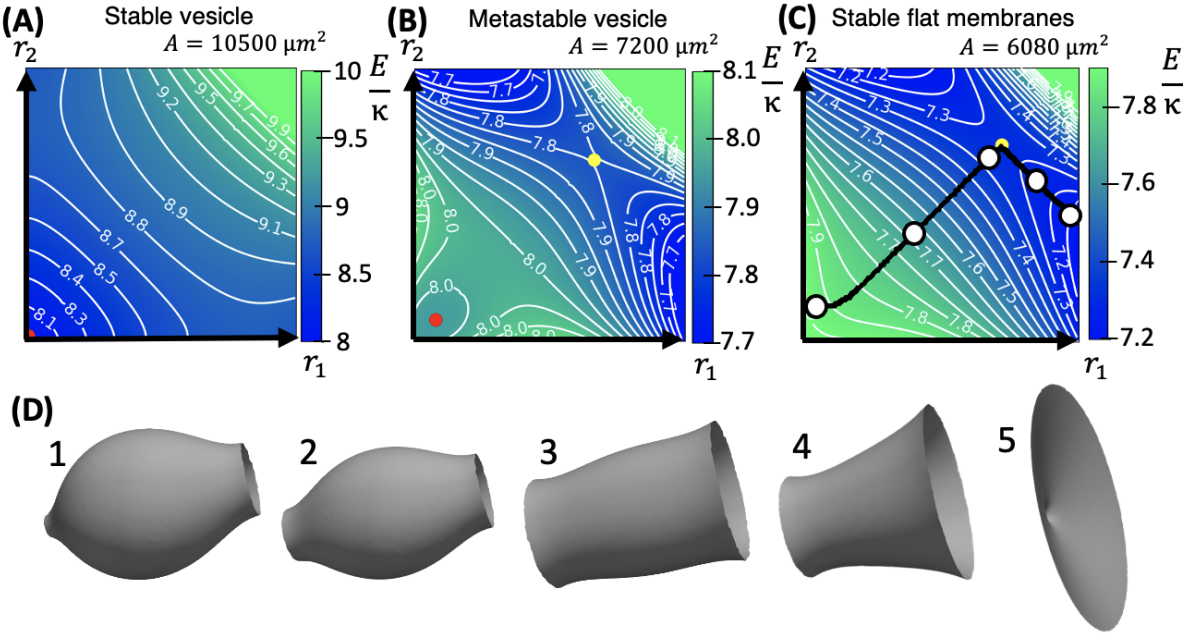


Figure 4.12: **Shrinking vesicles undergo shape change.** (**A-C**) Two pore energy landscape for decreasing surface areas. The reduced energy $\frac{E}{\kappa_c}$ as a function of the radii of both pores. Red points denote local minima, and yellow points denote saddle points (**D**) Surfaces corresponding to five points along the energy minimizing pathway, corresponding to the white dots in (C).

If a second pore is unable to nucleate, the vesicle follows a single pore pathway, associated with a one-dimensional energy diagram. For the single pore membranes, the energy landscape is qualitatively similar to that seen in the two pore case. For large membranes ($\approx$ 10,000 $\mu m^2$) the energy minima is at zero pore size [Fig. 4.14A], indicating that vesicles are stable. For intermediate sized membranes ($\approx$ 7200 $\mu m^2$) the local energy minimum moves away from zero, corresponding to a contour with a single stable pore

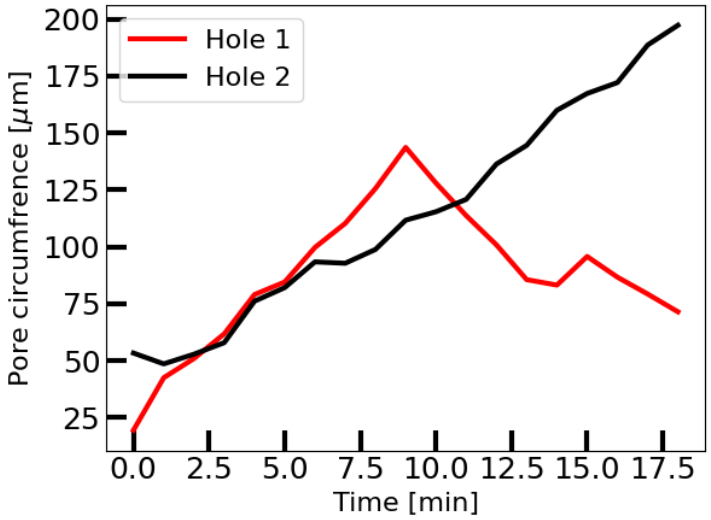


Figure 4.13: Circumference of both pores during two-pore disassembly. Pores are nearly identical, before symmetry is broken and one continues growing while the other shrinks.

[Fig. 4.14B]. The global minimum is once again a flat-membrane configuration, but the vesicle is prevented from unwrapping by a large energy barrier. At a smaller area ($\approx 6000$ $\mu m^2$) this energy barrier disappears, so that the membrane is able to smoothly unwrap to a flat membrane [Fig. 4.14C,D]. Taking equally-spaced configurations along the energy diagram produces shapes that qualitatively agrees with those seen in experiment.

As an additional comparison, we measured the membrane pore size as a function of area for experimental membranes and found that they transition to a period of rapid increase in radius at a critical area. This critical area is in quantitative agreement with the area at which the energy barrier disappears in numerical simulation (6080 $\mu m$) [Fig. 4.15].

Why a vesicle begins to unwrap via a one or two pore pathway has yet to be understood, but insight can be gained by studying the energy landscape. We note that the two pore configuration is at lower energy than the single pore configuration for a range of areas [Fig. 4.12B,C]. This qualitatively explains why the two pore pathway may occur: if

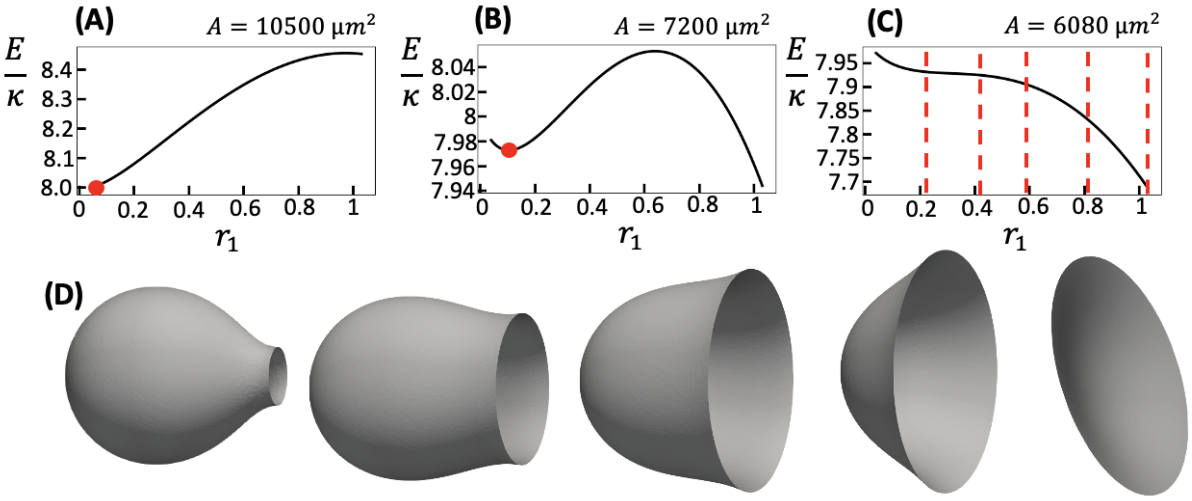


Figure 4.14: **Shrinking vesicles undergo shape change.** (**A**-**C**) Single pore energy landscape for decreasing surface areas. The reduced energy $\frac{E}{\kappa_c}$ as a function of the radii of both pores. Red points denote local minima, and yellow points denote saddle points (**D**) Surfaced corresponding to five points along the energy landscape, indicated with red lines in (C).

the vesicle is able to overcome the energy barrier associated with pore nucleation, there is a range of areas where a second pore will be preferred. When this second pore nucleates, the energy landscape will move the surface into a symmetric configuration, where both holes have the same size. Consequently, once this second pore is open the energy landscape constrains the energy-minimizing shape to follow the two-pore unwrapping process. Since pore nucleation is a dynamic process, we hypothesize that the dynamics of vesicle unwrapping is controlled by two time scales; the first is the rate of area change and the second is the time to nucleate a second pore. If the vesicle shrinks slowly, the second pore may have enough time to nucleate a second pore leading to the two-pore disassembly pathway.

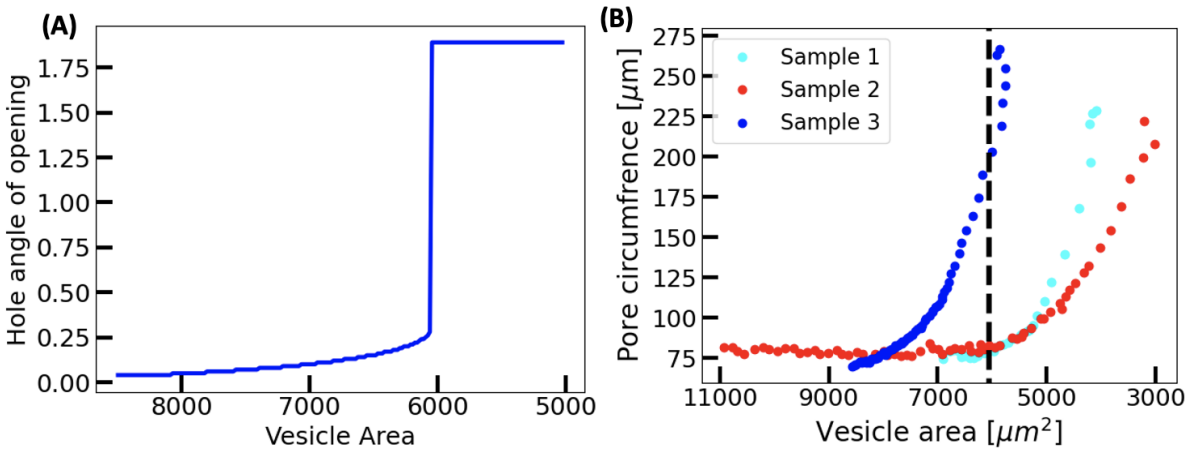


Figure 4.15: **Vesicle instability as a function of area.** (**A**) The opening angle of predicted energy-minimizing single-pore contours plotted as a function of membrane area. A rapid transitions to a flat membrane occurs at a critical area of $A^* = 6020\mu m^2$. (**B**) Size of the pores for experimental membranes as a function of area reveals a similar rapid change in pore size at a critical area. In multiple experiments, this critical point appears to occur at $A^* \approx 6000\mu m^2$ expected from the model (dashed line).

## 4.6 Discussion

The structure and dynamics of both colloidal and molecular membranes are described by the same coarse-grained principals, but different on length and time scales. Colloidal membranes enable high-resolution optical imaging, making them a valuable model system for studying general membrane physics. We demonstrate that colloidal membranes can form 3D vesicles. We have demonstrated that the shape vesicles take on are energy minimizing surfaces, given a fixed area and volume, and that dynamics are sufficiently slow to be considered quazistatic. Next, we outlined one pathway for closed vesicle formation, which follows an extension-then-fracture mechanism. Finally, we studied how membranes respond to continual shrinking, first by opening transient pores, and then by unwrapping back into a flt membrane.

Each of the experiments detailed here have potential for future work that will shed light on general membrane dynamics. For example, previous work has studied the dy-

namics of force-generated membrane tubes, and their biological relevance [105, 106, 107]. By studying colloidal pendent membranes pulled by gravity we can directly image details which would be nanometers in scale for lipid membranes. The size of colloidal vesicles and their constituent particles can be leveraged to extend the study of membrane tube formation. Sparse labeling of viral particles would enable particle flow tracking on the entire membrane surface as the pendent membrane extends. Similarly, the flow surrounding the membrane can be directly measured, opening the possibility for studying the hydrodynamic flows of both the membrane and the surrounding fluid throughout extension.

Another topic requiring further study is the observed transient pores. The pores observed here are similar to those formed in lipid vesicles in response to osmotic shock [108], mechanical stress [109] or electroportion [110]. However, the transient pores in colloidal vesicles last for tens of minutes, opening the possibility to study pore nucleation at the single-particle level. Finally, the ability to track the shape changes of disassembling membranes is unique to colloidal membranes. To observe similar dynamics in lipid membranes, one would need to shrink lipid membranes below $A^*$. For a lipid bilayer, with typical values of $\kappa_c \approx 20 k_B T$ and $\gamma \approx 50 pN$ [111] the critical radius $R^* = 12 nm$, significantly below optical resolution, obfuscating any shape changes associated with shrinking vesicles. Further study of this entirely new phenomena will elucidate understanding of the dynamics of a membrane subjected to a slowly-changing the energy landscape.

# Appendix A

# Appendix for 3D active nematic

## A.1 Materials

### A.1.1 Microtubule polymerization

Tubulin dimers were purified from bovine brains, through two cycles of polymerizations and depolymerizations in a high molarity PIPES buffer [112]. Tubulin was flash frozen and stored at -80 °C in M2B buffer (80 mM PIPES, pH 6.8, 1 mM EGTA, 2 mM $MgCl_2$). Tubulin was labeled with Alexa-Fluor 647-NHS (Invitrogen, A-20006) as previously described [113]. To induce polymerization, tubulin (80 $\mu$M in M2B) was mixed with 0.6mM GMCPP (Jena Biosciences, NU-4056) and 1mM dithiothreitol DTT in M2B. 3% of the tubulin was fluorescently labeled. The tubulin was first incubated for 30 min at 37°C, followed by an annealing step at room temperature for 6 hours. The GMPCPP stabilized microtubules have an average length of 1.5 $\mu$m [114]. The polymerized microtubules were then flash frozen and stored at -80°C.

### A.1.2 Assembly of kinesin clusters

K401-BIO-6xHIS is the 401 amino acid N-terminal domain derived from the Drosophila melanogaster kinesin-1 and labeled with a 6-his and a biotin tag. The motor proteins were transformed, expressed in Rosetta (DE3) pLysS *E. coli* cells, and purified as described previously [115]. The purified proteins were flash frozen in liquid nitrogen with 36% sucrose and stored at -80 °C. The K401 biotin-labeled motors were assembled into multimotor clusters using tetravalent streptavidin (ThermoFisher, 21122). We mixed 5 $\mu$L of 6.4 $\mu$M kinesin motors with 5.7 $\mu$L of 6.6 $\mu$M streptavidin (MW: 52.8 kDa) in 1.7:1 biotin to streptavidin ratio, and 0.5 $\mu$L of 5 mM dithiothreitol (DTT) in M2B (80 mM PIPES,pH 6.8, 1 mM EGTA, 2 mM $MgCl_2$). The clusters were then incubated on ice for 30 min, before being flash frozen and stored at -80C.

### A.1.3 PRC-1 purification

The truncated PRC1-NS$\Delta$C (MW: 58 kDa) was used to specifically crosslink microtubules while still allowing for their sliding. It consists of the first 486 amino acids of the full length PRC1 protein (MW: 72.5 kDa). The protein was transformed and expressed in Rosetta BL21(DE3) cells, and subsequently purified as described previously [116]. The truncated form of PRC1 has greatly increased stability, while maintaining the dimerization and the microtubule binding domaina and allowing for assembly of active fluids that exhibit chaotic flows [117].

### A.1.4 Colloidal virus purification

Filamentous virus fd-wt and fd-Y21M were purified andn characterized as described previously [118, 119]. All samples were stored in high salt 20 mM Tris buffer (pH 8.0, 100 mM NaCl). fd-Y21M forms a colloidal nematic liquid crystal phase as predicted by

the Onsager theory of hard rods [119].

### A.1.5 Assembling active nematic liquid crystal

We assembled active nematics by doping an *fd* colloidal liquid crystal with extensile microtubule bundles. A pre-mixture was prepared in a high salt M2B (M2B + 3.9 mM $MgCl_2$) containing an oxygen scavenging system (3.3 mg/mL glucose, DTT (5.5 mM), glucose oxidase (Sigma, G2133) and catalase (0.038 mg/mL, Sigma, C40)), 2nM Trolox to reduce photobleaching (Sigma, 238813), ATP (1420 uM), an ATP regeneration system (phosphoenol pyruvate (26 mM PEP, Beantown Chemical, 129745) and pyruvate kinase/lactate dehydrogenase enzymes (2.8% v/v PK/LDH, Sigma, P-0294)). We then added the kinesin clusters (121 nM Streptavidin), PRC-1 (200nM), *fd* viruses (25 mg/mL) and microtubules (13 $\mu$M). Typical samples consist of 7 mL of Premix, 3 mL of fd virus (100 mg/mL) and 2mL of microtubules (8 mg/mL). The samples are typically active for 3 hours. Passive samples were assembled using the same recipe but lacked both ATP and the kinesin clusters. The isotropic samples were obtained by assembling the previous recipe without fd-wt viruses. For SPIM imaging, the ATP concentration was reduced to 100 $\mu$M. The acquisition time (12 sec) of a 3D stack was small compared to the typical fluid velocity, which is less than 0.1 $\mu$m/sec.

## A.2 Imaging 3D nematic samples

### A.2.1 Widefield microscopy

Samples were imaged with an inverted microscope (Nikon Ti-E) equipped with a XYZ motorized stage, polarization optics, and a fluorescence imaging module. Simultaneous pictures of the birefringence and the fluorescent microtubules were obtained with a 20x

objective (Pan Fluor, NA 0.75) and a CCD camera (Andor, Clara E).

### A.2.2 Multiview-SPIM imaging

The 3D samples were imaged using multi-view light sheet microscopy [120]. Briefly, the microscope is composed of two detection and illumination arms. The detection arm is an epifluorescence microscope, consisting of a water-dipping objective (Apo LWD 25x, NA 1.1, Nikon Instruments Inc.), a filter wheel (HS-1032, Finger Lakes Instrumentation LLC), emission filters (BLP01-488R-25, BLP02-561R-25, Semrock Inc.), a tube lens (200 mm, Nikon Instruments Inc.), and an sCMOS camera (ORCA-Flash4.0 V3 Digital) with an effective pixel size of 0.26 $\mu$m. The illumination arm consisted of a water-dipping objective (CFI Plan Fluor 10x, NA 0.3), a tube lens (200 mm, both Nikon Instruments Inc.), a scan lens (S4LFT0061/065, Sill optics GmbH and Co. KG), a galvanometric scanner (6215 hr, Cambridge Technology Inc.), and two lasers (06-MLD 488 nm, Cobolt AB, and 660LX/LS OBIS 660 nm, Coherent Inc.). The FEP tubing is translated using a linear piezo stage (P-629.1cd with E-753 controller) and rotated using a rotational piezo stage (U-628.03 with C-867 controller) and a linear actuator (M-231.17 with C-863 controller, all Physik Instrumente GmbH and Co. KG). Samples were recorded using 4 views, by 900 rotated views, 200 slices with an optical sectioning of 2 $\mu$m, and a temporal resolution of either 12 or 20s depending if tracer beads were also imaged. Sample were mounted in a FEP tube of 800 $\mu$m inner diameter and sealed with NOA UV glue. The immersion water for the objectives was suplemented with 7.4% sucrose to mach the refractive index of the FEP tubing (n=1.344).

## A.3 Image processing

### A.3.1 Image post-processing: data fusion and deconvolution

Image processing was performed using Matlab, Fiji and associated multi-view deconvolution plugin [121, 122]. The light sheet data was unpacked and binned (2*2 binning, spatial resolution of 0.52 $\mu$m after binning) using a custom made Matlab program. To ensure a correct measurement of the microtubule orientation, we first removed distortions introduced by an anisotropic point-spread function (PSF) - SPIM being subject to optical aberration. We deconvolved the four views post-acquisition using an empirical PSF measured on passive fluorescent particles immersed in the active LC (20 iterations). Finally, the same markers were used to register the four complementary views of sample taken at 90 deg rotation intervals, which also reduced the effect of the anisotropic PSF.

### A.3.2 3D Orientation analysis

The 3D nematic director field was extracted by computing the local structure tensor in 3D with a custom-made Matlab code. This method has been described previously for 2D samples [123]. The Gaussian window size was $\approx$6 $\mu$m. Choosing the right window size is important for corect detection of the topological defects. Choosing a smaller window size resulted in false positives. Choosing a larger window size led to smoothing of the nematic director, and increased the number of undetected defects. To find the defects, we first computed the distortion energy in the one-elastic constant approximation, approximating spatial partial derivatives $\partial_i$ with finite differences. We did not measure $(\partial_i n_j)(\partial_i n_j)$. Instead we measured $(\partial_i [n_j n_k])(\partial_i [n_j n_k])$. In principle these two provide the same information. However, the first option picks up a large artificial derivative when n flips to -n, and then squares that derivative. The second option fixes the n =

-n problem by taking derivatives of $n_j n_k$ instead of just $n_j$, removing the large artificial derivatives. We then looked at the winding of the director field where the distortion energy was greater than a 0.5 threshold. We verified that the defects' detection did not depend on the energy threshold chosen. We manually verified that the defects observed in the nematic field correspond to disclinations in the fluorescent microtubule channel. We found that about 20% of the detected defects were false positives, principally due to a low signal/noise ratio in regions where the light sheet is not in focus (on the edge of the FOV).

## A.4 Data analysis

### A.4.1 Identifying defect loops in director fields

We identify the defect set in a voxelated director field as the set of all voxels where the magnitude of the gradient in the director, $|\nabla \mathbf{n}| = \sqrt{\partial_i n_j \partial_i n_j}$, exceeds a threshold, typically 0.5–0.6. The defect set is divided into its connected subsets, each of which is a defect. To differentiate loops from other defect structures, we filter these connected subsets by their topological genus. The genus, $g$, which counts the number of holes, can be computed from the Euler characteristic, $\chi$, through the relation $\chi = 2-2g$. Because a connected subset is a collection of cubic voxels, we can treat the subset as a polyhedron. Then, we can compute the Euler characteristic as

$$\chi = V - E + F, \tag{A.1}$$

where $V$, $E$, and $F$ are the number of vertices, edges, and faces of the polyhedron, respectively.

A connected subset $\mathcal{D}$ is a collection of cubic voxels which has an easily counted

number of vertices, edges, and faces, from which we calculate the Euler characteristic. To avoid spurious one-voxel holes, we inflate $\mathcal{D}$ by adding to it all of the nearest-neighbor voxels to each of the original voxels of $\mathcal{D}$ (without repetition). The computation of the Euler characteristic can be sped up using pre-computed information about possible voxel cluster motifs [124, 125]. From the Euler characteristic we obtain the genus and identify loops as connected subsets with $g = 1$.

### A.4.2 Calculating a loop core

Once a connected defect subset $\mathcal{D}$ has been identified as a loop, we obtain the director profiles and calculate $\mathbf{\Omega}$ at several points on the loop. We first identify a loop core, a one-voxel-thick thread through the disclination contour, to guarantee a nontrivial winding of the director field in a small circuit around the disclination. Our algorithm to compute the defect loop core $\mathcal{C}$ chooses a starting point $\mathbf{x}_{\text{start}}$ as the location of the smallest value of nematic order $S$ (simulation) or the largest value of $|\nabla \mathbf{n}|$ (experiment) in the connected subset. Then, successive points in the loop core are chosen as follows:

1. Construct a list $\{\mathbf{x}_i\}_{\text{elig.}}$ of eligible next points in $\mathcal{C}$, choosing from among the nearest-neighbor points to the most recently added point $\mathbf{x}_{\text{prev}}$ in $\mathcal{C}$, and selecting only those neighbors that are members of $\mathcal{D}$ but not already members of $\mathcal{C}$. Exclude any points that are in the list $\{\mathbf{x}_i\}_{\text{excl.}}$ of excluded points (defined below). Further specify that $\{\mathbf{x}_i\}_{\text{elig.}}$ cannot include any point that is a nearest neighbor of any point already in $\mathcal{C}$ besides $\mathbf{x}_{\text{prev}}$ and $\mathbf{x}_{\text{start}}$, unless this requirement leaves zero eligible next points in $\{\mathbf{x}_i\}_{\text{elig.}}$.

2. If $\mathbf{x}_{\text{prev}}$ is not a nearest neighbor of $\mathbf{x}_{\text{start}}$, but at least one of the eligible next points in $\{\mathbf{x}_i\}_{\text{elig.}}$ *is* a nearest neighbor of $\mathbf{x}_{\text{start}}$, then choose one of those points neighboring $\mathbf{x}_{\text{start}}$ as the next point $\mathbf{x}_{\text{next}}$ in $\mathcal{C}$ in order to close the loop. Otherwise,

choose the next point $\mathbf{x}_{\text{next}}$ according to smallest $S$ or largest $|\nabla \mathbf{n}|$ among the options in $\{\mathbf{x}_i\}_{\text{elig.}}$. Append $\mathbf{x}_{\text{next}}$ to $\mathcal{C}$. If this operation is not possible because there are no eligible next points in $\{\mathbf{x}_i\}_{\text{elig.}}$, then we have made a wrong turn; we therefore remove $\mathbf{x}_{\text{prev}}$ from $\mathcal{C}$, place $\mathbf{x}_{\text{prev}}$ in the list of excluded points $\{\mathbf{x}_i\}_{\text{excl.}}$, and return to step 1 with $\mathbf{x}_{\text{prev}}$ taken from the previous iteration.

3. If $\mathbf{x}_{\text{next}}$ is a nearest neighbor of $\mathbf{x}_{\text{start}}$, and $\mathcal{C}$ contains at least ten points, then we consider the loop core closed. Otherwise, we repeat steps 1-2 until $\mathcal{C}$ is closed.

By following the path of largest $|\nabla \mathbf{n}|$ or smallest $S$, the loop core advances through the connected subset until it closes. In some instances steps 1-3 produce a curve that does not thread through the defect loop, but instead forms a small loop in one portion of the defect subset. In these cases we run the algorithm again with a different starting point, chosen by the next-largest $|\nabla \mathbf{n}|$ value or next-smallest $S$ value in $\mathcal{D}$. To obtain the loop normal $\mathbf{N}$, the loop core is fit to a circle, and the normal to the plane of the circle serves as $\mathbf{N}$. An arbitrary choice of sign for $\mathbf{N}$ determines the positive sense of rotation around the loop. The local tangent vector $\mathbf{t}$ to the disclination is determined by the vector difference between next and previous points in the loop core, with sign chosen by the positive sense of rotation.

### A.4.3 Calculating the rotation vector and reference director

To calculate $\boldsymbol{\Omega}$ at a given point $P$ on the loop core, we first make a collection of directors $\{\mathbf{n}(\mathbf{x}_i)\}$ from points $\{\mathbf{x}_i\}$ that are near $P$ and nearly in the plane $\Theta$ transverse to $\mathbf{t}$. More specifically, $\{\mathbf{x}_i\}$ is the set of points with separation vector $\mathbf{d}_i$ from $P$ satisfying $d_{\min} \leq |\mathbf{d}_i| \leq d_{\max}$ and $|\arccos(\mathbf{d}_i \cdot \mathbf{t})| > \psi_{\min}$. We use $d_{\min} = 3$, $d_{\max} = 7$, and $\psi_{\min} \approx 0.61 \times (\pi/2)$, where lengths are given in units of the voxel spacing.

Next, for each point $\mathbf{x}_i$, we project $\mathbf{d}_i$ into the transverse plane $\Theta$, $\mathbf{d}_i^{\perp} = \mathbf{d}_i - \mathbf{t}(\mathbf{d}_i \cdot \mathbf{t})$,

to obtain an angle $\phi_i$ in the plane relative to a fixed reference direction. The collection of directors $\{\mathbf{n}(\mathbf{x}_i)\}$ is then plotted on the unit sphere in order of $\phi_i$. A semi-circle is fitted to the path traced out by this ordered collection of directors, with a definite orientation given by the positive sense of rotation in $\Theta$, whose positive normal direction is aligned with $\mathbf{t}$. We thus compute $\mathbf{\Omega}$ as the positive normal direction to this fitted semi-circle on the unit sphere. We also take the reference director $\mathbf{n}_{\text{out}}$ to be the $\mathbf{n}(\mathbf{x}_i)$ at the point $\mathbf{x}_i$ in the collection for which $\mathbf{d}_i$ is most nearly outward from the center of the circle fitted to the loop. Any small component of this $\mathbf{n}(\mathbf{x}_i)$ along $\mathbf{\Omega}$ is projected out to obtain $\mathbf{n}_{\text{out}}$.

### A.4.4 Calculating disclination loop topology

We measure the topological index $\nu$ of a disclination loop, defined in the Supplementary Text, as follows: At roughly even intervals around a loop separated by angle $\Delta\phi$, we calculate $\mathbf{\Omega}$ and $\mathbf{n}_{\text{out}}$ to find the frame $\mathbf{F}(\phi)$ at each step. We record the $SO(3)$ rotation operation $\mathbf{R}_{\phi,\phi+\Delta\phi}$ that takes $\mathbf{F}(\phi)$ into $\mathbf{F}(\phi+\Delta\phi)$ and use $\Delta\phi$ between $2\pi/12$ and $2\pi/8$. Expressing $\mathbf{R}_{\phi,\phi+\Delta\phi}$ as a rotation by angle $\alpha$ about an axis $\hat{a}$, we convert the rotation to a quaternion $q_{\phi,\phi+\Delta\phi} = \cos(\alpha/2)1 - \sin(\alpha/2)(\hat{a}\cdot\vec{\sigma})$, where $\vec{\sigma} = i\hat{x} + j\hat{y} + k\hat{z}$ (borrowing from the Pauli matrix language). The product $q_{0,2\pi} = \prod_{\phi=0}^{2\pi-\Delta\phi} q_{\phi,\phi+\Delta\phi}$ identifies the loop with one of the cases named in Sec. A.5, as $q_{0,2\pi}$ must be one of the following: 1 (unlinked and neutral), $-1$ (unlinked and charged), or a quaternion satisfying $q^2 = -1$ (linked).

## A.5 Theoretical calculations

### A.5.1 Rotation vector

The rotation vector $\mathbf{\Omega}$ used in this work is the rotation angle specifying the symmetry operation in order parameter space, $\mathbb{R}P^2$, undergone by the director $\mathbf{n}(\mathbf{x})$, on a small

closed measuring circuit $C$ around the disclination at the point of interest [126]. For all disclinations studied in this work, the angle of rotation is $|\mathbf{\Omega}| = \pi$, which corresponds to topological winding numbers of $\pm$ 1/2. The axis of rotation, $\hat{\mathbf{\Omega}} \equiv \mathbf{\Omega}/|\mathbf{\Omega}|$, is determined from the closed loop $\Gamma$ in $\mathbb{R}P^2$ traced out by $\mathbf{n}$ on the measuring circuit $C$. Because $\Gamma$ is, in general, approximately a semi-great circle, $\hat{\mathbf{\Omega}}$ is simply the normal to the semi-circle, with sign given by the positive sense of rotation on $\Gamma$ as $C$ is traversed in the positive sense (Fig. 2D). Near the defect point of interest, $\mathbf{n}$ is (approximately) confined to the plane orthogonal to $\mathbf{\Omega}$. We can form an orthonormal triad $\{\mathbf{n}_0, \mathbf{n}_1, \hat{\mathbf{\Omega}}\}$ such that, along $C$, $\mathbf{n}$ rotates from $\mathbf{n}_0$ through $\mathbf{n}_1$ into $-\mathbf{n}_0$.

### A.5.2 Topological classification of disclination loops

The classification of topological defects in this work follows the standard application of homotopy theory to nematics. Disclination loops, like hedgehog point defects, carry an integer hedgehog charge:

$$d = \frac{1}{4\pi} \int_{\mathbb{S}^2} d\theta d\phi \, \mathbf{n} \cdot [\partial_\theta \mathbf{n} \times \partial_\phi \mathbf{n}], \tag{A.2}$$

identifying the defect with an element of the second homotopy group $\pi_2(\mathbb{R}P^2) \cong \mathbb{Z}$ [127].

Whereas hedgehogs with different $d$ are topologically distinct, for disclination loops the topological categorization depends only on $d$ modulo 2 [127].

We refer to loops with even $d$ as topologically neutral, because shrinking a $d = 0$ loop to a point leaves behind a locally defect-free director field.

The topological information about a disclination loop is obtained using a meauring torus $\mathbb{T}^2$ enclosing the defect. Maps from $\mathbb{R}P^2$ to $\mathbb{T}^2$ are divided into four topologically distinct classes with a $\mathbb{Z}_4$ group structure when joining loops together [128].

We classify a disclination loop's topology by recording $\mathbf{\Omega}$ and $\mathbf{n}_{\text{out}}$, which together

specify the disclination profile, at several sampled points along the disclination's length. The choice of $\mathbf{n}_{\text{out}}$ as reference director follows the canonical choice of tracking $\mathbf{n}$ along a cycle of the torus unlinked with the disclination [128]. Together, $\{\mathbf{n}_{\text{out}}, \mathbf{n}_{\text{in}}, \hat{\mathbf{\Omega}}\}$ define an orthonormal frame $\mathbf{F}$, where $\mathbf{n}_{\text{in}} \equiv \hat{\mathbf{\Omega}} \times \mathbf{n}_{\text{out}}$ is the director on the inner side of the loop. Importantly, $\tilde{\mathbf{F}} \equiv \{-\mathbf{n}_{\text{out}}, -\mathbf{n}_{\text{in}}, \hat{\mathbf{\Omega}}\}$ gives the same profile as $\mathbf{F}$ because of the $\mathbf{n} \equiv -\mathbf{n}$ symmetry of the director. From point to point on a disclination loop parametrized by angle $\theta$, the frame $\mathbf{F}$ rotates according to $\mathbf{F}(\theta_{i+1}) = \mathbf{R}_{i,i+1}\mathbf{F}(\theta_i)$, where $\mathbf{R}$ is an element of the group $SO(3)$ of rotations of a 3D rigid body. Upon traversing the loop completely, $\mathbf{F}(\theta = 2\pi)$ must return to either $\mathbf{F}(\theta = 0)$ or $\tilde{\mathbf{F}}(\theta = 0)$. In the latter case, the disclination loop is linked by another disclination loop (or an odd number of them), a situation that we do not observe in experimental or simulated active nematics. If $\mathbf{F}$ returns to itself, then the loop is unlinked, and falls into the even-$d$ or the odd-$d$ class.

Let $\Upsilon$ be the path in $SO(3)$ representing the composition of all the rotations between $N$ sampled points, $\mathbf{R}_{0,2\pi} = \mathbf{R}_{0,\theta_1}\mathbf{R}_{\theta_1,\theta_2}\cdots\mathbf{R}_{\theta_{N-1},2\pi}$. To topologically classify these paths, we lift $\Upsilon$ from $SO(3)$ to the simply connected covering space $SU(2)$, which can be parametrized by the unit quaternions ($\pm i$, $\pm j$, $\pm k$, $\pm 1$, and their multiplicative products). Following the spirit of Ref. [129], we choose a parametrization in which $\pm k$ represent the rotation of $\mathbf{n}_{\text{out}}$ by $\pi$ about $\pm\mathbf{\Omega}$. The set of all possible total rotations $\mathbf{R}_{0,2\pi}$ is then represented by $\{1, k, -1, -k\} = k^\nu$, $\nu \in \{0, 1, 2, 3\}$

$(30, 48)$, forming a group under multiplication with the requisite $\mathbb{Z}_4$ structure.

The mod-4 integer $\nu$ provides a topological index for the loop: topologically neutral loops have $\nu = 0$, topologically charged loops have $\nu = 2$, and the linked-loop scenario corresponds to $\nu = 1$ or 3.

Disclination loops with approximately uniform $\mathbf{\Omega}$ and $\mathbf{n}_{\text{out}}$, which are the focus of this work, are trivially $\nu = 0$ loops, and therefore neutral and unlinked. The practical application of this theory, to calculate $\nu$ in observed disclination loops, is described in

Materials and Methods (A.1).

### A.5.3 A local formula for $\beta$

Experimental and simulated defect sets presented in this work are color-coded by $\beta$, the angle between rotation vector $\mathbf{\Omega}$ and unit tangent $\mathbf{t}$. The tangent vector is calculated straightforwardly from the separation between neighboring points on the disclination contour. We compute $\mathbf{\Omega}$ and thus $\beta$ from $\mathbf{n}$ in a circuit around the loop of interest as described in Sec. A.4.3. The small measuring circuit makes this calculation non-local in a mild way, which is feasible for individual loops but less practical for datasets of many defects.

We also used an alternative, purely local calculation of $\mathbf{\Omega}$ that agrees well with the non-local calculation: The direction of $\mathbf{\Omega}$ is estimated to be parallel to:

$$\tilde{\mathbf{\Omega}} \equiv \nabla \times \mathbf{n} - \mathbf{n}(\mathbf{n} \cdot \nabla \times \mathbf{n}) = \mathbf{n} \times [(\mathbf{n} \cdot \nabla)\mathbf{n}] \tag{A.3}$$

wherever $\tilde{\mathbf{\Omega}}$ has nonzero magnitude. The assumption $\mathbf{\Omega} \parallel \tilde{\mathbf{\Omega}}$ can be justified since they are exactly parallel for a straight disclination along the $z$-axis with uniform $\mathbf{\Omega}$, and with an idealized director field profile given by

$$\mathbf{n} = \hat{p}_1 \cos(\phi/2) + \hat{p}_2 \sin(\phi/2) \tag{A.4}$$

which produces a $\pi$ winding of $\mathbf{n}$ about an arbitrary $\tilde{\mathbf{\Omega}}$. Here, $\phi$ is the angle in the $xy$ plane, and $\{\hat{p}_1, \hat{p}_2, \hat{\mathbf{\Omega}}\}$ is an orthonormal triad.

We therefore expect $\tilde{\mathbf{\Omega}}$ to be a good approximation to the direction of $\mathbf{\Omega}$ except where the disclination is strongly curved, has a rapidly varying $\mathbf{\Omega}$, or has $\beta = \pi/2$ exactly (in which case $\tilde{\mathbf{\Omega}}$ has zero length). In contrast to the non-local measurement of

$\boldsymbol{\Omega}$ on a circuit, $\tilde{\boldsymbol{\Omega}}$ is a local measurement depending only on neighboring voxels for finite difference calculations of first derivatives of $\mathbf{n}$.

A separate measure is needed to choose between $\tilde{\boldsymbol{\Omega}}$ and $-\tilde{\boldsymbol{\Omega}}$ for the direction of $\boldsymbol{\Omega}$, because Eq. A.3 is odd in $\mathbf{n}$. We use the saddle-splay energy density expression:

$$\tilde{f}_{24} \equiv \nabla \cdot [(\mathbf{n} \cdot \nabla)\mathbf{n} - \mathbf{n}(\nabla \cdot \mathbf{n})]. \tag{A.5}$$

Applying this expression to the ideal disclination director field of Eq. A.4 shows that $\tilde{f}_{24}$ is positive at a $+1/2$ wedge profile, negative at a $-1/2$ wedge profile, and zero at a twist profile [130]. We find that $\tilde{f}_{24}$ alone is not a reliable measure of $\beta$ in the data, but that we can use the sign of $\tilde{f}_{24}$ to fix the sign of $\tilde{\boldsymbol{\Omega}}$ relative to the tangent. With this combination of $\tilde{\boldsymbol{\Omega}}$ and $\tilde{f}_{24}$, we obtain an estimate of the direction of $\boldsymbol{\Omega}$ with the correct sign of $\boldsymbol{\Omega} \cdot \mathbf{t}$, from which we obtain the angle $\beta$.

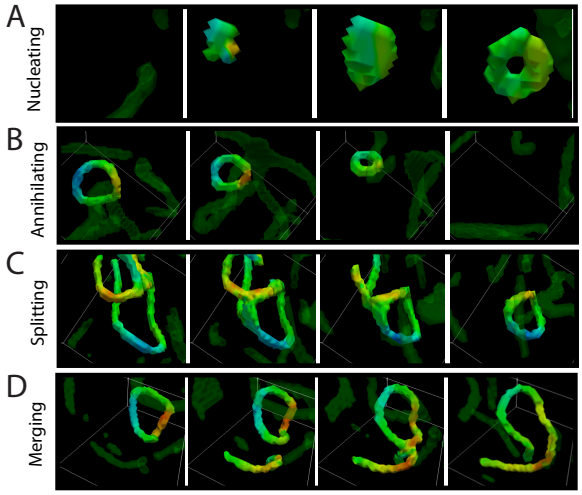


Figure A.1: **Dynamics of disclination loops observed in hybrid lattice Boltzmann simulations.** (**A**) Loop nucleation from a defect-free region. (**B**) Loop self-annihilation leaves behind a defect-free nematic. (**C**) A disclination line self-intersects and splits, emitting a loop. (**D**) A disclination loop merges with a disclination line. Coloring of the disclinations indicates $\beta$.

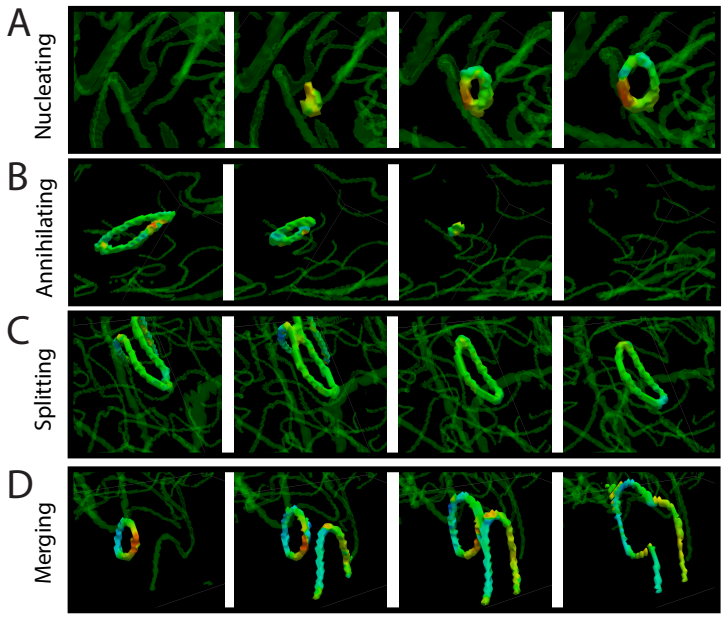


Figure A.2: **Dynamics of disclination loops observed in finite difference simulations.** (**A**) Loop nucleation from a defect-free region. (**B**) Loop self-annihilation leaves behind a defect-free nematic. (**C**) A disclination line self-intersects and splits, emitting a loop. (**D**) A disclination loop merges with a disclination line. Coloring of the disclinations indicates $\beta$.

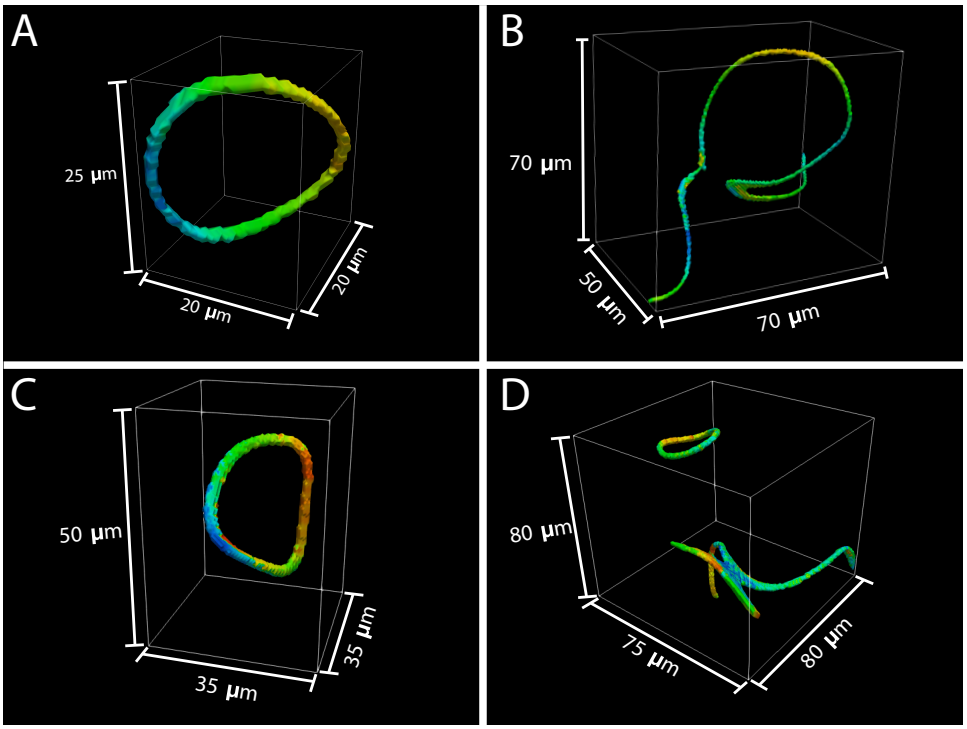


Figure A.3: **Scale of the loops shown in Fig. 2.** Bounding boxes are shown to give the scale of the (**A**) nucleation event, (**B**) splitting event, (**C**) annihilation event and (**D**) merging event. Coloring of the disclinations indicates $\beta$.

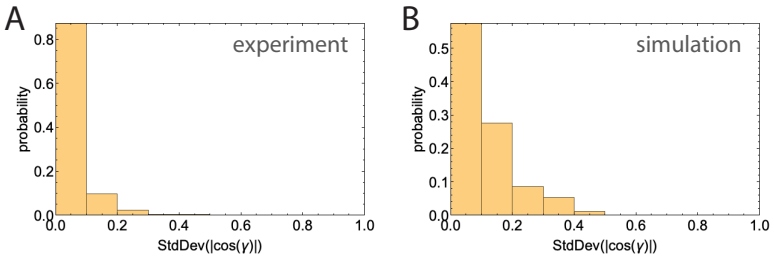


Figure A.4: **Disclination loops have nearly uniform $\boldsymbol{\Omega}$ and $\mathbf{n_0}$** Wider distribution of $|\cos(\gamma)|$ indicate more non-uniform loops. $|\cos(\gamma)|$ is the locally calculated angle between the loop normal and $\boldsymbol{\Omega}$. Each standard deviation value pertains to one loop, with $\boldsymbol{\Omega}$ calculated at 8 to 12 approximately evenly spaced points along the loop contour. N=268 for experimental loops and N=94 for simulated loops.

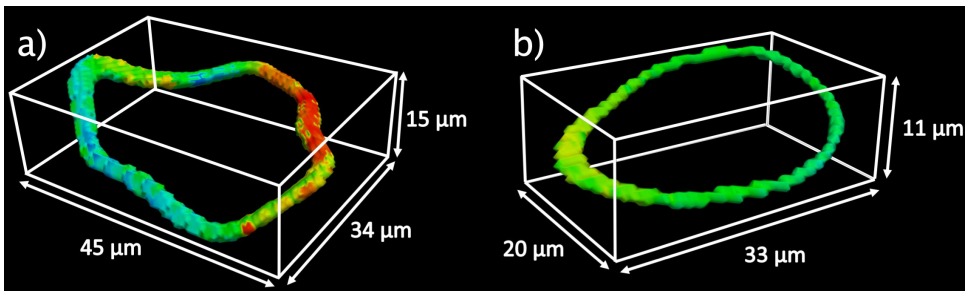


Figure A.5: **Fig. S5: Scale of the disclination loops.** Bounding boxes show the scale of the experimental wedge-twist (**A**) and pure twist loop (**B**) shown in Figure 4. Disclination coloring indicates $\beta$.

# Appendix B

# Appendix for active LLPS

## B.1 Material preparation

### B.1.1 Dextran fractional precipitation.

Control of LLPS required low-polydispersity, high-molecular-weight dextran. Dextran (1.5-2.8 MDa, Sigma-Aldrich) was separated into fractions of narrow molecular weight distributions via ethanol precipitation. Ethanol was gradually added to a solution of 0.2% dextran under vigorous stirring at 23 °C. After reaching 31% (w/w) ethanol, precipitates were removed by centrifugation (20 min at 17,000g, Fiberlite F9-6 x 1000 LEX fixed angle rotor, Thermo Scientific). Ethanol was then added to a concentration of 32% (w/w). The precipitate was collected by centrifugation and resuspended in water. Solvent was removed via lyophilization, and the powder was reconstituted in water to 20% (w/w) dextran. This stock solution was used to make LLPS solutions.

### B.1.2 PEG-dextran LLPS.

Polymers of high molecular weight chosen to create mixtures that are both active and phase separated. Inter-microtubule sliding occurs in a finite polymer concentration range, where depletion forces are sufficiently strong to induce microtubule bundling without friction [131]. Mixtures comprising 2.38% (w/w) fractionated dextran and 1.55% (w/w) poly(ethylene glycol) (PEG) (35 kDa, EMD Millipore), reconstituted in M2B buffer (80mM K-pipes, 2mM $MgCl_2$, 1mM EGTA, pH 6.8), enabled both phase separation and motor-driven inter-filament sliding. To distinguish the two phases, 2,000 kDa amino-Dextran (Fina Biosolutions) was labeled with Alexa-Fluor 488 NHS Ester (ThermoFisher Scientific) and was added at a final concentration of $< 0.1\%$ (w/w).

To characterize the LLPS, we let mixtures completely phase separate under gravity for one day. Top (PEG-rich) and bottom (dextran-rich) phases were extracted, and their densities were measured using a density meter (DMA 4100, Anton-Paar). The densities of the dextran and the PEG phases were $\rho_P = 1.0151 g/mL$ and $\rho_D = 1.024 g/mL$ respectively. The viscosity of each phase was determined by microrheology [132]. The viscosities of the PEG-rich and the dextran-rich phases were $\eta_P = 5\text{mPa}\,\text{s}$ and $\eta_D = 25\text{mPa}\,\text{s}$ respectively. Interfacial tension between the two phases was determined from the exponential decay length of the capillary rise next to a polyacrylamide coated wall. At low KSA concentrations, the decay length was $l_e = 45\mu\text{m}$ [Fig. 3.8C, inset]. The relation $l_e = l_c = \sqrt{\gamma/\Delta\rho g}$, where the density difference is $\Delta\rho = \rho_D - \rho_P$, and $g$ is the acceleration of gravity, yields the interfacial tension $\gamma = 0.18\mu\text{N/m}$.

### B.1.3 Chamber preparation.

Chambers were constructed of glass slides that were coated with a PEG brush (mPEG 5k-silane, BiochemPEG) [133]. PEG-coating resulted in preferential wetting by the pas-

sive PEG phase. Achieving a uniform coating was essential to prevent pinning of the dextran phase to the chamber walls. Glass was cleaned by sonicating in 1% Hellmanex, and then etched in 0.5 M NaOH for 30 minutes. Slides were dried at 90 $^{\circ}C$ in the presence of a desiccant for 10 minutes. Silanized PEG, reconstituted in anhydrous DMSO to a concentration of 5%, was sandwiched between glass slides and left to react for 30 minutes at 90 $^{\circ}C$. Slides were then rinsed in water and dried with a nitrogen stream. Chambers were assembled immediately. For wetting experiments, #0 coverslips were coated with polyacrylamide according to established protocol [134]. Chambers were constructed by sandwiching two polyacrylamide coated coverslips between PEG-coated slides.

### B.1.4 PEG-dextran active-LLPS.

We assembled active-LLPS by adding the phase-separating polymers to microtubules and clusters of kinesin motors. Kinesin K401-streptavidin (KSA) motor clusters and GMPCPP-stabilized microtubules were purified and prepared as described previously [135]. The active mixture was prepared in M2B buffer containing antioxidants (2 mM Trolox, 3.3 mg/mL glucose, 5 mM DTT, 200 $\mu$g/mL glucose oxidase and 35 $\mu$g/mL catalase) to reduce photobleaching, ATP (1420 uM), an ATP regeneration system (26 mM phosphoenol pyruvate (Beantown Chemical, 129745) and 2.8% (v/v) pyruvate kinase/lactate dehydrogenase enzymes (Sigma, P-0294)). We added microtubules to a final concentration of 0.67 mg/mL and KSA at variable concentration.

## B.2 Methods

### B.2.1 Correlation length evolution in phase separation experiments.

To quantify the phase separation dynamics, images of dextran fluorescence were thresholded at each time point to produce a binary intensity map $I(\vec{r},t)$, where $I = 1$ for dextran-rich domains and $I = -1$ for PEG-rich domains, and the radius $\vec{r} = (x, y)$ [Fig. B.3A,B]. The two-point correlation function $C(\Delta\vec{r},t) = \langle I(\vec{r}+\Delta\vec{r},t)I(\vec{r},t)\rangle$ was azimuthally averaged to produce the radial correlation function $C(r,t)$. The correlation length $\xi(t)$ was defined such that $C(r = \xi(t),t) = 0.5$ [Fig. B.3C,D], and its evolution was tracked [Fig. B.3E].

### B.2.2 Evolution of correlation length and interface curvature at 230nM KSA.

In samples approaching a steady state, increase in the interface curvature preceded the decay of the correlation length. Local interface curvatures were computed as

$$\kappa = \frac{f_{xx}f_y^2 - 2f_{xy}f_xf_y + f_{yy}f_x^2}{(f_x^2+f_y^2)^{3/2}} \tag{B.1}$$

where $f(x, y)$ is the dextran fluorescence intensity at pixel $(x, y)$ and subscripts denote partial derivatives [136]. $\kappa$ was averaged over all interfaces in the field of view at each time point. Initially, the average curvature increased before the correlation length started to decay [Fig. B.5]. The correlation length evolution lagged by 30 min behind the average interface curvature for the first 1.5 hours of the experiment. After 2 hours, both correlation length and inverse curvature evolved synchronously as the system approached

steady state.

### B.2.3 Detection of bulk-phase-separated interfaces.

Interfaces were detected using a multi-step procedure:

(1) Dextran fluorescence images were divided by a background image, thresholded, and numerically differentiated to extract domain edges. Edges that straddle the image horizontal axis were selected, skeletonized, and pruned to produce an initial contour at single pixel resolution [Fig. B.6A-C].

(2) For each point on the contour $(x, y)$, image intensity is interpolated at sub-pixel resolution along the local interface normal $(n_x, n_y)$ in a 5x5 pixel neighborhood of $(x, y)$. Sub-pixel interface position along the normal is defined so that the interpolated image intensity equals the threshold [Fig. B.6D-H].

(3) The local tangent angle to the interface $\theta = \tan(\Delta y/\Delta x)$ is found by finite differences, and the contour is re-parameterized with the arc-length parameter $s$.

(4) The total arc length of the interface is measured for each time point. Due to interface deformations, the total arc length fluctuates in time. For computing correlations and Fourier transforms, tangent angle data from a single experiment $\theta(s, t)$ is trimmed so that the interface at each time point has the same total arc length.

### B.2.4 Power spectra of interface fluctuations.

Interface tangent angles $\theta(s, t)$ were used to compute the spatiotemporal autocorrelation function $R_\theta(\Delta s, \Delta t) = \langle \theta(s + \Delta s, t + \Delta t)\theta(s, t)\rangle$, where $\langle\rangle$ denotes averaging over an arc-length interval of 3.1 mm and time interval of 2 hours. The power spectrum was then computed as $S(k) = \int ds e^{-iks} R_\theta(s, \Delta t = 0)$.

### B.2.5 Dynamic structure factor (DSF) of interface height.

Local interface height was sampled as a function of the horizontal coordinate $x$ and time $t$. The spatiotemporal autocorrelation function of interface height $R_h(\Delta x, \Delta t) = \langle h(x+\Delta x, t+\Delta t)h(x,t)\rangle$ was calculated by cross correlating a rectangular window $\Delta x_m < x < X - \Delta x_m, \Delta t_m < t < T - \Delta t_m$ of $h(x,t)$ with the complete sample, where $X$ and $T$ denote the sample size and duration. $\Delta x_m$ and $\Delta t_m$ denote maximum lag distance and time respectively. The values of the parameters were $X = 10.7\ mm, T = 2\ hr, \Delta x_m = 1mm, \Delta t_m = 0.36hr$ for experiments; for simulations they were $X = 2\ mm, \Delta x_m = 0.67\ mm$, and $T = 0.44, 0.22, 0.11\ hr, \Delta t_m = 0.3, 0.15, 0.0755\ hr$ for activity values $\alpha = 10, 20, 40$ mPa respectively. The DSF was then computed by multiplying the result of auto-correlation with a 2D Hanning window, and taking the Fourier transform of the result in both space and time.

### B.2.6 Extraction of the wave dispersion relation.

Wave dispersion $\omega_p(k)$ was extracted from the DSF in two ways. Above a wave-number $k_{min}$, the DSF for a constant $k$ exhibited a peak at a frequency $\omega = \omega_p(k)$. The peak position was detected by modelling the DSF with a sum of Lorentzians, one centered at $\omega = 0$ and the other at $\omega = \omega_0$:
$F(\omega) = a\,((1-c)/((\omega/b)^2+1) + c/((\omega/\omega_0)^2-1)^2 + (\omega\Delta\omega/\omega_0^2)^2)$, where $a, b, c, \omega_0$ and $\Delta\omega$ are adjustable parameters. The frequency peak was $\omega_p = \sqrt{\omega_0^2 - \Delta\omega^2/2}$. For $k < k_{min}$, the dispersion relation was detected by finding the wave number at which the DSF is at maximum for a constant frequency.

### B.2.7 Power spectra of active fluid velocity.

To find the velocity of the active phase, two-color fluorescent images were taken of both the Alexa Fluor 488 labeled dextran and the Alexa Fluor 647 labeled microtubules. A mask of the active phase was found by thresholding the dextran channel. This mask, along with the accompanying microtubule images, were imported into the MATLAB plugin PIVLab [137]. Particle Image Velocimetry was preformed on the microtubule bundle images to find the velocity of the active phase.

Active bulk fluid velocity was calculated in a 2.5 mm X 2 mm window that was 100 microns below the interface. The vectorial velocity field $\mathbf{v}$, sampled in 10 sec intervals over 1.5 hours, 5 hours after the beginning of the experiment, was used to obtain the spatiotemporal autocorrelation function $R_{\mathbf{v}}(\Delta\mathbf{r}, \Delta t) = \langle \mathbf{v}(\mathbf{r} + \Delta\mathbf{r}, t + \Delta t) \cdot \mathbf{v}(\mathbf{r}, t) \rangle_{\mathbf{r},t}$, where the radius is $\mathbf{r} = (x, y)$. The autocorrelation was azimuthaly averaged to produce the radial autocorrelation function $R_{\mathbf{v}}(r, t)$. Fig. S13 depicts sections of $R_{\mathbf{v}}(r, t)$ at $t = 0$ and $r = 0$ to extract correlation length and time scales.

### B.2.8 Measuring the center-of-mass of active fluid capillary rise.

In wetting experiments and simulations, the center-of-mass height of the active fluid that is adjacent to the wall is defined as follows: (1) Interface profile is detected using thresholding as in Fig. B.6. The average height $Y_0$ of the bulk interface far from the wall ($> 5l_e$) is set as zero height. (2) Pixels above threshold whose height is greater than $Y_0$, and are within $5l_e$ of the wall are included in the center-of-mass height determination. The center of mass is defined as $Y_{cm} = \frac{1}{N}\sum_i (Y_i - Y_0)$, where N is the total number of pixels.

## B.3 Numerical model

### B.3.1 Multiphase hydrodynamic model.

To simulate activity-powered interfaces, we use a VOF (Volume Of Fluid) multiphase hydrodynamic theory to model the active-passive mixture [138, 139]. The two fluids are described by three continuum fields: the volume fraction of the active phase $\phi$ which is referred to as the 'color function' in VOF, the velocity field $\mathbf{v}$, and the nematic tensor $\mathbf{Q} \equiv S(\hat{\mathbf{n}}\hat{\mathbf{n}} - \mathbf{I})$ describing the local orientation of microtubule bundles. Here, $\hat{\mathbf{n}}$ is a unit vector indicating the local orientation of microtubules, and $0 \leq S \leq 1$ is the local nematic order parameter. $\mathbf{I}$ is the identity matrix. Since the experimental system is quasi-two-dimensional, we implement the theoretical model in two dimensions. The governing equations are [138, 139, 74, 84, 85]:

$$\frac{D\phi}{Dt} = 0, \tag{B.2a}$$

$$\frac{D\mathbf{Q}}{Dt} = \lambda\phi\mathbf{u} + \mathbf{Q}\cdot\boldsymbol{\omega} - \boldsymbol{\omega}\cdot\mathbf{Q} + \frac{1}{\gamma_Q}\mathbf{H}, \tag{B.2b}$$

$$\frac{D\rho\mathbf{v}}{Dt} = \eta\nabla^2\mathbf{v} - \boldsymbol{\nabla}P + \boldsymbol{\nabla}\cdot(\phi\boldsymbol{\sigma}) - \gamma_v\mathbf{v} + \mathbf{f}_c + \mathbf{f}_g, \tag{B.2c}$$

with $D/Dt = \partial_t + \mathbf{v}\cdot\boldsymbol{\nabla}$ the material derivative.

The field $\phi$ is set by the initial conditions to have constant value in the bulk of either phase, with $\phi = 1$ in the active fluid and $\phi = 0$ in the passive one, and sharp yet continuous variations between the two bulk values at the interface. The advection of $\phi$ by the flow then drives interface fluctuations. Unlike the more familiar phase field model, the VOF model sets the right-hand-side of Eq. (B.2a) equal to zero, hence neglects phase field diffusion in the interfacial region. It is appropriate when phenomena such as Ostwald ripening are much slower than other time scales, as appears to be the case in the

active-LLPS. It is much more efficient for simulating large interfaces as it only requires interfacial widths of the order of 2-3 grid points.

The dynamics of the nematic tensor $\mathbf{Q}$ is governed by relaxation and coupling to flow. The first term on the right hand side of Eq. (B.2b) describes alignment with local flow gradients, with $\mathbf{u} = (\boldsymbol{\nabla}\mathbf{v} + \boldsymbol{\nabla}\mathbf{v}^T)/2$ and $\lambda$ the flow-alignment parameter. The flow alignment term is known to drive nematic order even when the system is in the isotropic state [140, 141]. To confine this effect to the active phase, we weight the flow-alignment term by the color function $\phi$ such that flow alignment vanishes in the passive phase. The second and third term describe co-rotation of the director with the local vorticity $\boldsymbol{\omega} = (\boldsymbol{\nabla}\mathbf{v} - \boldsymbol{\nabla}\mathbf{v}^T)/2$, and we neglect for simplicity other nonlinear flow couplings. The relaxation of $\mathbf{Q}$, with $\gamma_Q$ the rotational viscosity, is driven by the molecular field $\mathbf{H} = -\delta F_{LdG}/\delta\mathbf{Q}$ that minimizes the Landau-de Gennes free energy [142, 74]

$$F_{LdG} = \frac{1}{2}\int_{\mathbf{r}} \left[ a\mathrm{Tr}\mathbf{Q}^2 + \frac{b}{2}\left(\mathrm{Tr}\mathbf{Q}^2\right)^2 + K(\partial_j Q_{ik})^2 \right] \tag{B.3}$$

The first two terms in $F_{LdG}$ control the isotropic-nematic transition, and sets the equilibrium value of order parameter to be $S = 0$ when $a > 0$ and $S = \sqrt{-2a/b}$ if $a < 0$. The last term describes the energy cost for spatial variation of the order parameter, with isotropic stiffness $K$. Here we choose $a > 0$. This places the liquid crystal in the isotropic state when passive, which is the experimentally relevant situation.

The velocity field is governed by the Navier-Stokes equation Eq. (B.2c), with viscous dissipation controlled by viscosity $\eta$, drag $\gamma_v$ with the walls, gravitational force $\mathbf{f}_g = -\rho(\phi)g\hat{\mathbf{y}}$, and a capillary force, $\mathbf{f}_c = \gamma\kappa\boldsymbol{\nabla}\phi$ [138, 139], where $\gamma$ is the interfacial tension and $\kappa = -\boldsymbol{\nabla}\cdot(\boldsymbol{\nabla}\phi/|\boldsymbol{\nabla}\phi|)$ the local curvature of the interface. Integrating such capillary force along the interface normal $\hat{\mathbf{N}} = \boldsymbol{\nabla}\phi/|\boldsymbol{\nabla}\phi|$ gives a total force $\gamma\kappa\hat{\mathbf{N}}$, which is what we expected from Young-Laplace pressure. The pressure $P$ serves as a Lagrange multiplier

to incorporate the incompressibility constraint, $\boldsymbol{\nabla} \cdot \mathbf{v} = 0$. The additional stress from the nematic degrees of freedom, $\boldsymbol{\sigma} = \boldsymbol{\sigma}^e + \boldsymbol{\sigma}^a$ includes passive elastic and active stresses, with

$$\boldsymbol{\sigma}^e = -\lambda \mathbf{H} + \mathbf{Q} \cdot \mathbf{H} - \mathbf{H} \cdot \mathbf{Q} \,, \qquad \boldsymbol{\sigma}^a = \alpha \mathbf{Q} \,, \tag{B.4}$$

and $\alpha < 0$ the activity. Note that $\boldsymbol{\sigma}$ is weighted by the color function $\phi$ in Eq. (B.2c), hence its contribution vanishes in the passive phase. Similarly, the capillary force $\mathbf{f}_c$ is nonzero only at the interface. For simplicity, we assume that the two phases have the same viscosity and drag. Finally, the local density is related to the volume fraction $\phi$ as $\rho = \phi\rho_a + (1-\phi)\rho_p$, where $\rho_a$ and $\rho_p$ are the densities of pure active and passive phase, respectively.

## B.4 Numerical simulations

### B.4.1 General setting.

The continuum equations are solved with the Finite Volume Method using the open source package OpenFOAM [143] (OpenFoam, *https://openfoam.org/*). Specifically, we modify the InterFoam solver from OpenFOAM to include the dynamics of the nematic tensor $\mathbf{Q}$ [144] (InterFoam, *https://openfoamwiki.net/index.php/InterFoam*). The simulation is done on a square grid embedded in a rectangular box centered at the origin, and we use the standard adaptive time step controller in OpenFOAM with a maximum Courant number 0.3. Although OpenFOAM can only process three-dimensional simulations, one can still use it to simulate two-dimensional systems by having a single grid along the third dimension, and setting the two boundaries normal to the third dimension to be *empty* (Openfoam user guide, *https://cfd.direct/openfoam/user-guide/*).

The parameters used in the simulations are: $\rho_a = 1027kg/m^3$, $\rho_p = 1014kg/m^3$, $\eta = 0.015Pa{\cdot}S$, $\gamma_v = 25MPa{\cdot}S/m^2$, $\gamma = 0.3\mu N/m$, $\gamma_Q = 0.1kg/(m{\cdot}S)$, $K = 5{\times}10^{-14}N$, $a = 0.001Pa$, $b = 0.1Pa$, $\lambda = 0.1$. Activity values range from 5 mPa to 80 mPa. The boundary and initial conditions, box and grid sizes are varied depending on the specific problem we study.

### B.4.2 Simulations of interfacial fluctuations.

We use a rectangular box of size $2mm \times 1mm$ in the $xy$ plane, with a uniform grid spacing of $2.5\mu m$. In the absence of active fluctuations, the interface separating the top passive fluid from the bottom active fluid is flat and located at $y = 0$. The top and bottom boundaries are solid walls with slip boundaries for the velocity field $\mathbf{v}$, i.e., $\hat{\mathbf{n}} \cdot \mathbf{v} = 0$ and $\partial_{\hat{\mathbf{t}}} v_{\hat{\mathbf{t}}} = 0$ where $\hat{\mathbf{n}}$ and $\hat{\mathbf{t}}$ represent the normal and tangential directions to the wall, and Neumann boundary for the color function $\phi$ and the nematic tensor $\mathbf{Q}$, i.e., $\nabla\phi|_{wall} = 0$ and $\nabla Q_{ij}|_{wall} = 0$. Although no-slip condition is typically used at solid walls, our experiments have found obvious sliding of microtubules with respect to the wall, hence justifying the slip boundary condition of velocity at the wall. At the left and right boundaries we impose periodic boundary conditions by using the *cyclicAMI* boundary in OpenFoam. All simulations start with a flat interface located at 65% of the box height, with zero velocity and zero nematic order. We add small perturbations to the initial $\mathbf{Q}$ field in the active phase. Activity then drives these initial perturbations to grow and pushes the system into the chaotic state.

### B.4.3 Simulations of wetting.

For the wetting simulations, we use a smaller simulation box of size $0.5mm \times 0.5mm$ since we need to use finer grids here. The boundary conditions at the top and bottom boundaries are the same as used in the simulations of interfacial fluctuations. The left and right boundaries are treated as solid walls, with slip boundary conditions for the velocity field and zero-gradient boundary conditions for the color function ($\nabla\phi|_{wall} = 0$), except at the interface contact point, where the gradient of $\phi$ is set to prescribe the contact angle of the passive system using the *constantAlphaContactAngle* function in OpenFoam. The nematic tensor $\mathbf{Q}$ has a fixed value at the left and right walls. For parallel anchoring of nematic director, we set $Q_{xx} = -0.5$ and $Q_{xy} = 0$ at the two walls, and $Q_{xx} = 0.5$ and $Q_{xy} = 0$ for perpendicular wall anchoring. We use nonuniform grids in the wetting simulations. The grid size in the bulk ($|x| < 0.23mm$) is set to be $2.5\mu m$ as in the fluctuation simulations. To improve the spatial resolution at the contact point, we refine the simulation grid close to the wall such that the grid size is $1.25\mu m$ for grids within $0.23mm < |x| < 0.24mm$ and $0.625\mu m$ for grids at $|x| > 0.24mm$. The initial condition is similar to that in the fluctuation simulations, except the flat interface is located at 50% of the box height.

### B.4.4 Extracting interface profiles.

The instantaneous interface profile $h(x,t)$ is extracted from the spatial distribution of color function $\phi$ by using the *isoSurface* function in OpenFOAM. Specifically, OpenFOAM first interpolates among discrete $\phi$ values residing on grids to get a continuously varying $\phi$ field. Based on this, it is able to find numerically the positions where the continuous $\phi$ field is exactly 0.5. The coordinates of the points with $\phi = 0.5$ then constitute

the interface profiles we are looking for.

## B.5 Theory of active interfacial fluctuations

As discussed in the main text, the non-monotonic power spectra of interfacial tangent angle fluctuations is the result of a competition between passive relaxations and active excitations [Fig. 3.5B, 3.7B]. Here, we provide the theoretical basis for this claim by analytically deriving the height equation for fluctuating interfaces from continuum hydrodynamics and, based on that, calculate the fluctuation spectrum of passive and active interface.

We begin by recalling the behavior of thermally driven interfaces.

## B.6 Equilibrium interfacial fluctuations from the equipartition theorem.

For a system in thermal equilibrium the equal-time spectrum of fluctuations is easily obtained from the energy cost of distortions of the flat interface located at $y = 0$. We expand the distortion $h(x,t)$ in a Fourier series as $h(x,t) = \frac{1}{L}\sum_k \hat{h}(k,t)\ e^{ikx}$, with $L$ the system size along $x$ and inverse transform $\hat{h}(k,t) = \int_{-L/2}^{L/2} dx\ h(x,t)\ e^{-ikx}$. Assuming small deformations, the energy cost of interface fluctuations is

$$\mathcal{F} = \frac{1}{2L}\sum_k (\gamma k^2 + \Delta\rho g)|\hat{h}(k,t)|^2\ , \tag{B.5}$$

where we have included the energy cost due to gravity. Here $\gamma$ is the interfacial tension and $\Delta\rho$ is the difference between the densities of the bottom and top fluid. The

equipartition theorem states that the mean energy of each fluctuation mode is $k_BT/2$. It immediately follows

$$\frac{1}{L}\langle|\hat{h}(k,t)|^2\rangle = \frac{k_BT}{\gamma(k^2+\ell_c^{-2})} \ . \tag{B.6}$$

As is well known, the spectrum becomes constant in the gravity-dominated region $k \ll \ell_c^{-1}$, and scales as $k^{-2}$ at $k \gg \ell_c^{-1}$ where interfacial tension dominates [145].

### B.6.1 Equilibrium interfacial fluctuations from interface dynamics.

Active systems cannot be described by a free energy and require an approach based on dynamics. To set the stage for the study of active interfacial fluctuations, it is useful to first derive the thermal fluctuation spectrum from hydrodynamics for the case where fluid dissipation is controlled by *both* friction with a substrate and fluid viscosity, as relevant to our experimental system. This derivation, which is not available in the literature, will inform the calculation of the active fluctuation spectrum.

We consider two passive fluids. For simplicity assume they have the same viscosity and friction, and only differ in density. We consider the dynamics in the Stokes limit which is appropriate for our experiments and follow the derivation of Refs. [146, 147, 148, 149, 150]. The Stokes equation for the two semi-infinite fluids in the presence of thermal noise is given by

$$\gamma_v\mathbf{v} = \eta\nabla^2\mathbf{v} - \nabla P - \rho g\hat{\mathbf{y}} + \mathbf{f}(\mathbf{r},t) \ , \tag{B.7}$$

where

$$\mathbf{f}(\mathbf{r},t) = \nabla\cdot\boldsymbol{\sigma}(\mathbf{r},t) + \eta(\mathbf{r},t) \tag{B.8}$$

comprises the stochastic stress and force density describing the effect of thermal noise, with correlations determined by the fluctuation-dissipation theorem as

$$\begin{aligned}\langle\sigma_{ik}(\mathbf{r},t)\sigma_{jl}(\mathbf{r}',t')\rangle =&2k_BT\eta(\delta_{ij}\delta_{kl}+\delta_{il}\delta_{jk})\delta(\mathbf{r}-\mathbf{r}')\delta(t-t')\ ,\\ \langle\eta_i(\mathbf{r},t)\eta_j(\mathbf{r}',t')\rangle =&2k_BT\gamma_v\delta_{ij}\delta(\mathbf{r}-\mathbf{r}')\delta(t-t')\ ,\\ \langle\sigma_{ik}(\mathbf{r},t)\eta_j(\mathbf{r}',t')\rangle =&0\ .\end{aligned} \tag{B.9}$$

We assume the fluids to be incompressible, hence $\nabla\cdot\mathbf{v}=0$.

Continuity of velocity and stress at the interface requires

$$\begin{aligned}&[\mathbf{v}]_0=0\ ,\\ &[\eta(\partial_x v_y+\partial_y v_x)+\sigma_{xy}]_0=0\ ,\\ &[2\eta\partial_y v_y-P+\sigma_{yy}]_0=\gamma\partial_x^2 h-\Delta\rho g h\ ,\end{aligned} \tag{B.10}$$

where for any function $s(x,y)$ we have defined $[s(x)]_0\equiv s(x,y=0^-)-s(x,y=0^+)$ as the change in $s$ across the interface. The two terms on the RHS of the last equation represent the Laplace pressure due to interfacial tension and gravity-induced pressure difference, respectively.

To linear order, the interface height is related to the local velocity through

$$\partial_t h(x,t)=v_y(x,y=0,t)\ . \tag{B.11}$$

To obtain an equation for the dynamics of interface fluctuations, we need to solve for $v_y(x,y,t)$ for given stochastic force $\mathbf{f}(\mathbf{r},t)$. Interface height correlations will then be obtained by averaging over thermal noise.

By taking Fourier transforms of Eqs. (B.7)-(B.10) with respect to $x$ and eliminating

$\hat{v}_x$ and $\hat{P}$ in favor of $\hat{v}_y$, we obtain an equation for $\hat{v}_y(k,y,t)$ as

$$(\partial_y^2 - k^2)(\partial_y^2 - \beta^2 k^2)\hat{v}_y(k,y,t) = \frac{ik}{\eta}\left(\partial_y \hat{f}_x - ik\hat{f}_y\right) , \tag{B.12}$$

where $\beta = \sqrt{1 + 1/(\ell_\eta^2 k^2)}$, and $\ell_\eta = \sqrt{\eta/\gamma_v}$ is the viscous screening length. We similarly eliminate $\hat{v}_x$ and $\hat{P}$ from Eqs. (B.10) to express the boundary conditions in terms of $\hat{v}_y$, with the result

$$\begin{aligned}
&[\hat{v}_y]_0 = 0 , \\
&[\partial_y \hat{v}_y]_0 = 0 , \\
&[\eta(\partial_y^2 + k^2)\hat{v}_y - ik\hat{\sigma}_{xy}]_0 = 0 , \\
&\left[\frac{\eta}{k^2}(\partial_y^2 - 3k^2 - \ell_\eta^{-2})\partial_y \hat{v}_y - \hat{\sigma}_{yy} - \frac{i}{k}\hat{f}_x\right]_0 = \gamma(k^2 + \ell_c^{-2})\hat{h} .
\end{aligned} \tag{B.13}$$

We write the solution to Eq. (B.12) with boundary conditions given by Eq. (B.13) as the sum of the solution to the homogeneous equation with the required boundary conditions and a particular solution to the inhomogeneous equation with homogeneous boundary conditions,

$$\hat{v}_y(k,y,t) = \hat{v}_y^h(k,y,t) + \hat{v}_y'(k,y,t) . \tag{B.14}$$

The homogeneous solution $\hat{v}_y^h$ describes the flow induced by the stress discontinuity across the interface and propagated by passive processes. It is given by

$$\begin{aligned}
\hat{v}_y^h(k,y,t) = &-\frac{|k|}{2\gamma_v}\left[\gamma(k^2 + \ell_c^{-2})\hat{h} + [\hat{\sigma}_{yy} + \frac{i}{k}\hat{f}_x]_0\right]\left(e^{-|ky|} - \frac{1}{\beta}e^{-\beta|ky|}\right) \\
&+ \frac{ik\hat{\sigma}_{xy}}{2\gamma_v}\mathrm{sign}(y)\left(e^{-|ky|} - e^{-\beta|ky|}\right) .
\end{aligned}$$

The particular solution can be obtained in terms of Green's function and describes interfacial flows driven by stochastic stress and force in the bulk. It is given by

$$\begin{aligned}\hat{v}'_y(k,y,t) =& \frac{|k|}{2\gamma_v}\int_{-\infty}^{0-} dy' \left(e^{-|k||y-y'|} - \frac{1}{\beta}e^{-\beta|k||y-y'|}\right)\left[\hat{f}_y(k,y',t) + \frac{i}{k}\partial_{y'}\hat{f}_x(k,y',t)\right] \\ &+ \frac{|k|}{2\gamma_v}\int_{0+}^{\infty} dy' \left(e^{-|k||y-y'|} - \frac{1}{\beta}e^{-\beta|k||y-y'|}\right)\left[\hat{f}_y(k,y',t) + \frac{i}{k}\partial_{y'}\hat{f}_x(k,y',t)\right].\end{aligned} \tag{B.15}$$

Adding the two solutions $\hat{v}_y^h$ and $\hat{v}'_y$, and integrating by parts, it is easy to show that, at the interface $y = 0$, the surface terms in $\hat{v}'_y$ are cancelled by equal and opposite contributions from $\hat{v}_y^h$. The $y$ velocity at the interface can then be written as

$$\hat{v}_y(k, y = 0, t) = \hat{v}^r(k,t) + \hat{v}^t(k,t)\ , \tag{B.16}$$

where $\hat{v}^r$ controls the passive relaxation of the interface due to surface tension and gravity and $\hat{v}^t$ represents the stochastic forcing arising from thermal noise that drives interface fluctuations. The relaxation part has the form

$$\hat{v}^r(k,t) = -\nu(k)\hat{h}(k,t)\ , \tag{B.17}$$

with

$$\nu(k) = \frac{\gamma(k^2 + \ell_c^{-2})}{2\eta|k|(\beta^2+\beta)} \equiv \frac{\gamma(k^2+\ell_c^{-2})}{\zeta(k)}\ , \tag{B.18}$$

where

$$\zeta(k) = 2\eta|k|(\beta^2+\beta) \tag{B.19}$$

has a natural interpretation as an effective friction per unit length on the interface. The

stochastic forcing has a rather lengthy expression

$$\begin{aligned}\hat{v}^t(k,t) =& \frac{k^2}{2\gamma_v}\int_{-\infty}^{0} dy' e^{|k|y'}\left[\hat{\sigma}_{xx}(y') - \hat{\sigma}_{yy}(y') + 2ik|k|^{-1}\hat{\sigma}_{xy}(y') - ik^{-1}\hat{f}_x(y') + |k|^{-1}\hat{f}_y(y')\right] \\ & - \frac{k^2}{2\gamma_v}\int_{-\infty}^{0} dy' e^{\beta|k|y'}\Big[\hat{\sigma}_{xx}(y') - \hat{\sigma}_{yy}(y') + ik|k|^{-1}(\beta+\beta^{-1})\hat{\sigma}_{xy}(y') - ik^{-1}\hat{f}_x(y') \\ & + \beta^{-1}|k|^{-1}\hat{f}_y(y')\Big] \\ & - \frac{k^2}{2\gamma_v}\int_{0}^{\infty} dy' e^{-|k|y'}\left[\hat{\sigma}_{xx}(y') - \hat{\sigma}_{yy}(y') - 2ik|k|^{-1}\hat{\sigma}_{xy}(y') - ik^{-1}\hat{f}_x(y') - |k|^{-1}\hat{f}_y(y')\right] \\ & + \frac{k^2}{2\gamma_v}\int_{0}^{\infty} dy' e^{-\beta|k|y'}\Big[\hat{\sigma}_{xx}(y') - \hat{\sigma}_{yy}(y') - ik|k|^{-1}(\beta+\beta^{-1})\hat{\sigma}_{xy}(y') - ik^{-1}\hat{f}_x(y') \\ & - \beta^{-1}|k|^{-1}\hat{f}_y(y')\Big] ,\end{aligned} \tag{B.20}$$

but it is easy to show using Eqs. (B.9) that it has zero mean and correlations

$$\langle \hat{v}^t(k,t)\hat{v}^t(k',t')\rangle = \frac{2k_BT}{\zeta(k)} L\delta_{k,-k'}\ \delta(t-t') . \tag{B.21}$$

The dynamics of interface fluctuations is then governed by a Langevin equation

$$\partial_t \hat{h}(k,t) = -\nu(k)\hat{h}(k,t) + \hat{v}^t(k,t) . \tag{B.22}$$

with noise correlations given by Eq. (B.21). We can now use the Langevin equation to evaluate the equal time spectrum of interface fluctuations. After defining the temporal Fourier transform, $\hat{h}(k,\omega) = \int_{-\infty}^{\infty} dt e^{-i\omega t}\hat{h}(k,t)$, we immediately obtain the dynamic structure factor of the interface as

$$\frac{1}{L}\langle|\hat{h}(k,\omega)|^2\rangle = \frac{2k_BT/\zeta(k)}{\omega^2+\nu^2(k)} . \tag{B.23}$$

The static or equal-time fluctuation spectrum is then given by

$$\frac{1}{L}\langle|\hat{h}(k,t)|^2\rangle = \int_{-\infty}^{\infty}\frac{d\omega}{2\pi L}\langle|\hat{h}(k,\omega)|^2\rangle = \frac{2k_BT/\zeta(k)}{2\nu(k)} = \frac{k_BT}{\gamma(k^2+\ell_c^{-2})}\ , \tag{B.24}$$

which is consistent with that obtained using the equipartition theorem. Importantly, the dependence of the noise amplitude on the effective friction is key for guaranteeing the result obtained from equipartition.

### B.6.2 Dynamics of activity-powered interfacial fluctuations.

In the previous section, we studied the dynamics of thermally driven interfaces. This is characterized by the exponential relaxations with $k$ dependent rates that are controlled by interfacial tension and gravity. Now we will show how a non-monotonic tangent angle spectrum arises in active interfaces from the competition of the passive relaxation mechanisms delineated above and active processes. When the bottom fluid is active, the main driving force of interfacial fluctuations is not thermal noise, but active stress. Neglecting random thermal forces and stresses, the Stokes equation then takes the form

$$\gamma_v\mathbf{v} = \eta\nabla^2\mathbf{v} - \nabla P - \rho g\hat{\mathbf{y}} + \nabla\cdot\sigma^{\mathbf{a}}\ , \tag{B.25}$$

where the active stress $\sigma^{\mathbf{a}}$ is specified below.

One can then carry out the same derivation as in the thermal case to obtain an equation for the interfacial fluctuations as

$$\partial_t\hat{h}(k,t) = -\nu(k)\hat{h}(k,t) + \hat{v}^a(k,t)\ , \tag{B.26}$$

where the passive relaxation rate $\nu(k)$ is given again by Eq. (B.18) and $\hat{v}^a(k,t)$ is the

active forcing (or active interfacial flow) due to bulk active stress, given by

$$\begin{aligned}\hat{v}^a(k,t) =& \frac{k^2}{2\gamma_v}\int_{-\infty}^{0} dy\; e^{|k|y}\left[2\hat{\sigma}^a_{xx}(y) + 2ik|k|^{-1}\hat{\sigma}^a_{xy}(y)\right] \\ &- \frac{k^2}{2\gamma_v}\int_{-\infty}^{0} dy\; e^{\beta|k|y}\left[2\hat{\sigma}^a_{xx}(y) + ik|k|^{-1}(\beta+\beta^{-1})\hat{\sigma}^a_{xy}(y)\right].\end{aligned} \tag{B.27}$$

In this case, however, Eq. (B.26) is not a closed equation since the forcing $\hat{v}^a$ is determined by the dynamics of the active stress, which in turn couples back to the flow, as shown in Eq. (B.2b). As discussed in the main text, this feedback is key for the onset of traveling surface waves. On the other hand, as shown below, the form given in Eq. (B.26) offers a useful interpretation of the role of activity on the equal-time fluctuation spectrum.

To proceed, we treat the active stress as stochastic forcing correlated both in space and time. This is justified by a large body of simulations of bulk active nematics [151] that have quanified active stress correlations. For the purpose of modeling interfacial fluctuations, we assume a simple form with exponential correlation in both space and time, given by

$$\langle\sigma^a_{xx}(\mathbf{r},t)\sigma^a_{xx}(\mathbf{r}',t')\rangle = \langle\sigma^a_{xy}(\mathbf{r},t)\sigma^a_{xy}(\mathbf{r}',t')\rangle = \sigma^2_{rms}e^{-|\mathbf{r}-\mathbf{r}'|/\ell_a}e^{-|t-t'|/\tau_a}\,, \tag{B.28}$$

and $\langle\sigma^a_{xx}(\mathbf{r},t)\sigma^a_{xy}(\mathbf{r}',t')\rangle = 0$. The statistical properties of the active noise are then completely determined by three quantities: the correlation length $\ell_a$, the correlation time $\tau_a$, and root mean square active stress $\sigma_{rms}$.

Using Eqs. (B.27)-(B.28), we can calculate the correlation function of the active forcing $v^a$ as

$$\langle\hat{v}^a(k,t)\hat{v}^a(k',t')\rangle = \frac{2\mathcal{E}(k)}{\zeta(k)}L\delta_{k,-k'}\;\frac{e^{-|t-t'|/\tau_a}}{\tau_a}\,, \tag{B.29}$$

where

$$\mathcal{E}(k) = \frac{\sigma_{rms}^2 \ell_a^2 \tau_a \zeta(k)}{8\gamma_v^2} \int_{-\infty}^{\infty} dk_z \frac{(\beta-1)^2 k^6}{(k^2+k_z^2)\left(\beta^2 k^2 + k_z^2\right)} \frac{4 + \left(1+\beta^{-1}\right)^2 + \left(1-\beta^{-1}\right)^2 k_z^2 k^{-2}}{\left(1+\ell_a^2 k^2 + \ell_a^2 k_z^2\right)^{3/2}}. \tag{B.30}$$

We can then readily obtain the equal-time spectrum of the active interfacial fluctuations as

$$\frac{1}{L}\langle|\hat{h}(k,t)|^2\rangle = \frac{2\mathcal{E}(k)}{\gamma(k^2+\ell_c^{-2})} \frac{1}{1+\tau_a\nu}. \tag{B.31}$$

The equal-time spectrum of the active interface is well described by Eq. (B.31). Figures B.10A,B show excellent agreement between the theoretical spectra (solid lines) calculated using Eq. (B.31) and those measured from simulations and experiment (circles). The experiment, simulations, and theory, all suggest a crossover of the height spectrum from $\langle|\hat{h}(k,t)|^2\rangle \sim |k|$ at small wavenumber to $\langle|\hat{h}(k,t)|^2\rangle \sim k^{-6}$ at large wavenumber, which is very different from the equilibrium spectrum in Eq. (B.24). This can be attributed to the scale dependence of energy injection in the active fluid.

To understand this, note that $\mathcal{E}(k)$ has the dimension of energy. Comparing Eq. (B.29) to (B.21), we see that $\mathcal{E}(k)$ can be used to characterize the energy scale of active fluctuations, to be compared to $k_BT$ in thermal equilibrium. We have calculated $\mathcal{E}(k)$ numerically using Eq. (B.30) and the results are shown in Figs. B.10C,D. Both simulations and experiments show energy scale of the order $10^{-13} \sim 10^{-11} J$, which is much larger than the thermal energy scale $k_BT \sim 10^{-21} J$. This explains the giant interfacial fluctuations found in both experiments and simulations. Furthermore, $\mathcal{E}(k)$ has a strong dependence on wavenumber $k$: it crosses over from $\mathcal{E}(k) \sim k$ at small $k$ where dissipation is dominated by friction to $\mathcal{E}(k) \sim k^{-3}$ where dissipation is dominated by viscosity. The crossover length scale is essentially independent of activity and is controlled by the typical size of flow vortices, which in our system is determined by the screening length

$\ell_\eta$. This behavior is consistent with the energy spectrum reported for bulk active liquid crystal in the regime of active turbulence [89].

The scale dependence of the active energy injection determines the fluctuation spectrum of active interface. At small wavenumber or large scales,

we find $\langle|\hat{h}(k,t)|^2\rangle \sim \mathcal{E}(k) \sim k$, in agreement with the interfacial spectra shown in Figs. B.10A,B from both simulations and experiments. At large wavenumber where $\tau_a\nu(k) \gg 1$, we find $\langle|\hat{h}(k,t)|^2\rangle \sim \mathcal{E}(k)/(k^2\nu(k)) \sim k^{-6}$, where we have assumed $k \gg \ell_c^{-1}, \ell_\eta^{-1}$ and used $\nu(k) \sim k$. The scale-dependence of active energy injection distinguishes the active interfacial spectra from their equilibrium counterparts.

### B.6.3 Estimating active stress using interfacial fluctuations.

Equation (B.31) allows us to estimate the magnitude of the active stress $\sigma_{rms}$ from the interface spectrum. This is best done using the interface's tilting angle $\theta$ instead of the height since the former is well defined even at high activity. Using $\hat{\theta}(k,t) \simeq ik\hat{h}(k,t)$, we find

$$\frac{1}{L}\langle|\hat{\theta}(k,t)|^2\rangle = \frac{2k^2\mathcal{E}(k)}{\gamma(k^2+\ell_c^{-2})}\frac{1}{1+\tau_a\nu}, \tag{B.32}$$

and the root mean square value of $\theta$

$$\theta_{rms} \equiv L^{-1}\sqrt{\sum_k \langle|\hat{\theta}(k,t)|^2\rangle}. \tag{B.33}$$

Clearly $\theta_{rms}$ is proportional to the amplitude of the active stress $\sigma_{rms}$,

$$\theta_{rms} = \sigma_{rms}/p, \tag{B.34}$$

where

$$\frac{1}{p^2} = \sum_k \frac{\ell_a^2 \tau_a L^{-1} k^2}{4\gamma_v^2 \nu (1+\tau_a \nu)} \int_{-\infty}^{\infty} dk_z \frac{(\beta-1)^2 k^6}{(k^2+k_z^2)\left(\beta^2 k^2 + k_z^2\right)} \frac{4 + \left(1+\beta^{-1}\right)^2 + \left(1-\beta^{-1}\right)^2 k_z^2 k^{-2}}{\left(1+\ell_a^2 k^2 + \ell_a^2 k_z^2\right)^{3/2}}. \tag{B.35}$$

Measuring $\theta_{rms}$ and calculating $p$ numerically allows us to estimate the magnitude of active stress $\sigma_{rms}$.

We use this method to measure the active stress in the experiment. Taking advantage of the fact that $\ell_a$ and $\tau_a$ barely change with the KSA concentration, $p$ is essentially independent of the KSA concentration. Using $p \approx 8.4$ mPa/rad estimated from one set of data, we obtain that the active stress varies between 2.5 mPa and 6 mPa in the experiment [Fig. 3.10B], close to the values obtained from activity-induced wetting below 300 nM KSA. The lowest active stress value coincides with the yield stress of passive kinesin-crosslinked bundled microtubule gels [152].

## B.7 Theory of activity-induced wetting: from active stress to active tension

The enhanced wetting in the presence of activity originates from directed active stresses in the region near the wall that persistently lift the interface, effectively increasing wall adhesion of the active phase. Both experiment and simulation show that nematic director preferentially aligns with the wall [Fig. 3.8B, 3.9A inset]. Such an alignment is expected even for passive rigid filaments due to steric interaction with the wall [142, 153]. It is enhanced by active forces, resulting in so-called active anchoring, as demonstrated in recent simulations [85, 154, 155]. Since the active stress is extensile, these vertically aligned domains exert, on average, a lifting force on the interface, driving

it upwards. Activity then changes both the height of the contact point and the apparent wetting angle, as shown below.

### B.7.1 Force balance at a passive interface.

We first summarize the force balance that determines the interface profile and the wetting angle of a passive interface in the presence of gravity [156]. For a passive interface, the profile of the interface height $h(x,t)$ is governed by the Young-Laplace equation that expresses normal force balance across the interface as

$$\gamma \frac{h''}{(1+h'^2)^{3/2}} - \Delta\rho g h = 0 \ , \tag{B.36}$$

where primes denote derivatives with respect to $x$ and $\gamma$ is the interfacial tension. This equation needs to be solved with the contact boundary condition at the wall

$$h'(0) = -\cot\theta_e \ , \tag{B.37}$$

where the wetting angle $\theta_e$ (shown in Fig. B.7.3A) is determined by balancing the wall tension $\gamma_w$ and the interfacial tension $\gamma$

$$\gamma \cos\theta_e = \gamma_w \ . \tag{B.38}$$

Assuming the slope of the interface remains small, i.e., $h' \ll 1$, Eq. (B.36) can be linearized and solved, resulting in an exponential interface profile, given by

$$h(x) = \ell_c \cot\theta_e \ e^{-x/\ell_c} \ , \tag{B.39}$$

with $\ell_c = \sqrt{\gamma/\Delta\rho g}$ the capillary length.

### B.7.2 Force balance at an active interface.

In the active liquid crystal there is a region close to the wall where MT bundles align parallel to the wall [Figs. 3.8B, 3.9A inset, B.7.3B]. We assume that the thickness $\ell_w$ of this wall-aligned region is $\ell_w \ll \ell_c$. Outside this region ($x > \ell_w$), the average active stress vanishes due to the chaotic dynamics, and we expect the average interface profile to be governed again by the Young-Laplace equation, but with an apparent wetting angle $\theta_a$ different from the equilibrium wetting angle $\theta_e$ [Fig. B.7.3B]. The profile is therefore given by Eq. (B.39), with $\theta_e \to \theta_a$.

To determine $\theta_a$, we examine force balance within the thin wall-aligned region where four forces per unit chamber thickness are at play (inset Fig. B.7.3B):

1. coherent active stresses lifting the interface $F_a \approx -\alpha\ell_w$, where $\alpha < 0$;
2. vertical downward gravitaional force resulting from density difference, $F_g = \Delta\rho g h_0 \ell_w$, where $h_0$ is the height of the contact point;
3. interfacial tension away from the wall aligned domain at $x > \ell_w$, drags the interface downward $F_i = \gamma \cos\theta_a$ in the $y$ direction;
4. wall adhesion contributes to a vertical lifting force per unit length $F_w = \gamma_w$.

The wetting angle $\theta_a$ is determined by the balance of these four terms through

$$F_w + F_a = F_i + F_g \,, \tag{B.40}$$

$-\alpha\ell_w > 0$ has the dimension of interfacial tension which defines an "active tension" $\gamma_a \equiv |\alpha|\ell_w$.

Prior to complete wetting, the interface profile for $x \geq \ell_w$ is governed by the Young-Laplace law with wetting angle $\theta_a$. The interface profile must be obtained from the solution of the nonlinear equation, Eq. (B.36) [156]. The maximum height $h_0$ is obtained by setting $h(x=0) \simeq h(x=\ell_w)$, with the result

$$h_0 \approx \ell_c\sqrt{2(1-\sin\theta_a)}. \tag{B.41}$$

Equation (B.40) then becomes

$$\gamma\cos\theta_a + \Delta\rho g\ell_w\ell_c\sqrt{2(1-\sin\theta_a)} = \gamma_w + |\alpha|\ell_w\ . \tag{B.42}$$

This shows that increase in activity results in a decrease of the active wetting angle $\theta_a$, and associated increase of the maximum height $h_0$.

The onset of complete wetting corresponds to $\theta_a = 0$. Inserting this in Eq. (B.42) gives the critical activity for complete wetting as

$$\alpha_c = \frac{\gamma-\gamma_w}{\ell_w} + \sqrt{2}\Delta\rho g\ell_c\ . \tag{B.43}$$

Beyond complete wetting,

$\theta_a = 0$. For $x \leq \ell_w$, the interface height keeps growing until the active stress is balanced by gravity and interfacial tension. Setting $\theta_a = 0$ in Eq. (B.40), we obtain the maximum height as

$$h_0 = \frac{1}{\Delta\rho g\ell_w}\left(\gamma_w-\gamma-\alpha\ell_w\right) = \sqrt{2}\ell_c + \frac{1}{\Delta\rho g}\left(|\alpha|-\alpha_c\right)\ . \tag{B.44}$$

When $|\alpha| \gg \alpha_c$, i.e., at values of activity well above the onset of complete wetting, $h_0 \simeq \frac{|\alpha|}{\Delta\rho g}$ and one can infer the active stress directly by measuring $h_0$. In experiments, we use the center-of-mass of the capillary rise to determine the active stress, as it is challenging to consistently define $h_0$, e.g. when the wetting layer splits from the bulk fluid.

Numerical simulations allowed us to examine the dynamics of active wetting starting from a flat interface. For all activities, the contact point climbed up the wall, saturating at a maximum value determined by force balance [Fig. B.12A]. We compare the steady state maximum height obtained from simulations (circles) to Eq (B.40) [Fig. B.12B]. The theory provides an excellent prediction for the height prior to complete wetting, as well as the transition to complete wetting. Beyond complete wetting, the maximum height $h_0$ increases linearly with activity $|\alpha|$, suggesting that measuring the height of the contact point estimates active stresss. The rate of growth of the height with activity is, however, slightly larger than the expected value $1/\Delta\rho g$ (dashed line in Fig. B.12B). This could be due to the fact that at high activity, the contact point has a sharp geometry and the fields are varying violently in space, which significantly reduces the numerical accuracy of OpenFOAM.

To summarize, the presence of a wall-aligned layer gives rise to an active tension $\gamma_a = |\alpha|\ell_w$ that changes the apparent wetting angle from the passive value $\theta_e$ to $\theta_a$ given by Eq. (B.42). Importantly, we show that it is possible to infer the active stress by comparing measurement of wetting of interfaces in passive and active samples.

### B.7.3 Converting maximum height to center of mass.

In experiments it is difficult to determine the maximum height of the wetting layer. A more convenient and directly measurable quantity for quantifying activity-induced wetting is the center of mass of the region of the interface that is lifted above its flat value, defined as

$$h_c = \frac{1}{2A}\int_0^\infty h^2(x)dx \ , \tag{B.45}$$

where

$$A = \int_0^\infty h(x)dx \tag{B.46}$$

is the area of the lifted region. To compare with experiments we therefore evaluate the center of mass $h_c$ as follows. By requiring that the total gravitational force exerted on the lifted region, $\Delta\rho g A d$, balance the sum of wall adhesion $F_w$ and active lifting force $F_a$, we obtain the area $A$ as

$$A = \frac{\gamma_w - \alpha\ell_w}{\Delta\rho g} \ . \tag{B.47}$$

To evaluate the integral in Eq. (B.45). We separate the wall-aligned layer from the bulk part of the interface. Within the aligning layer $x < \ell_w$, we assume $h(x) \simeq h_0$, so that the thin layer contributes $h_0^2\ell_w/2$ to the integral. For $x \geq \ell_w$, we assume the average interface profile satisfies the nonlinear Young-Laplace equation.Since no explicit solution is available, we first evaluate the interface profile numerically by solving the Young-Laplace equation with contact angle $\theta_a$, then calculate the bulk part of the integral in Eq. (B.45) numerically.

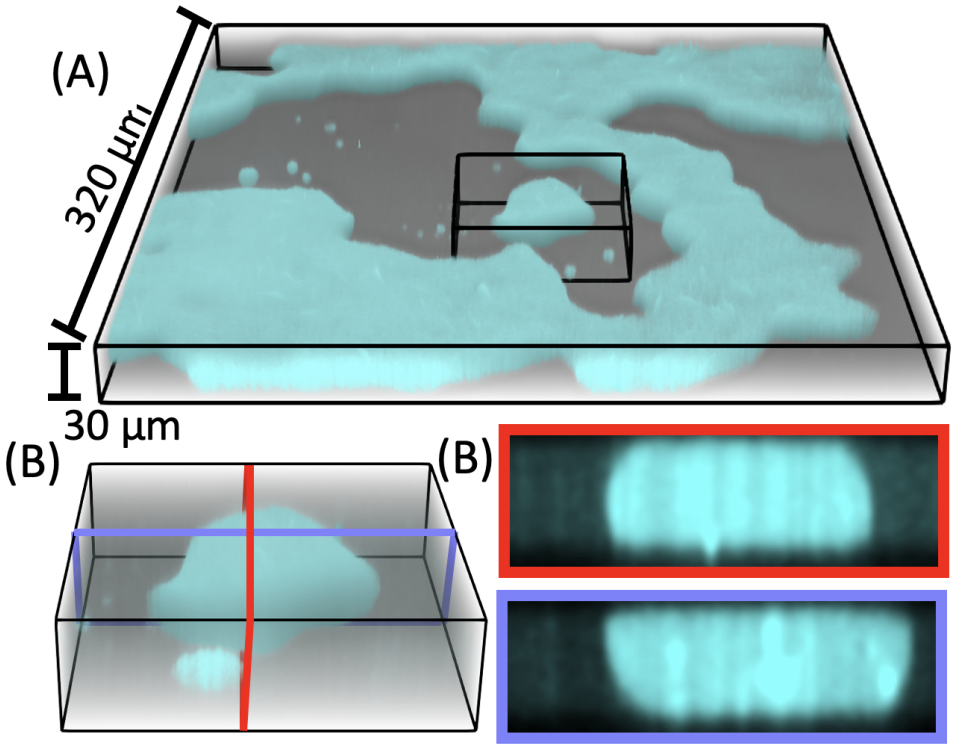


Figure B.1: **Three-dimensional visualization of coarsening sample at 275 nM KSA.** (**A**) Active droplets (cyan) confined to a 30 $\mu$m chamber. (**B**) Magnified image of an isolated droplet. (**C**) Cross sections views of the droplet. In 30 $\mu$m thick chambers, droplets span the entire chamber, and have a nearly flat vertical profile.

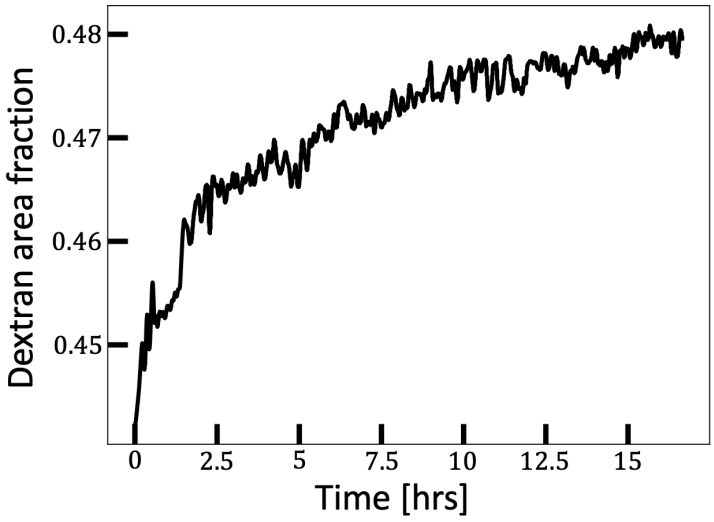


Figure B.2: **Area fraction of dextran over time.** The area fraction initially increases rapidly, then remains nearly constant 2 hours after sample preparation.

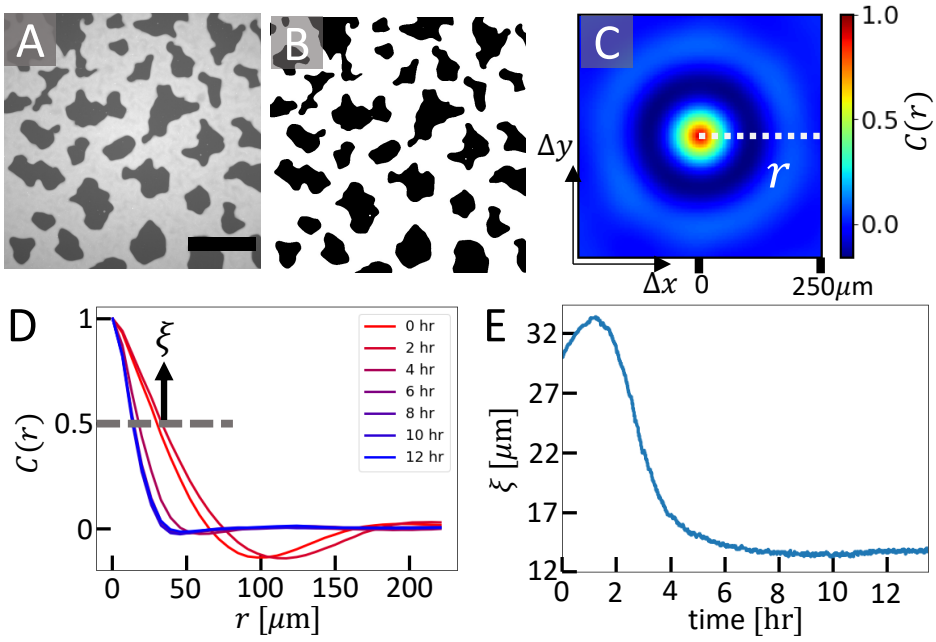


Figure B.3: **Measurement of the correlation length.** (**A**) Dextran fluorescence image 1.5 hr after the start of the experiment. Only part of the field of view is shown. Scale bar 300 $\mu$m. (**B**) Pixels in dextran-rich regions are assigned a value of 1, and those in the PEG-rich regions are assigned a value of $-1$. (**C**) The autocorrelation matrix of (B). (**D**) The radial autocorrelation at 6 time points, obtained from (C) by azimuthal averaging around the origin. The correlation length $\xi$ is defined as the distance at which the autocorrelation function equals 0.5. (**E**) Evolution of $\xi$ in time. KSA concentration 235nM.

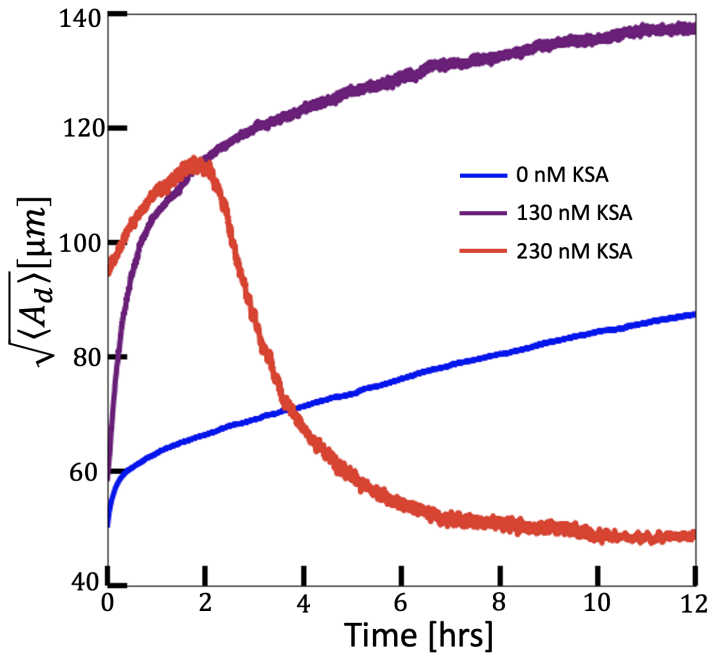


Figure B.4: **Time evolution of average PEG-rich droplet size.** At each time point, all PEG droplets in a dextran-fluorescence image were identified. Then, their areas were averaged and the average droplet size was defined as the square root of the average area. At 130 nM KSA, droplet coarsening was enhanced. At 230 nM KSA, the mean droplet size peaked around 2 hours, and then entered a dynamic steady state characterized by constant average droplet size.

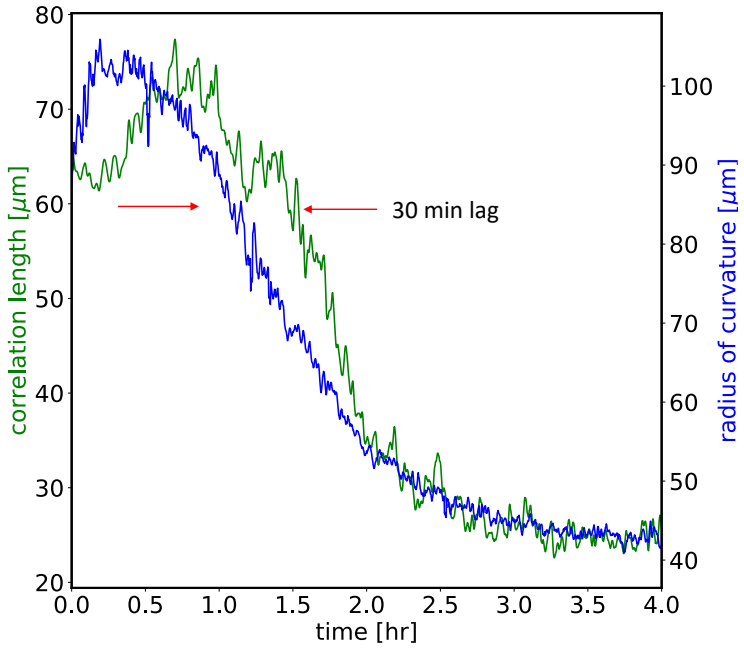


Figure B.5: **Early evolution of correlation length and inverse curvature for 230 nM KSA.** In the first 2 hours of the experiment, correlation length development lagged behind that of the average interface curvature. Subsequently, the rate of change of both quantities coincided as the system approached the steady state.

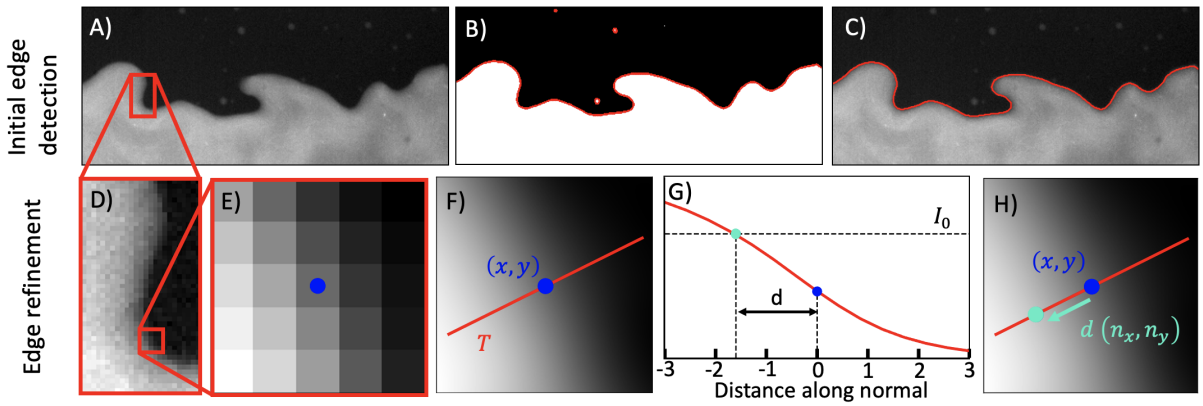


Figure B.6: **Detection of bulk-phase-separated interfaces.** (**A**) Dextran fluorescence image. (**B**) The thresholded image, with edges detected using the Sobel filter shown in red. (**C**) After skeletonizing and pruning the largest component, the edge roughly contours the interface. (**D**) A small section of the interface. (**E**) A magnified region surrounding a point $(x, y)$ on the interface. (**F**) Image intensity in (E) is interpolated using a 2D spline (grayscale). Red line is parallel to the local normal $(n_x, n_y)$ to the interface. (**G**) Interpolated image intensity along the local normal. The distance d along the normal is defined where the intensity is equal to the threshold. (**H**) The interface position is defined to be $(x, y) + d(n_x, n_y)$

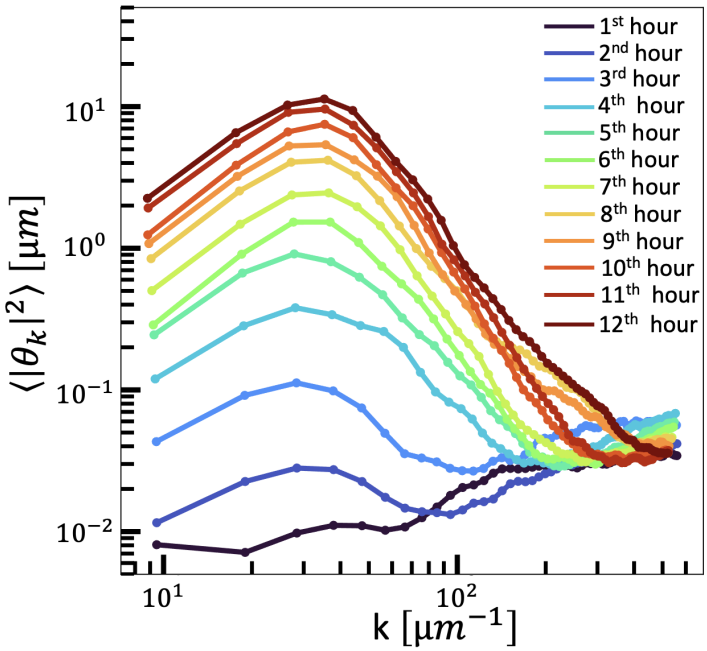


Figure B.7: **Tangent angle power spectrum as a function of time, averaged over one-hour intervals after sample preparation.** Although the amplitude of fluctuations increases over time, after ≈ 6 hours, the shape of the fluctuation spectrum remains nearly constant.

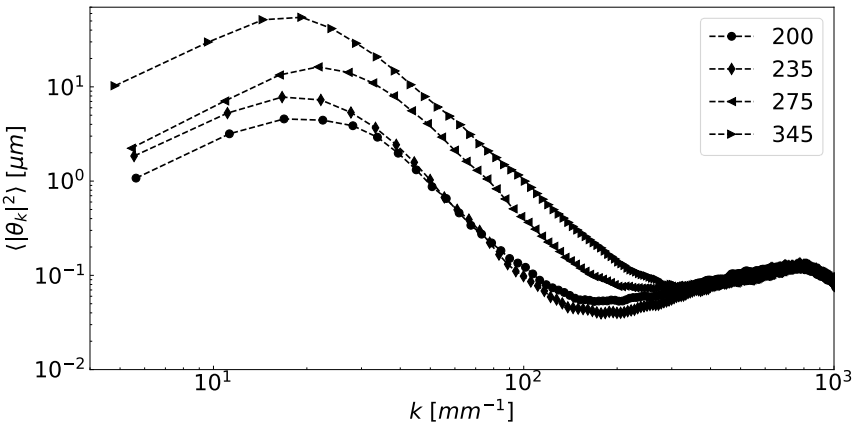


Figure B.8: **Experimental tangent angle spectra extended to $k = 10^3$ mm$^{-1}$.** Tangent angle measurement noise increases as $\sim k^2$, resulting in a secondary peak at $k \sim 8 \cdot 10^2$ mm$^{-1}$ where all spectra overlap. Legend denotes KSA concentrations in units of nM.

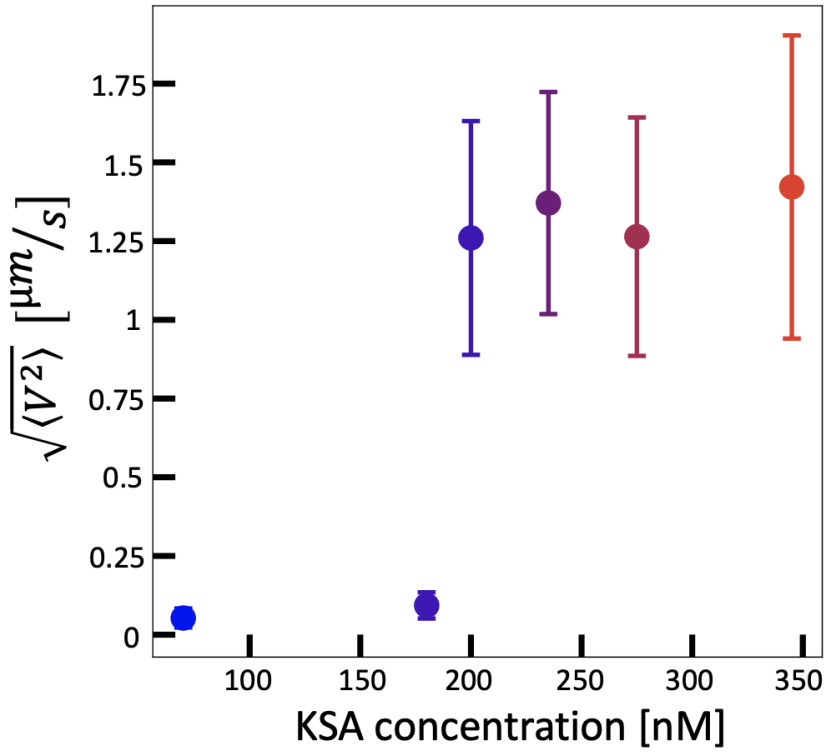


Figure B.9: **Root-mean-square velocity of active phase as a function of kinesin concentration averaged from 6 to 8 hours after sample preparation.** Below 200 nM KSA, the speed decreases significantly. Above 200 nM KSA, the speed is approximately constant. Error bars show standard deviation.

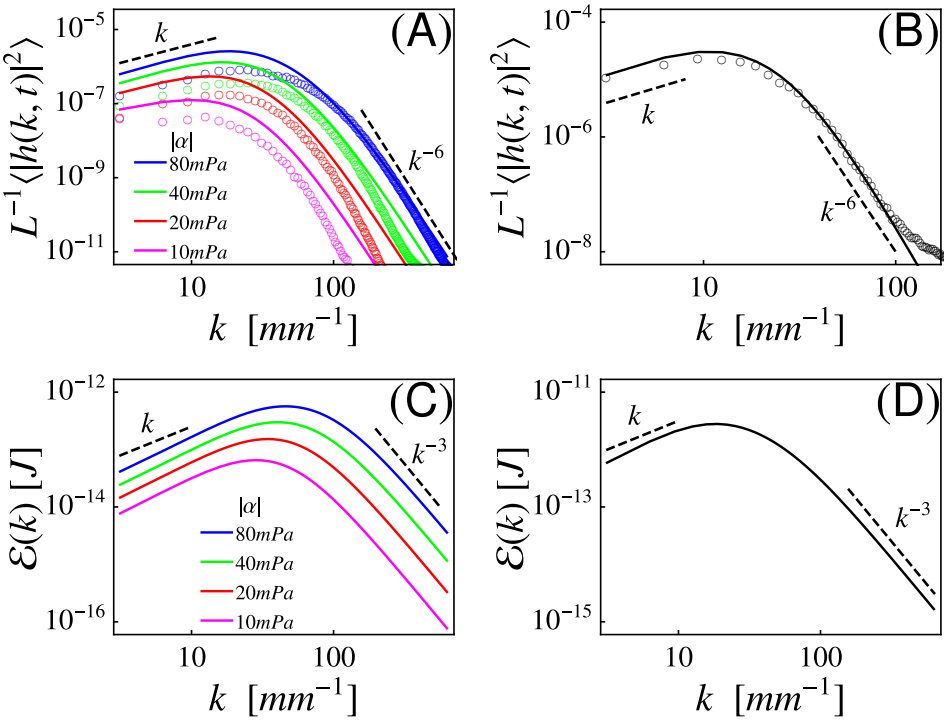


Figure B.10: **Fluctuation of active interfaces at different activities.** (**A-B**) Fluctuation spectra of interfaces from (A) simulations and (B) experiment. Solid lines are theoretical values calculated using Eq. (B.31), while circles are height spectra extracted from either simulations or experiments. For simulations, $\sigma_{rms}^2 = \alpha^2 \bar{S}^2/8$, where $\bar{S}$ is the mean nematic order parameter at the steady state. The correlation legnth $\ell_a$, correlation time $\tau_a$, and $\bar{S}$ were measured from simulations. Since all other parameters are known, no fitting parameter is used here. (**C-D**) Energy spectra $\mathcal{E}(k)$ calculated using (B.30) with parameters from (C) simulations and (D) experiment. The 200 nM KSA data set is used to obtain results in panels B and D. We used the following parameters to calculate the energy and interface fluctuation spectra: interfacial tension $\gamma = 0.177$ $\mu$N/m, density difference $\Delta\rho = 8.9$ kg/m$^3$, viscosity $\eta = 25$ mPa·S, friction $\gamma_v = 100$ MPa. The correlation length and time of active stress $\ell_a = 50$ $\mu$m and $\tau_a = 80$ sec were used in (B) and (D). Magnitude of active stress $\sigma_{rms}$ is used as a fitting parameter, and the best fit gives $\sigma_{rms} = 2.47$ mPa.

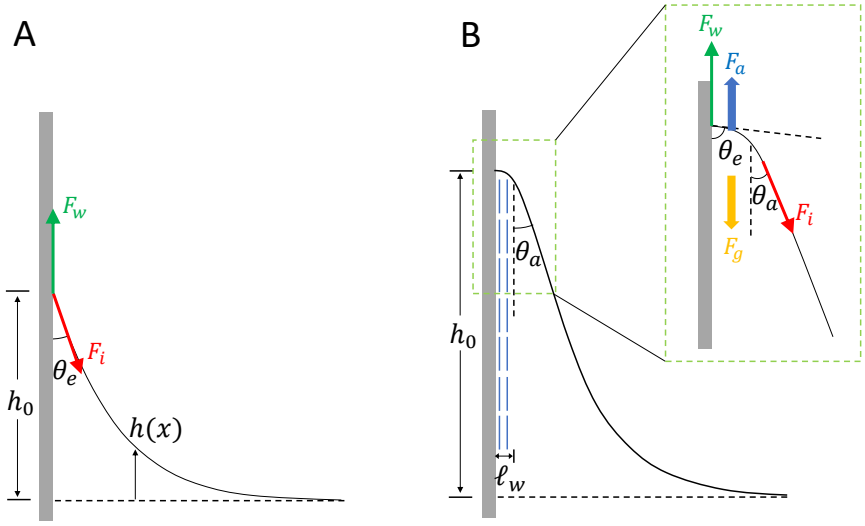


Figure B.11: (**A**) Sketch of the wetting profile of a passive liquid-air interface defined by $y = h(x)$. The wall tension $\gamma_w$ is determined by $\gamma_w = \gamma_{wall-air} - \gamma_{wall-liquid}$. (**B**) Sketch of activity-induced wetting. The inset shows the geometry and force balance close to the contact point.

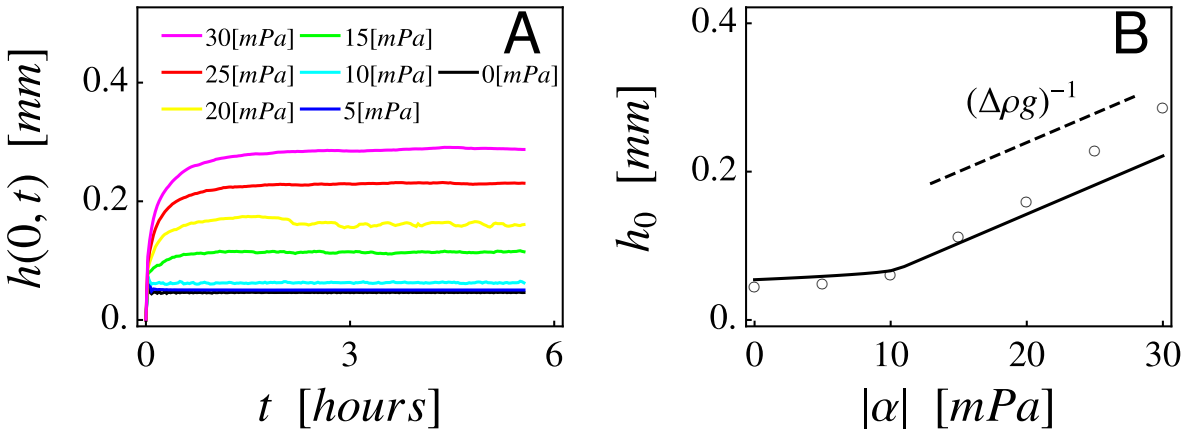


Figure B.12: **Evolution of height of interface contact point with activity.** (**A**) Height of contact point as a function of time at different activities obtained from numerical simulations of the continuum model. Since there are two vertical walls, we use the average height of the contact points at the two walls. (**B**) Steady state height of contact point $h_0$ as a function of activity. The circles are obtained from simulations as $h_0 = (t_s - t_0)^{-1} \int_{t_0}^{t_s} h(0,t)dt$, with $t_0 = 7200S$ and $t_s = 20000S$. The solid line shows the theoretical value given in Eq. (B.40) with $\ell_w = 2.5\mu m$. The dashed line shows the predicted slope $1/\Delta\rho g$. In both figures we have used a passive contact angle $\theta_e = 10$ degree.

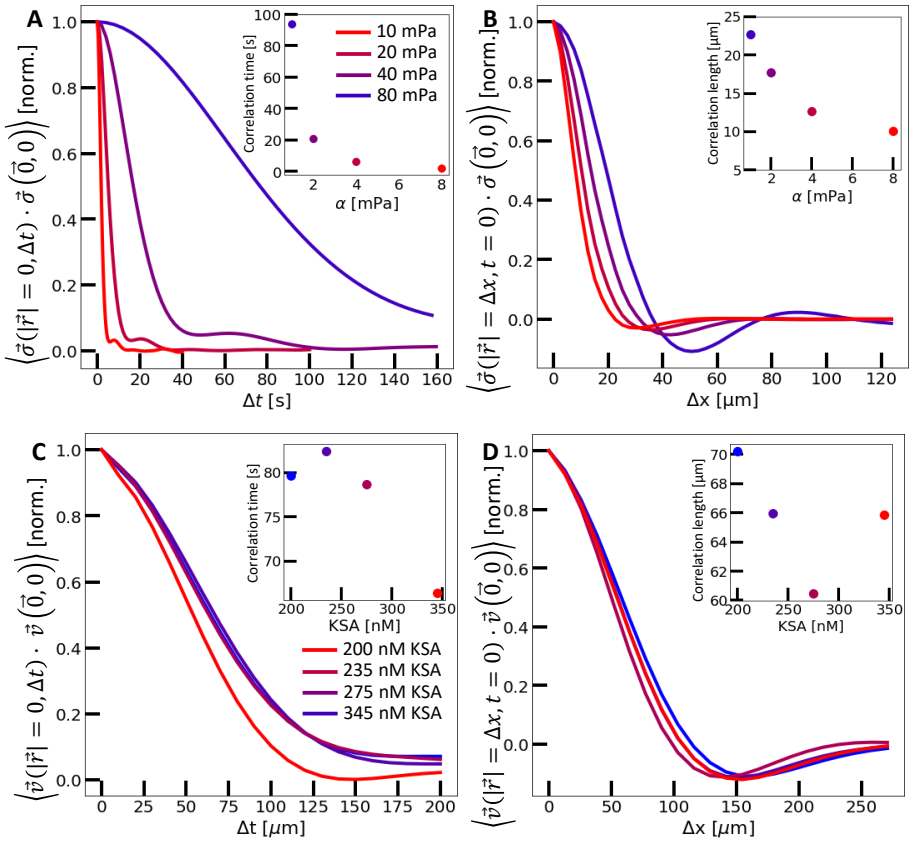


Figure B.13: **Measurement of bulk spatiotemporal autocorrelations in simulations and experiments.** (**A**) Normalized time correlation of active stresses in numerical simulations. Inset: Correlation time decreases with increasing activity. (**B**) Normalized space correlation of active stress in numerical simulation. Inset: Correlation length decreases with increasing activity. (**C**) Normalized time correlation of velocity in experiment. Inset: Correlation time shows little variation with activity. (**D**) Normalized space correlation of velocity in experiment. Inset: Correlation length shows little variation with activity. Velocity (stress) autocorrelations were computed by averaging the scalar products of bulk velocity (stress) fields with their displacement in time $\Delta t$ and space $\Delta x$. Correlation times and length were defined where the correlation curve reaches $1/e$.

# Appendix C

# Appendix for colloidal vesicles

## C.1 Experimental Materials and Methods

### C.1.1 Phage production

Litmus is a phagemid, meaning that its DNA does not containing the necessary code to produce viral proteins. Producing litmus requires the addition of a helper phage to generate the necessary viral proteins. M13K07 is a standard helper phage, and was grown following previously established protocols[157]. The E. coli strain ER2738 was infected with M13K07 and incubated in LB media at 37 C. After viral proliferation, it was separated from the bacteria via multiple rounds of centrifugation. To purify the virus, 20 g/L PEG 8 kDa and 20 g/L NaCl were added to the solution, causing viruses to form a dense precipitate. The virus was then pelleted in an ultracentrifuge and resuspended in 20 mM Tris-HCl buffer to form the M13K07 stock solution for infecting cells.

Litmus requires a different growth protocol than M13K07 due to its nature as a phagemid [101, 157]. The Litmus plasmid was transformed into competent cells (NEB 5-alpha F'), and grown in liquid media in overnight starter cultures. 2 $\mu$L of 60 mg/mL

M13KO7 stocks were added to the bacterial stocks to begin phage production. M13KO7 confers kanamycin resistance to the cells. The cells are cultured in 2XYT media with 100 $\mu$g/mL ampicilin, 25 $\mu$g/mL kanamycin, 1 mM MgCl2 and 1mM MgSO4 [18]. Both Litmus and M13KO7 are exuded from infected bacteria throughout growth.

We started purification by separating the bacteria from the phage via several rounds of centrifugation. First, most bacteria was removed through a low-speed round of centrifugation (10 min at 4,000xg, Fiberlite F9-6 x 1000 LEX fixed angle rotor, Thermo Scientific) followed by a second high-speed round (15 min, 12,000xg), collecting the supernatant which contained the phage. The supernatant was then filtered through a 0.22 $\mu m$ filter, which allowed th phage to pass through, while removing any remaining bacteria. The phage was then condensed out of solution by adding 50 g/L PEG 8 kDa (Sigma-Aldrich) and 30 g/L NaCl. The condensed phage was centrifuged out of solution (30 min at 12,000 xg), and resuspended in 20 mM tris-HCl, pH 8 buffer. To increase the phage purity, we preformed two additional cycles of centrifugation, where the solution was first spun at 45,000 xg for 15 minutes to remove bacterial debris, followed by the addition of 50 g/L PEG 8 kDa and 30 g/L NaCl to precipitate the phage with a 45,000 xg spin for 15 minutes to pellet the phage. These rounds further separated the phage from the supernatant which contained bacterial debris.

After puification, the virus suspension contained both M13K07 and Litmus, requiring phase separation to obtain a monodisperse sample of Litmus. Dextran was added to the mixed growth product which, at critical concentration, induced the isotropic to nematic phase transition in M13KO7 but not the Litmus. After one round of centrifugation at 21,000 xg for 15 minutes, the condensed nematic phase containing primarily M13KO7 settles to the bottom of the centrifuge tube, while the Litmus remains in the upper isotropic phase. The isotropic phase was collected to create litmus stock. Gel electrophoresis was used to confirm separation of M13KO7 and litmus. An optional purification step to fur-

ther clean the phages using an anion exchange column (POROS, GoPure XQ 0.5 cmD x 5 cmL COLUMN) using an established protocol [Monjezi2010]. The additional rounds of purification increased membrane size and the frequency of vesicle formation from a few vesicles per sample, to many hundreds [Fig. C.3].

### C.1.2 Sample preparation

Each experiment required a multi-day preparation to form membranes. Vesicle samples were composed of DyLight-550 fluorescently-labeled phage and 500 kDa dextran in a 125 mM NaCl, 20 mM Tris-HCl, pH8 buffer. At pH 8, Viral particles are negatively charged, producing electrostatic repulsion that prevents membrane formation. Salt acts to screen the electrostatic repulsion, and dextran acts as a polymer depletant, inducing an entropically-driven attraction between the phages [14, 96, 158]. The balance between the screened electrostatic force and the depletion force leads to the alignment of phages and, ultimately, the self-assembly of colloidal membranes.

Low-polydispersity dextran was found to produce significantly cleaner and larger membranes, resulting in more frequent vesicles. Dextran (Mr 500,000 Da, Sigma-Aldrich) was separated into fractions with narrow molecular weight distributions via Ethanol precipitation. Ethanol was gradually added to a solution of 0.2% dextran under vigorous stirring at 23 °C. After reaching 31% (w/w) ethanol, dextran precipitates were removed by centrifugation (20 min at 17,000g, Fiberlite F9-6 x 1000 LEX fixed angle rotor, Thermo Scientific). Ethanol was then added to a concentration of 32% (w/w). The precipitate was collected by centrifugation and resuspended in water. Solvent was removed by freeze-dry lyophilization, and the powder was reconstituted in water to 100 mg/mL dextran. This stock solution was used to make vesicle samples.

Samples were confined to a glass chamber that was coated with an Acrylamide poly-

mer brush to prevent adsorption following established protocols [159]. Chambers were made using a microscope slide and coverslip, separated by parafilm spacers. The number of layers of parafilm was chosen to set the desired thickness of the chamber. Chambers made using at least three layers of parafilm for a thickness of $> 500\ \mu m$ consistently formed closed isolated vesicles, while in thinner chambers, vesicles were rarely able to tear away from the top surface. Chambers up to 3 mm thick were used to take data for the pendent vesicles. Samples were prepared using at variable concentration, depending on the thickness of the chamber. Since membranes sediment to the bottom of the chamber, 3 mm chambers needed to have lower final phage concentration (0.4 mg/mL) than in 500 $\mu m$ chambers (1 mg/mL) to achieve the same density of membranes at the surface.

Samples were prepared at a final concentration of 54 mg/mL fractionated 500 kDa dextran, in a 125 mM NaCl 20 mM tris-HCl buffer at pH 8. Directly after sample preparation samples were loaded into the chamber, and then sealed with NOA glue. The sample was then stored overnight with the microscope slide facing downward. One day after sample preparation, Litmus membranes layered the bottom of the chamber and began to curve upward against gravity [Fig. C.2]. The sample chamber was then inverted so that the coverslip faced downward. To image membrane extension and tearing, samples were immediately placed on a spinning disk confocal microscope and imaged with a 40x water immersion objective (N40XLWD-NIR), to limit axial distortion. To image fully formed vesicles, the chamber was left inverted for a day or more, and the resulting vesicles were imaged as before.

### C.1.3 Dialysis chamber

The buffer exchange experiments took place in a dialysis device as is shown in [Fig. C.5]. Holes were drilled into standard microscope glass slides, which were then coated

with an Acrylimide brush, following standard protocol [159]. Following this coating, slides were cleaned and dried. A 20 kDa dialysis membrane was glued on the top surface of the slide, covering the drilled holes. A PDMS buffer exchange chamber was then glued over top of the dialysis membrane. On the opposing side of the microscope slide, a chamber was formed using a coverslip with 600 $\mu m$ of parafilm as a spacer. An assembled view of the chamber is shown in [Fig. C.5a]. The bottom chamber was filled with the sample (0.5 mg/mL phage, 54 mg/mL dextran in 125 mM NaCl 20 mM tris-HCl, pH 8), and sealed with NOA glue. The top buffer-exchange chamber was filled with Litmus buffer (125 mM NaCl 20 mM Tris-HCl, pH 8), and sealed with a flexible epoxy. The sample was stored overnight with the coverslip facing up to form membranes on the microscope glass side of the chamber. The chamber was then inverted so that the coverslide faced downward and was stored for an additional day, to form vesicles on the bottom coverslip. The flexible epoxy was peeled off the PDMS chamber, the dialysis chamber was flushed with air, and filled it with 0 mM NaCl 20 mM Tris-HCl buffer. The salt in the sample diffused out of the chamber over the course of several hours, while the resulting vesicle shape change was recorded using a confocal microscope.

### C.1.4 Contouring vesicles

To contour the vesicles, the 3D confocal images were imported into Fiji. Initial rough contours of fluorescent objects in each image were found using the Ridge Detector plugin [160]. This generated a mask that roughly contoured the vesicle, but included noise other membrane objects which did not belong to the vesicle of interest. To further filter the images, we recognize that the z-scans of the membranes are composed of roughly-circular cross sections. We then fit each image in the z-scan with a circle using a RANSAC algorithm. This picked out pendent-membrane-like objects, while rejecting line-like cross

sections that make up other membranes. The Z-stacks of the circular fits acted as an initial point cloud which was converted into a mesh using MeshLab [161]. This point cloud was cleaned from outliers using the filters "simplify point cloud" and "Compute Normal for Point Set". These points were then used to construct a surface using the filter "Ball Pivoting". Each mesh was then visually inspected, and manually repaired wherever meshes contained self-intersections or holes.

The cleaned meshes were then put through a final round of processing. In the above-described contouring scheme, vesicles were assumed to have a perfectly circular cross section, and were manually inspected and repaired, both of which introduce artifacts to the final vesicle contour. To remedy this, we developed an iterative algorithm to evolve the initial mesh by attracting it toward regions of high intensity. To begin, First-order directional derivatives of the image were taken using a difference-of-Gaussian filter. Each point on the mesh is acted on by a force, $\overrightarrow{F} = \alpha \overrightarrow{\nabla} I$, where $\alpha$ is an arbitrary constant and $I$ is the image intensity. This acts to draw each point comprising the mesh up the gradient. This algorithm was iterated until it converged on the region of highest intensity. In practice, each point moved several pixels, settling within roughly one hundred iterations. This method provided a consistent technique for detecting the vesicle contour, given an accurate initial guess for the mesh.

## C.2 Estimating membrane properties

### C.2.1 Membrane relaxation time

To estimate the rate of membrane relaxation, we will use the known result [162, 93]

$$\Gamma(l) = \frac{\kappa_c}{\eta R_0^3} \frac{(l-1)l^2(l+1)^2(l+2)}{(2l+1)(2l^2+2l-1)}$$

for bending dominated energy. The longest time scale is at $l = 2$, which is given by

$$\tau = \frac{55}{144}\frac{\eta R_0^3}{\kappa_c}$$

Which, for $\kappa_c = 11,000 k_B T$, $R_0 \approx 100\mu m$ and the viscosity of the solute is $\eta \approx 5mPas = 1.2 k_B T s/\mu m^3$, we get $\tau = 41s$.

### C.2.2 Density Estimate

To estimate the arial density of the membrane, we measured the density of virus rod suspensions in a concentrated solution using an oscillating U-tube density meter (DMA 4100, Anton-Paar). We found that the density of the tris buffer is $\rho_{tris} = 0.9994 g/cm^3$ and the density of the virus solution at 41 $mg/mL$ is $\rho_{litmus}(41 mg/mL) = 1.0130 g/cm^3$.

Previous work used small-angle x-ray scattering measured fd-wt membranes at 56 mg/mL dextran were condensed to $290 mg/mL$ [16]. Because the length of the rod should not change the membrane density, since the change per unit length and the osmotic pressure both scale with the length of the rod, we can assume that the Litmus membranes will be nearly 290 $mg/mL$. We can then extrapolate the density difference to be:

$$\Delta\rho_{litmus}(260 mg/mL) = \frac{1.0130 g/cm^3 - 0.9994 g/cm^3}{41 mg/mL}(290 mg/mL) = 0.096 g/cm^3$$

So the arial density is:

$$\Delta\sigma = (368nm)(\frac{1cm}{10^7 nm})0.096 g/cm^3 = 3.7 * 10^{-6} g/cm^2$$

From which we find that:

$$\Delta\sigma g = (3.7 * 10^{-6} g/cm^2) * (980 cm/s^2) = 3.6 * 10^{-3} \frac{g}{cms^2} = 0.075 \frac{k_B T}{\mu m^3}$$

### C.2.3 Out of plane fluctuation spectrum

The bending energy, $\kappa_c$ was experimentally measured by imaging out-of-plane fluctuations of small flat membranes suspended from the top of the chamber [Fig. C.4A]. The center cross-section perpendicular to the plane of the membrane was imaged at 20 ms intervals [Fig. C.4B,C]. The initial contour of this cross section was found by determining the maximum intensity along each vertical line, h(x), using a first order Savitzky-Golay filter. This contour was refined to subpixel accuracy along each point on the contour by interpolating a 5x5 pixel neighborhood around each point (x, y). Gradients of this interpolated regions were used to find the normal. We then determinined the sub-pixel interface position along this normal that is equal to a predefined intensity value.

To process the data, the mean contour was subtracted from each timepoint. To account for non-periodicity, the signal was first multiplied by a Hanning function and rescaled to preserve the fluctuation amplitude before the power spectrum was calculated. The power spectrum was fitted with the equation

$$\langle |A^2(q)| \rangle = \langle \epsilon^2 \rangle + \frac{k_B T q}{\sigma} \left(1 - \frac{1}{\sqrt{1 + \sigma/\kappa_c q^2}}\right) \tag{C.1}$$

where $\langle \epsilon^2 \rangle$ is a fitting parameter for the noise and $\sigma$ is the lateral tension. This equation is appropriate for fitting the fluctuations of a one-dimensional cut along a two dimensional sheet [97]. This was done for three separate membranes, to measure an average of $\sigma = 370 \pm 90 k_B T/\mu m^2$, $\kappa_c = 11000 \pm 1000 k_B T$ and $\langle \epsilon^2 \rangle = 3.5 \pm 0.2 * 10^{-4} \mu m$ [Fig. C.4D].

### C.2.4 In plane fluctuation spectrum

Flat Litmus membranes at the bottom of the chamber were imaged using DIC microscopy, at 20 ms intervals [Fig. C.6A]. Edges were contoured by first finding the maximum value h(x) for each point along x in the image, and then refined to subpixel accuracy for each point on the contour by interpolating a 5x5 pixel neighborhood around each point (x, y). Gradients of this interpolated regions were used to find the normal. Sub-pixel interface position along the normal is defined so that the interpolated image intensity equals a predefined threshold value along the entire interface. The power spectrum was calculated and fitted with the equation

$$\langle |A^2(q)| \rangle = \langle \epsilon^2 \rangle + \frac{k_B T}{\gamma q^2 + \kappa_B q^4}$$

where $\langle \epsilon^2 \rangle$ is a fitting parameter for the noise and $\kappa_B$ is the edge bending energy [Fig. C.6B] [163]. This was done for nine separate membranes, to measure an average of $\gamma = 350 \pm 20 k_B T/\mu m$ and $\kappa_B = 1000 \pm 100 k_B T \mu m$ [Fig. C.6C].

## C.3 Numerical methods for shape analysis

### C.3.1 Energy and coordinate system

For shape analysis, we will focus on axisymmetric membranes. Here, we use the coordinates

$$e_s = \begin{pmatrix} r'(s) \\ z'(s) \\ 0 \end{pmatrix} = \begin{pmatrix} \cos\psi(s) \\ \sin\psi(s) \\ 0 \end{pmatrix}, \quad e_\phi = \begin{pmatrix} -r(s)\sin(\phi) \\ r(s)\cos(\phi) \\ 0 \end{pmatrix}. \tag{C.2}$$

where $\psi(s)$ is the local tangent angle parameterized by the arclength and $\phi$ is the az-

imuthal angle, as shown in figure C.1.

For the most general case, we have to consider the gravitational energy, curvature energy and edge terms

$$E = \int \left[\frac{\kappa_c}{2}(2H)^2 + \bar{\kappa}K_G + \sigma g z + \mu\right]dA + \int q(r_s - \cos\psi) + \int \eta(z_s + \sin\psi) + \gamma \int dL + P\int dV \quad \text{(C.3)}$$

with the Lagrange multipliers $\mu$ to keep the surface area constant, $q(s)$ to account for $r_s = \cos\psi$, $\eta(s)$ to account for $z_s = -\sin\psi$ and P to account for the constant volume. In this parameterization, the energy can be written as

$$E = 2\pi \int \left[\frac{\kappa_c}{2}\left(\psi_s + \frac{\sin\psi}{r}\right)^2 + \overline{\kappa}\psi_s\frac{\sin\psi}{r} + \sigma g z + \mu\right] r ds + \int q(r_s - \cos\psi)ds + \int \eta(z_s + \sin\psi)ds + \gamma\int dL + P\int r^2\sin\psi ds \quad \text{(C.4)}$$

From this general case, we solve for experimentally relevant examples:

### C.3.2 Closed vesicles

For closed vesicles, we do not need the line tension term, leaving

$$E = 2\pi \int \left[\frac{\kappa_c}{2}\left(\psi_s + \frac{\sin\psi}{r}\right)^2 + \overline{\kappa}\psi_s\frac{\sin\psi}{r} + \sigma g z + \mu\right] r ds + \int q(r_s - \cos\psi)ds + \int \eta(z_s + \sin\psi)ds + P\int r^2\sin\psi ds \quad \text{(C.5)}$$

To solve these equations we first take the variation along $\psi$ to get the Euler-Lagrange equation

$$-\kappa_c r\psi_{ss} - \kappa_c \cos\psi\psi_s + \kappa_c \frac{\sin\psi\cos\psi}{r} + q\sin\psi + Pr^2\cos\psi = 0$$

Next, can take the variation along $r$ to get the equation

$$\frac{\kappa_c}{2}\psi_s^2 - \frac{\kappa_c}{2}\frac{\sin^2\psi}{r^2} + \mu - q_s + \sigma g z + 2Pr\sin\psi = 0$$

Taking variation in V gives

$$P_s = 0$$

Taking the variation in z gives

$$\eta_s = \sigma g r$$

Lastly, we have the equations

$$r_s = \cos\psi$$

$$z_s = -\sin\psi.$$

We can then define the arclength in terms of the reduced arclength, so that $t = s/L$, where L is the arclength of the curve. These equations can be recast into the system of first-order ODE's

$$
\begin{aligned}
\frac{d\psi}{dt} &= L\psi_s \\
\frac{d\psi'}{dt} &= -L\frac{\cos\psi\psi_s}{r} + L\frac{\sin\psi\cos\psi}{r^2} + L\frac{q}{r\kappa_c}\sin\psi + L\frac{\eta}{r\kappa_c}\cos\pi + Pr^2\cos\psi \\
\frac{dr}{dt} &= L\cos\psi \\
\frac{dz}{dt} &= -L\sin\psi \\
\frac{dq}{dt} &= L\frac{\kappa_c}{2}\psi'^2 - L\frac{\kappa_c}{2}\frac{\sin^2\psi}{r^2} + L\mu + L\sigma gz + 2Pr\sin\psi \\
\frac{dA}{dt} &= 2\pi rL \\
\frac{d\mu}{dt} &= 0 \\
\frac{d\eta}{dt} &= L\sigma gr \\
\frac{dL}{dt} &= 0 \\
\frac{dP}{dt} &= 0 \\
\frac{dV}{dt} &= Lr^2\sin\psi.
\end{aligned}
\tag{C.6}
$$

We need eleven boundary conditions to solve this system. To begin with, we enforce five boundary condition at the top center of the vesicle where the tangent angle is zero, the radius is zero, the height is zero, the integrated area is zero and the integrated volume is zero, leading to the five conditions:

(1) $\psi(0) = 0$

(2) $r(0) = 0$

(3) $z(0) = 0$

(4) $A(t = 0) = 0$

(5) $V(t = 0) = 0$

We also have that at the bottom of the vesicle, the radius in contact with the floor is

set to $R$ and the integrated area is $A_0 - \pi R^2$ the integrated volume is $V_0$ and the tangent angle is $\pi$, giving the four conditions:

(6) $r(t=1) = R$

(7) $A(t=1) = A_0 - \pi R^2$

(8) $\psi(t=1) = \pi$

(9) $V(t=1) = V_0$

We also have two additional condition. The first is that the Hamiltonian is zero at the bottom by the transversality condition [164]. This gives

$\mathcal{H}(0) = \psi' \frac{\partial \mathcal{L}}{\partial \psi'} + r' \frac{\partial \mathcal{L}}{\partial r'} - \mathcal{L} = 0$

$= \frac{\kappa_c r}{2}(\psi_s^2 - sin(\psi)^2/r^2) - \mu r + qcos(\psi) - \eta sin(\psi) - \sigma g r z|_{s=0}$

which reduces to

(10) $q(0) = 0$

The final boundary condition comes from having zero gravitational force at the bottom

(11) $\eta(0) = 0$

This system of equations can then be solved in any ODE solver, and requires only the radius of the contact with the bottom surface, the total surface area and the total volume as free parameters, which can each be experimentally measured.

### C.3.3 Pendent vesicle

To model pendent membranes, the only major difference energetically is the presence of an open pore at the top. However, this term is $E_{edge} = \gamma \int dL$. Since the width of the top opening will be a fixed radius measured experimentally, this term will not enter into the Euler-Lagrange equations. Therefore, the energy is identical to C.5, and the the Euler-Lagrange equations will be identical to C.6. However, the boundary conditions will be changed.

To begin with, we enforce the four boundary condition at the top of the pendent vesicle, the radius is fixed at a constant $R$, the integrated area is $A_0$ the integrated volume is $V_0$, the height is zero and the tangent angle is fixed to ensure a vanishing bending moment such that $\psi_s = -(1 + \frac{\sin\psi}{r})$, giving the five conditions:

(1) $r(t =) = R$

(2) $A(t = 1) = A_0$

(3) $\psi_s(t = 1) = -(1 + \frac{\sin\psi}{r})$

(4) $V(t = 1) = V_0$

(5) $z(0) = 0$

At the bottom of the pendent vesicle, the tangent angle is zero, the radius is zero, the integrated area is zero and the integrated volume is zero, leading to the four conditions:

(6) $\psi(0) = 0$

(7) $r(0) = 0$

(8) $A(t = 0) = 0$

(9) $V(t = 0) = 0$

We retain the two additional condition from the previous section:

(10) $q(t = 0) = 0$

(11) $\eta(t = 0) = 0$

These can again be solved using any ODE solver, with experimentally measured values as inputs.

### C.3.4 Single pores vesicles

To model the single pore evaporating vesicles, we will use the energy functional above, with minor modifications. First, since the vesicle has an open pore, we will assume that the volume is equilibrated to the minimum energy (P = 0). We also assume that the

gravitational energy does not contribute, since the vesicles we are describing are generally small. This gives the energy functional:

$$E = 2\pi \int \Big[\frac{\kappa_c}{2}\big(\psi_s + \frac{\sin\psi}{r}\big)^2 + \overline{\kappa}\psi_s\frac{\sin\psi}{r} + \mu\Big] r ds + \int q(r_s - \cos\psi) ds + \gamma \int dL \quad \text{(C.7)}$$

By construction:

$\frac{d\psi}{ds} = L\psi'$

$\frac{dr}{ds} = L\cos\psi$

$\frac{dz}{ds} = -L\sin\psi$

$\frac{dA}{ds} = 2\pi r L$

$\frac{dL}{ds} = 0$

$\frac{d\mu}{ds} = 0$

Taking variation in $\psi$ gives

$\frac{d\psi_s}{ds} = -L\frac{\cos\psi\psi'}{r} + L\frac{\sin\psi\cos\psi}{r^2} + L\frac{q}{r\kappa_c}\sin\psi.$

Taking variation in r gives

$\frac{dq}{ds} = +L\frac{\kappa_c}{2}\psi'^2 - L\frac{\kappa_c}{2}\frac{\sin^2\psi}{r^2} + L\mu.$

To solve these equations, we need eight boundary conditions. The radii of the single pore is:

(1) $r(0) = r_1$

and the position of hole is set by

(2) $z(0) = 0$

The surface area of the contour gives the conditions

(3) $A(t = 0) = 0$

(4) $A(t = 1) = A$

We also have zero bending moment on the open boundary

(5) $\psi_s(t=0) = -(1+\frac{\psi}{r})$

At the opposite pole of the membrane we have that

(6) $r(t=1) = 0$

(7) $\psi(t=1) = 0$

And finally, we have that the Hamiltonian is zero by the transversality condition:

(8) $\mathcal{H}(0) = 0$

This now requires $r_1$ and the total surface area as input parameters, both of which can be measured experimentally. We find the predicted cross sections of single pore vesicles fit well with the experimental data [Fig. 4.11A,B].

### C.3.5 Two pores vesicles

To model the two pore system, we use the energy functional as the single pore membrane C.7, with altered boundary conditions. Six of the boundary conditions are unchanged:

(1) $r(0) = r_1$

(2) $z(0) = 0$

(3) $A(t=0) = 0$

(4) $A(t=1) = A$

(5) $\mathcal{H}(0) = 0$

(6) $\psi_s(t=0) = -(1+\frac{\psi}{r})$

The two altered boundary conditions account for the second open pore:

(7) $r(t=1) = r_2$

(8) $\psi_s(t=1) = -(1+\frac{\sin\psi}{r})$

This now requires $r_1$, $r_2$ and the total surface area as input parameters, which can each be measured experimentally.

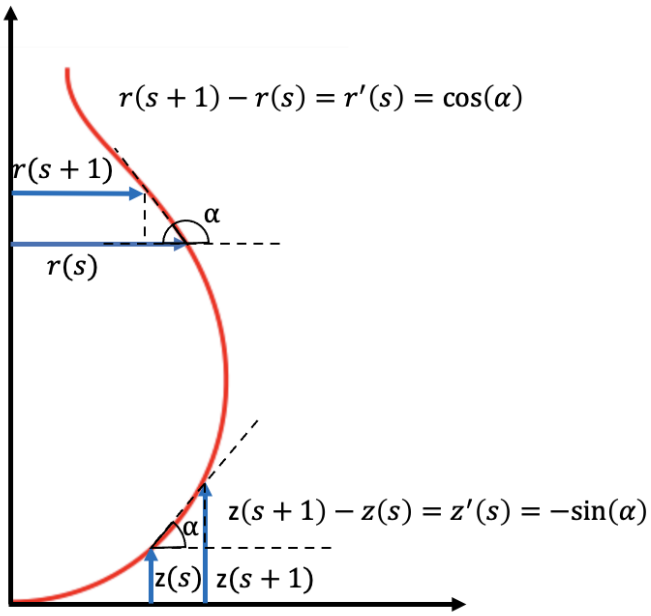


Figure C.1: Coordinate system used to solve Euler-Lagrange equations and to predict vesicle shape.

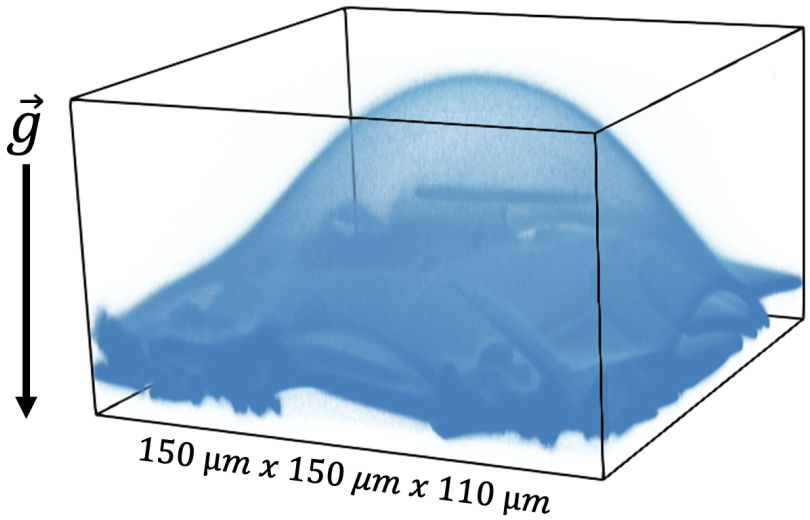


Figure C.2: Typical membrane seen a the bottom of the chamber, just before inversion. The membrane is curving upward but has not closed into a vesicle.

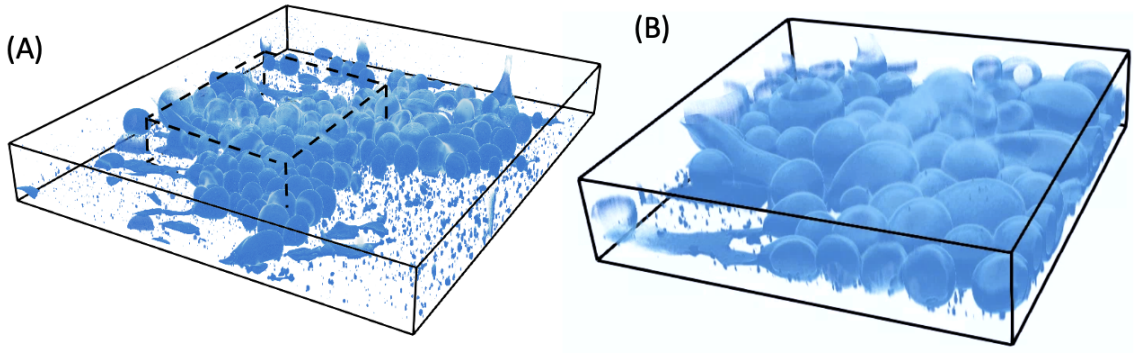


Figure C.3: **Dense grouping of vesicles seen in experiment.** Over an imaging area of 2 mm x 2.3 mm, 72 closed vesicles were densely packed together. (**A**) 3D rendering of the entire patch of vesicles (**B**) and a higher resolution image showing a 880 $\mu m$ x 880 $\mu m$ area.

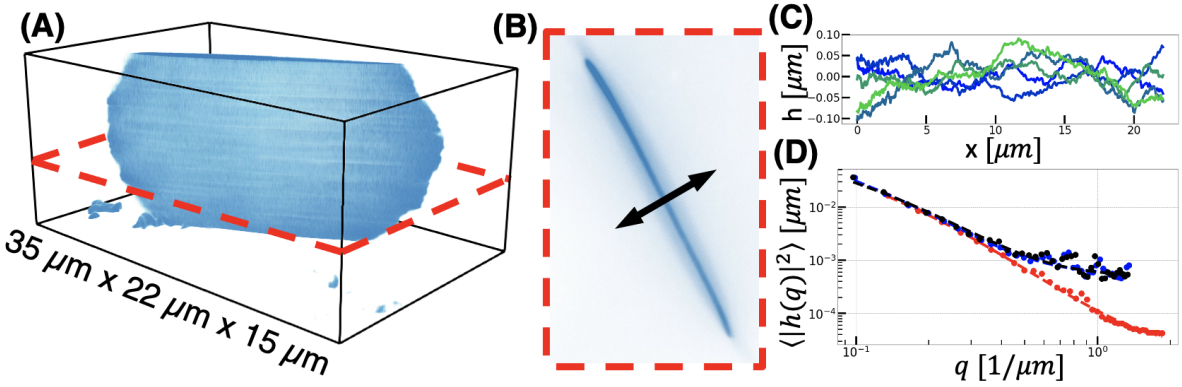


Figure C.4: **Out-of-plane fluctuation analysis to measure material properties.** (**A**) A flat Litmus membrane suspended from the chamber top. (**B**) Center-slice of the membrane. Direction of out-of-plane fluctuations indicted by arrow. (**C**) Typical fluctuations seen in experiment. (**D**) The fluctuation spectrum for three samples. Black and blue contours were taken with 100x magnification and the red contour at 150x magnification.

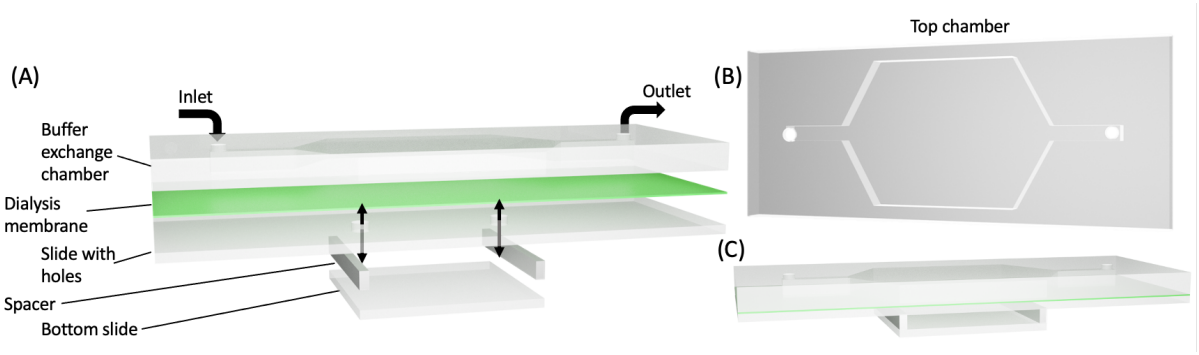


Figure C.5: **Schematic of dialysis chamber.** (**A**) An exploded view of the dialysis device with key components labeled. (**B**) View of the top buffer exchange chamber, showing the shape of the channel. (**C**) The assembled chamber.

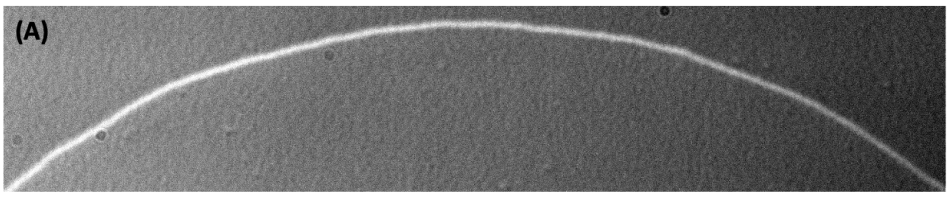


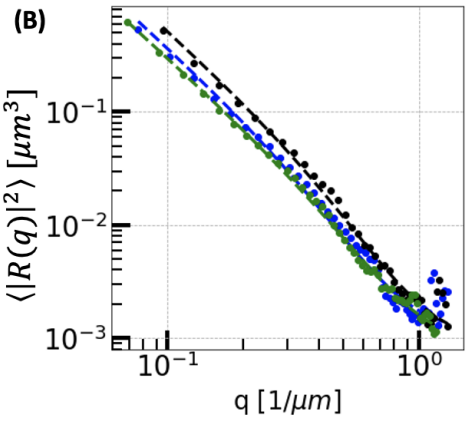


| (C) | $\gamma$ [$k_bT/\mu m$] | $\kappa_b$[$k_bT$ $\mu m$] |
|---|---|---|
| Sample 1 | $620 \pm 20$ | $1200 \pm 200$ |
| Sample 2 | $260 \pm 20$ | $1300 \pm 200$ |
| Sample 3 | $190 \pm 20$ | $700 \pm 100$ |
| Sample 4 | $330 \pm 10$ | $1000 \pm 100$ |
| Sample 5 | $300 \pm 20$ | $800 \pm 100$ |
| Sample 6 | $260 \pm 30$ | $600 \pm 100$ |
| Sample 7 | $390 \pm 20$ | $1900 \pm 300$ |
| Sample 8 | $310 \pm 20$ | $900 \pm 200$ |
| Sample 9 | $500 \pm 10$ | $1100 \pm 100$ |
| Average | $350 \pm 20$ | $1000 \pm 100$ |

Figure C.6: **In-plane fluctuation analysis to measure material properties.** (**A**) An example of a typical DIC microscopy image seen in experiment. (**B**) Fluctuation spectrum of three membranes, fitted with the expected functional form. (**C**) Table showing the measures of $\gamma$ and $\kappa_B$ for each of the nine samples analyzed.

# Bibliography


[1] L. Onsager, *The effects of shape on the interaction of colloidal particles*, *Annals of the New York Academy of Sciences* **51** (1949).

[2] S. Chandrasekhar and B. K. S. amd K. A. Suresh, *Smectic phase in a colloidal suspension of semiflexible virus particles*, *Pramana* **9** (1977).

[3] L. Wang, D. Huang, L. Lam, and Z. Cheng, *Bowlics: history, advances and applications*, *Liquid Crystals Today* **26** (2017), no. 4 85–111.

[4] L. A. Madsen, T. J. Dingemansand, M. Nakata, and E. T. Samulski, *Thermotropic biaxial nematic liquid crystals*, *Physical Review Letters* **92** (2004).

[5] H. Kikuchi, M. Yokota, H. Y. Yoshiaki Hisakado, and T. Kajiyama, *Polymer-stabilized liquid crystal blue phases*, *Nature Materials* **1** (2002).

[6] F. Jähnig and H. Schmidt, *Hydrodynamics of liquid crystals*, *Annals of Physics* **71** (1972), no. 1 129–166.

[7] A. Buka, P. Palffy-Muhoray, , and Z. Rácz, *Viscous fingering in liquid crystals*, *Physical Review A* **36** (1987).

[8] Q. Zhang, S. Zhou, R. Zhang, and I. Bischofberger, *Dendritic patterns from shear-enhanced anisotropy in nematic liquid crystals*, *Science Advances* **9** (2023).

[9] T. Hirose, K. Ninomiya, S. Nakagawa, and T. Yamazaki, *A guide to membraneless organelles and their various roles in gene regulation*, *Nature Reviews Mollecular Cell Biology* **24** (2023).

[10] D. Bracha, M. T. Walls, and C. P. Brangwynne, *Probing and engineering liquid-phase organelles*, *Nature Biotechnology* **37** (2019).

[11] J. E. Lee, P. I. Cathey, H. Wu, R. Parker, and G. K. Voeltz, *Endoplasmic reticulum contact sites regulate the dynamics of membraneless organelles*, *Science* **367** (2020), no. 6477 eaay7108.

[12] E. Barry, D. Beller, and Z. Dogic, *A model liquid crystalline system based on rodlike viruses with variable chirality and persistence length*, *Soft Matter* **5** (2009).

[13] Z. Dogic and S. Fraden, *Smectic phase in a colloidal suspension of semiflexible virus particles*, *Physical Review Letters* **78** (1997).

[14] E. Barry and Z. Dogic, *Entropy driven self-assembly of nonamphiphilic colloidal membranes*, *Proceedings of the National Academy of Sciences of the United States of America* **107** (2010).

[15] W. Helfrich, *Elastic properties of lipid bilayers: Theory and possible experiments*, *Zeitschrift fur Naturforschung - Section C Journal of Biosciences* **28** (1973).

[16] A. J. Balchunas, R. A. Cabanas, M. J. Zakhary, T. Gibaud, S. Fraden, P. Sharma, M. F. Hagan, and Z. Dogic, *Equation of state of colloidal membranes*, *Soft Matter* **15** (2019).

[17] A. Khanra, L. L. Jia, N. P. Mitchell, A. Balchunas, R. A. Pelcovits, T. R. Powers, Z. Dogic, , and P. Sharma, *Controlling the shape and topology of two-component colloidal membranes*, *Proceedings of the National Academy of Sciences* **119** (2022).

[18] J. M. Miller, C. Joshi, P. Sharma, A. Baskaran, A. Baskaran, G. M. Grason, M. F. Hagan, and Z. Dogic, *Conformational switching of chiral colloidal rafts regulates raft–raft attractions and repulsions.*, *Proceedings of the National Academy of Sciences* **116** (2019).

[19] C. Blanch-Mercader, V. Yashunsky, S. Garcia, G. Duclos, L. Giomi, and P. Silberzan, *Turbulent dynamics of epithelial cell cultures*, *Physical Review Letters* **120** (2018).

[20] J. Toner, Y. Tu, and S. Ramaswamy, *Hydrodynamics and phases of flocks.*, *Annals of Physics* **318** (2005).

[21] C. Dombrowski, L. Cisneros, S. Chatkaew, R. E. Goldstein, and J. O. Kessler, *Self-concentration and large-scale coherence in bacterial dynamics*, *Physical Review Letters* **93** (2004).

[22] W. Wang, X. Lv, J. L. Moran, S. Duana, and C. Zhoua, *A practical guide to active colloids: choosing synthetic model systems for soft matter physics research*, *Soft Matter* **16** (2020).

[23] A. Cavagna and I. Giardina, *Bird flocks as condensed matter*, *Annual Review of Condensed Matter Physics* **5** (2014).

[24] I. Aoki, *A simulation study on the schooling mechanism in fish.*, *Nippon Suisan Gakkaishi* **48** (1982).

[25] V. Soni, E. S. Bililign, S. Magkiriadou, S. Sacanna, D. Bartolo, M. J. Shelley, and W. T. Irvine, *The odd free surface flows of a colloidal chiral fluid*, *Nature Physics* **15** (2019), no. 11 1188–1194.

[26] J. Palacci, S. Sacanna, A. P. Steinberg, D. J. Pine, and P. M. Chaiken, *Living crystals of light-activated colloidal surfers*, *Science* **339** (2013).

[27] N. Kumar, R. Zhang, J. J. D. Pablo, and M. L. Gardel, *Tunable structure and dynamics of active liquid crystals*, *Science Advances* **4** (2018).

[28] P. J. Foster, S. Furthauer, M. J. Shelley, and D. J. Needleman, *Active contraction of microtubule networks.*, *eLife* **4** (2015).

[29] T. Sanchez, D. T. Chen, S. J. Decamp, M. Heymann, and Z. Dogic, *Spontaneous motion in hierarchically assembled active matter*, *Nature* **491** (2012), no. 7424 431–434.

[30] P. M. Bendix, G. H. Koenderink, D. Cuvelier, Z. Dogic, B. N. Koeleman, W. M. Brieher, C. M. Field, L. Mahadevan, and D. A. Weitz, *A quantitative analysis of contractility in active cytoskeletal protein networks*, *Biophysical Journal* **94** (2008).

[31] A. Hunt, F. Gittes, , and J. Howard., *The force exerted by a single kinesin molecule against a viscous load.*, *Biophysical Journal,* **67** (1994).

[32] J. Howard, A. J. Hudspeth, and R. D. Vale, *Movement of microtubules by single kinesin molecules.*, *Nature* **342** (1989).

[33] S. M. Block, L. S. Goldstein, and B. J. Schnapp., *Bead movement by single kinesin molecules studied with optical tweezers.*, *Nature* **348** (1990).

[34] C. L. Asbury, A. N. Fehr, and S. M. Block., *Kinesin moves by an asymmetric hand-over-hand mechanism.*, *Science* **302** (2003).

[35] F. J. Nedelec, T. Surrey, A. C. Maggs, and S. Leibler., *Self-organization of microtubules and motors.*, *Nature* **389** (1997).

[36] L. Giomi, *Geometry and Topology of Turbulence in Active Nematics*, *Physical Review X* **5** (jul, 2015) 31003.

[37] T. Gao, R. Blackwell, M. A. Glaser, M. D. Betterton, and M. J. Shelley, *Multiscale polar theory of microtubule and motor-protein assemblies*, *Physical Review Letters* **114** (2015).

[38] G. Duclos, R. Adkins, D. Banerjee, M. S. E. Peterson, M. Varghese, I. Kolvin, A. Baskaran, R. A. Pelcovits, T. R. Powers, A. Baskaran, F. Toschi, M. F. Hagan, S. J. Streichan, V. Vitelli, D. A. Beller, and Z. Dogic, *Topological structure and dynamics of three dimensional active nematics*, *Science* **367** (2020).

[39] U. Krzic, S. Gunther, T. E. Saunders, S. J. Streichan, and L. Hufnagel, *Multiview light-sheet microscope for rapid in toto imaging*, *Nature Methods* **9** (2012).

[40] R. Adkins, I. Kolvin, Z. You, S. Witthaus, M. C. Marchetti, and Z. Dogic, *Dynamics of active liquid interfaces*, *Science* **376** (2022).

[41] S. Galtier, *Introduction to Modern Magnetohydrodynamics*. Cambridge University Press, 2016.

[42] M. J. Bowick, L. Chandar, E. A. Schiff, and A. M. Srivastava, *The cosmological kibble mechanism in the laboratory: String formation in liquid crystals*, *Science* **263** (1994).

[43] P. Poulin, H. Stark, T. C. Lubensky, and D. A. Weitz, *Novel colloidal interactions in anisotropic fluids*, *Science* **275** (1997).

[44] A. R. Bausch, M. J. Bowick, A. Cacciuto, A. D. Dinsmore, M. F. Hsu, D. R. Nelson, M. G. Nikolaides, A. Travesset, and D. A. Weitz, *Grain boundary scars and spherical crystallography*, *Science* **299** (2003).

[45] W. T. Irvine, V. Vitelli, and P. M. Chaikin, *Pleats in crystals on curved surfaces*, *Nature* **468** (2010).

[46] M. W. Scheeler, W. M. V. Rees, H. Kedia, D. Kleckner, and W. T. Irvine, *Complete measurement of helicity and its dynamics in vortex tubes*, *Science* **357** (2017).

[47] A. Martinez, M. Ravnik, B. Lucero, R. Visvanathan, S. Žumer, and I. I. Smalyukh, *Mutually tangled colloidal knots and induced defect loops in nematic fields*, *Nature Materials* **13** (2014).

[48] U. Tkalec, M. Ravnik, S. Čopar, S. Žumer, and I. Muševič, *Reconfigurable knots and links in chiral nematic colloids*, *Science* **333** (2011).

[49] R. Aditi Simha and S. Ramaswamy, *Hydrodynamic fluctuations and instabilities in ordered suspensions of self-propelled particles*, *Physical review letters* **89** (2002), no. 5 058101, [0108301].

[50] D. Marenduzzo, E. Orlandini, M. E. Cates, and J. M. Yeomans, *Steady-state hydrodynamic instabilities of active liquid crystals: Hybrid lattice boltzmann simulations*, *Physical Review E - Statistical, Nonlinear, and Soft Matter Physics* **76** (2007).

[51] S. Shankar, S. Ramaswamy, M. C. Marchetti, and M. J. Bowick, *Defect unbinding in active nematics*, *Physical Review Letters* **121** (2018).

[52] L. Giomi, M. J. Bowick, P. Mishra, R. Sknepnek, and M. C. Marchetti, *Defect dynamics in active nematics*, *Philosophical Transactions of the Royal Society A: Mathematical, Physical and Engineering Sciences* **372** (2014).

[53] S. P. Thampi, R. Golestanian, and J. M. Yeomans, *Instabilities and topological defects in active nematics*, *EPL* **105** (2014).

[54] X. Q. Shi and Y. Q. Ma, *Topological structure dynamics revealing collective evolution in active nematics*, *Nature Communications* **4** (2013).

[55] V. Narayan, S. Ramaswamy, and N. Menon, *Long-lived giant number fluctuations in a swarming granular nematic*, *Science* **317** (2007).

[56] K. Kawaguchi, R. Kageyama, and M. Sano, *Topological defects control collective dynamics in neural progenitor cell cultures*, *Nature* **545** (2017).

[57] T. B. Saw, A. Doostmohammadi, V. Nier, L. Kocgozlu, S. Thampi, Y. Toyama, P. Marcq, C. T. Lim, J. M. Yeomans, and B. Ladoux, *Topological defects in epithelia govern cell death and extrusion*, *Nature* **544** (2017).

[58] S. Zhou, A. Sokolov, O. D. Lavrentovich, and I. S. Aranson, *Living liquid crystals*, *Proceedings of the National Academy of Sciences of the United States of America* **111** (2014), no. 4 1265–1270.

[59] H. Li, X. qing Shi, M. Huang, X. Chen, M. Xiao, C. Liu, H. Chaté, and H. P. Zhang, *Data-driven quantitative modeling of bacterial active nematics*, *Proceedings of the National Academy of Sciences of the United States of America* **116** (2019).

[60] P. D. G. Jacques Friedel, *Disclination loops in liquid crystals*, *Comptes rendus de l'Académie des Sciences Paris B* (1969).

[61] T. Emeršič, R. Zhang, Žiga Kos, S. Čopar, N. Osterman, J. J. de Pablo, and U. Tkalec, *Sculpting stable structures in pure liquids*, *Science Advances* **5** (2019).

[62] E. M. Terentjev, *Disclination loops, standing alone and around solid particles, in nematic liquid crystals*, *Physical Review E* **51** (1995).

[63] G. P. Alexander, B. G. G. Chen, E. A. Matsumoto, and R. D. Kamien, *Colloquium: Disclination loops, point defects, and all that in nematic liquid crystals*, *Reviews of Modern Physics* **84** (2012).

[64] S. Čopar and S. Žumer, *Quaternions and hybrid nematic disclinations*, *Proceedings of the Royal Society A: Mathematical, Physical and Engineering Sciences* **469** (2013).

[65] S. Čopar, J. Aplinc, Žiga Kos, S. Žumer, and M. Ravnik, *Topology of three-dimensional active nematic turbulence confined to droplets*, *Physical Review X* **9** (2019).

[66] T. N. Shendruk, K. Thijssen, J. M. Yeomans, and A. Doostmohammadi, *Twist-induced crossover from two-dimensional to three-dimensional turbulence in active nematics*, *Physical Review E* **98** (2018).

[67] M. S. Lavine, *Computational modelling of declination loops under shear flow*, *Macromolecular Symposia* **124** (1997).

[68] A. J. Bray, *Theory of phase-ordering kinetics*, *Advances in Physics* **51** (2002), no. 2 481–587.

[69] C. P. Brangwynne, C. R. Eckmann, D. S. Courson, A. Rybarska, C. Hoege, J. Gharakhani, F. Jülicher, and A. A. Hyman, *Germline P granules are liquid droplets that localize by controlled dissolution/condensation*, *Science* **324** (2009), no. 5935 1729–1732.

[70] J. O. Hinze, *Fundamentals of the hydrodynamic mechanism of splitting in dispersion processes*, *AIChE Journal* **1** (1955), no. 3 289–295.

[71] P. Tong, W. I. Goldburg, J. Stavans, and A. Onuki, *Temporal fluctuations in a turbulently stirred binary liquid mixture*, *Physical Review Letters* **62** (1989), no. 23 2668–2671.

[72] L. Berthier, J. L. Barrat, and J. Kurchan, *Phase separation in a chaotic flow*, *Physical Review Letters* **86** (2001), no. 10 2014–2017.

[73] P. Perlekar, R. Benzi, H. J. Clercx, D. R. Nelson, and F. Toschi, *Spinodal decomposition in homogeneous and isotropic turbulence*, *Physical Review Letters* **112** (2014), no. 1 1–5.

[74] M. C. Marchetti, J. F. Joanny, S. Ramaswamy, T. B. Liverpool, J. Prost, M. Rao, and R. A. Simha, *Hydrodynamics of soft active matter*, *Reviews of Modern Physics* **85** (2013), no. 3 1143–1189.

[75] H. H. Wensink, J. Dunkel, S. Heidenreich, K. Drescher, R. E. Goldstein, H. Löwen, and J. M. Yeomans, *Meso-scale turbulence in living fluids*, *Proceedings of the National Academy of Sciences of the United States of America* **109** (2012), no. 36 14308–14313.

[76] H. Soni, W. Luo, R. A. Pelcovits, and T. R. Powers, *Stability of the interface of an isotropic active fluid*, *Soft Matter* **15** (2019), no. 31 6318–6330, [arXiv:1904.0155].

[77] A. E. Patteson, A. Gopinath, and P. E. Arratia, *The propagation of active-passive interfaces in bacterial swarms*, *Nature Communications* **9** (dec, 2018) [arXiv:1805.0642].

[78] S. C. Takatori and A. Sahu, *Active Contact Forces Drive Nonequilibrium Fluctuations in Membrane Vesicles*, *Physical Review Letters* **124** (2020), no. 15 158102, [arXiv:1911.0133].

[79] H. R. Vutukuri, M. Hoore, C. Abaurrea-Velasco, L. van Buren, A. Dutto, T. Auth, D. A. Fedosov, G. Gompper, and J. Vermant, *Active particles induce large shape deformations in giant lipid vesicles*, *Nature* **586** (2020), no. 7827 52–56.

[80] C. M. Caragine, S. C. Haley, and A. Zidovska, *Nucleolar dynamics and interactions with nucleoplasm in living cells*, *eLife* **8** (2019) e47533.

[81] C. Pérez-González, R. Alert, C. Blanch-Mercader, M. Gómez-González, T. Kolodziej, E. Bazellieres, J. Casademunt, and X. Trepat, *Active wetting of epithelial tissues*, *Nature Physics* **15** (2019), no. 1 79–88.

[82] Y. Liu, R. Lipowsky, and R. Dimova, *Concentration dependence of the interfacial tension for aqueous two-phase polymer solutions of dextran and polyethylene glycol*, *Langmuir* **28** (2012), no. 8 3831–3839.

[83] R. Singh and M. E. Cates, *Hydrodynamically Interrupted Droplet Growth in Scalar Active Matter*, *Physical Review Letters* **123** (2019), no. 14 148005, [arXiv:1907.0481].

[84] L. Giomi and A. Desimone, *Spontaneous division and motility in active nematic droplets*, *Physical Review Letters* **112** (2014), no. 14 1–5, [arXiv:1310.1908].

[85] M. L. Blow, S. P. Thampi, and J. M. Yeomans, *Biphasic, lyotropic, active nematics*, *Physical Review Letters* **113** (2014), no. 24 1–5, [arXiv:1407.7493].

[86] D. Langevin, *Light scattering by liquid surfaces and complementary techniques*. M. Dekker, 1992.

[87] D. G. Aarts, M. Schmidt, and H. N. Lekkerkerker, *Direct Visual Observation of Thermal Capillary Waves*, *Science* **304** (2004), no. 5672 847–850.

[88] A. Varshney and V. Steinberg, *Elastic Alfven waves in elastic turbulence*, *Nature Communications* **10** (2019), no. 1 652.

[89] B. Martínez-Prat, R. Alert, F. Meng, J. Ignés-Mullol, J. F. Joanny, J. Casademunt, R. Golestanian, and F. Sagués, *Scaling Regimes of Active Turbulence with External Dissipation*, *Physical Review X* **11** (2021), no. 3 1–16, [arXiv:2101.1157].

[90] J.-F. Joanny and S. Ramaswamy, *A drop of active matter*, *Journal of Fluid Mechanics* **705** (2012) 46–57.

[91] E. Tjhung, A. Tiribocchi, D. Marenduzzo, and M. E. Cates, *A minimal physical model captures the shapes of crawling cells*, *Nature Communications* **6** (2015), no. 1 5420.

[92] Y.-N. Young, M. J. Shelley, and D. B. Stein, *The many behaviors of deformable active droplets*, *Mathematical Biosciences and Engineering* **18** (2021), no. 3 2849–2881.

[93] R. A. Simha and S. Ramaswamy, *Hydrodynamic fluctuations and instabilities in ordered suspensions of self-propelled particles*, *Physical review letters* **89** (2002).

[94] Z. Dogic and S. Fraden, *Development of model colloidal liquid crystals and the kinetics of the isotropic–smectic transition*, *Phil. Trans. R. Soc. A.* **359** (2001).

[95] M. J. Karnovsky, A. M. Kleinfeld, R. L. Hoover, and R. D. Klausner, *The concept of lipid domains in membranes.*, *Journal of Cell Biology* **94** (1982).

[96] T. Gibaud, E. Barry, M. J. Zakhary, M. Henglin, A. Ward, Y. Yang, C. Berciu, R. Oldenbourg, M. F. Hagan, D. Nicastro, R. B. Meyer, and Z. Dogic, *Reconfigurable self-assembly through chiral control of interfacial tension*, *Nature* **481** (2012).

[97] M. Mutz and W. Helfrich, *Bending rigidities of some biological model membranes as obtained from the fourier analysis of contour sections*, *Journal de Physique* **51** (1990).

[98] S. A. Safran, *Statistical thermodynamics of surfaces, interfaces, and membranes*. CRC Press, 2018.

[99] M. Hu, J. J. Briguglio, and M. Deserno, *Determining the gaussian curvature modulus of lipid membranes in simulations*, *Biophysical Journal* **102** (2012).

[100] C. Huang, D. Quinn, Y. Sadovsky, S. Suresh, and K. J. Hsia, *Formation and size distribution of self-assembled vesicles*, *Proceedings of the National Academy of Sciences* **114** (2017).

[101] P. D. Evans, S. N. Cook, P. D. Riggs, and S. Fraden, *Litmus: multipurpose cloning vectors with a novel system for bidirectional in vitro transcription*, *Biotechniques* (1995).

[102] C. E. Ioan, T. Aberle, and W. Burchard, *Light scattering and viscosity behavior of dextran in semidilute solution*, *Macromolecules* **34** (2001).

[103] D. Kumar, C. M. Richter, and C. M. Schroeder, *Conformational dynamics and phase behavior of lipid vesicles in a precisely controlled extensional flow*, *Soft Matter* (2020).

[104] H. Bouvrais, L. Duelund, and J. H. Ipsen, *Buffers affect the bending rigidity of model lipid membranes*, *Langmuir* (2014).

[105] A. Roux, *The physics of membrane tubes: soft templates for studying cellular membranes.*, *Soft Matter* **9** (2013).

[106] T. R. Powers, G. Huber, and R. E. Goldstein, *Fluid-membrane tethers: Minimal surfaces and elastic boundary layers*, *Physical Review E* (2002).

[107] E. Beltrán-Heredia, F.-C. Tsai, S. Salinas-Almaguer, F. J. Cao, P. Bassereau, and F. Monroy, *Membrane curvature induces cardiolipin sorting*, *Communications Biology* **2** (2019).

[108] M. Chabanon, J. C. S. Ho, B. Liedberg, A. N. Parikh, and P. Rangamani, *Thermoelasticity of large lecithin bilayer vesicles*, *Biophysical Journal* **112** (2017).

[109] O. Sandre, L. Moreaux, and F. Brochard-Wyart, *Dynamics of transient pores in stretched vesicles*, *Proceedings of the National Academy of Sciences* (1999).

[110] J. Moroz and P. Nelson, *Dynamically stabilized pores in bilayer membranes*, *Biophysical Journal* (1997).

[111] E. Sackmann, *Membrane bending energy concept of vesicle- and cell-shapes and shape-transitions*, *FEBS Letters* **346** (1994), no. 1 3–16.

[112] M. Castoldi and A. V. Popov, *Purification of brain tubulin through two cycles of polymerization–depolymerization in a high-molarity buffer*, *Protein Expression and Purification* **32** (2003), no. 1 83 – 88.

[113] A. Hyman, D. Drechsel, D. Kellogg, S. Salser, K. Sawin, P. Steffen, L. Wordeman, and T. Mitchison, *Preparation of modified tubulins*, in *Molecular Motors and the Cytoskeleton*, vol. 196 of *Methods in Enzymology*, pp. 478 – 485. Academic Press, 1991.

[114] S. J. DeCamp, G. S. Redner, A. Baskaran, M. F. Hagan, and Z. Dogic, *Orientational order of motile defects in active nematics*, *Nature Materials* **14** (2015) 1110.

[115] D. S. Martin, R. Fathi, T. J. Mitchison, and J. Gelles, *Fret measurements of kinesin neck orientation reveal a structural basis for processivity and asymmetry*, *Proceedings of the National Academy of Sciences* **107** (2010), no. 12 5453–5458, [https://www.pnas.org/content/107/12/5453.full.pdf].

[116] R. Subramanian, E. M. Wilson-Kubalek, C. P. Arthur, M. J. Bick, E. A. Campbell, S. A. Darst, R. A. Milligan, and T. M. Kapoor, *Insights into antiparallel microtubule crosslinking by prc1, a conserved nonmotor microtubule binding protein*, *Cell* **142** (2010), no. 3 433 – 443.

[117] P. Chandrakar, J. Berezney, B. Lemma, B. Hishamunda, A. Berry, K.-T. Wu, R. Subramanian, J. Chung, D. Needleman, J. Gelles, *et. al.*, *Microtubule-based active fluids with improved lifetime, temporal stability and miscibility with passive soft materials*, *arXiv preprint arXiv:1811.05026* (2018).

[118] T. Maniatis, J. Sambrook, and E. Fritsch, *Molecular cloning, a laboratory manual (second edition), volumes 1, 2 and 3.*, *Cold Spring Harbor Laboratory Press* (1989) 623–623.

[119] E. Barry, D. Beller, and Z. Dogic, *A model liquid crystalline system based on rodlike viruses with variable chirality and persistence length*, *Soft Matter* **5** (2009), no. 13 2563–2570.

[120] S. J. Streichan, M. F. Lefebvre, N. Noll, E. F. Wieschaus, and B. I. Shraiman, *Global morphogenetic flow is accurately predicted by the spatial distribution of myosin motors*, *eLife* **7** (2, 2018) e27454.

[121] J. Schindelin, I. Arganda-Carreras, E. Frise, V. Kaynig, M. Longair, T. Pietzsch, S. Preibisch, C. Rueden, S. Saalfeld, B. Schmid, J.-Y. Tinevez, D. J. White, V. Hartenstein, K. Eliceiri, P. Tomancak, and A. Cardona, *Fiji: an open-source platform for biological-image analysis*, *Nature Methods* **9** (2012) 676.

[122] S. Preibisch, F. Amat, E. Stamataki, M. Sarov, R. H. Singer, E. Myers, and P. Tomancak, *Efficient bayesian-based multiview deconvolution*, *Nature Methods* **11** (2014) 645—-648.

[123] R. Rezakhaniha, A. Agianniotis, J. T. C. Schrauwen, A. Griffa, D. Sage, C. V. C. Bouten, F. N. van de Vosse, M. Unser, and N. Stergiopulos, *Experimental investigation of collagen waviness and orientation in the arterial adventitia using confocal laser scanning microscopy*, *Biomechanics and Modeling in Mechanobiology* **11** (2012), no. 3-4 461.

[124] A. Lozano-Durán and G. Borrell, *Algorithm 964: an efficient algorithm to compute the genus of discrete surfaces and applications to turbulent flows*, *ACM Transactions on Mathematical Software (TOMS)* **42** (2016), no. 4 34.

[125] J. Toriwaki and T. Yonekura, *Euler number and connectivity indexes of a three dimensional digital picture*, *Forma* **17** (2002), no. 3 183–209.

[126] M. Kleman and J. Friedel, *Disclinations, dislocations, and continuous defects: A reappraisal*, *Reviews of Modern Physics* **80** (2008), no. 1 61.

[127] G. P. Alexander, B. G.-g. Chen, E. A. Matsumoto, and R. D. Kamien, *Colloquium: Disclination loops, point defects, and all that in nematic liquid crystals*, *Reviews of Modern Physics* **84** (2012), no. 2 497.

[128] K. Jänich, *Topological properties of ordinary nematics in 3-space*, *Acta Applicandae Mathematica* **8** (1987), no. 1 65–74.

[129] S. Čopar and S. Žumer, *Quaternions and hybrid nematic disclinations*, *Proceedings of the Royal Society A: Mathematical, Physical and Engineering Science* **469** (2013), no. 2156 20130204.

[130] L. Tran, M. O. Lavrentovich, D. A. Beller, N. Li, K. J. Stebe, and R. D. Kamien, *Lassoing saddle splay and the geometrical control of topological defects*, *Proceedings of the National Academy of Sciences* **113** (2016), no. 26 7106–7111.

[131] A. Ward, F. Hilitski, W. Schwenger, D. Welch, A. W. C. Lau, V. Vitelli, L. Mahadevan, and Z. Dogic, *Solid friction between soft filaments*, *Nature Materials* **14** (2015), no. 6 583–588.

[132] T. M. Squires and T. G. Mason, *Fluid Mechanics of Microrheology*, *Annual Review of Fluid Mechanics* **42** (dec, 2009) 413–438.

[133] Y. Gidi, S. Bayram, C. J. Ablenas, A. S. Blum, and G. Cosa, *Efficient One-Step PEG-Silane Passivation of Glass Surfaces for Single-Molecule Fluorescence Studies*, *ACS Applied Materials & Interfaces* **10** (nov, 2018) 39505–39511.

[134] T. Sanchez and Z. Dogic, *Chapter Twelve - Engineering Oscillating Microtubule Bundles*, in *Cilia, Part A* (W. F. B. T. M. i. E. Marshall, ed.), vol. 524, pp. 205–224. Academic Press, 2013.

[135] A. M. Tayar, L. M. Lemma, and Z. Dogic, *Assembling Microtubule-Based Active Matter*, .

[136] A. Ciomaga, P. Monasse, and J.-M. Morel, *The Image Curvature Microscope: Accurate Curvature Computation at Subpixel Resolution*, *Image Processing On Line* **7** (2017) 197–217.

[137] W. Thielicke and R. Sonntag, *Particle Image Velocimetry for MATLAB: Accuracy and enhanced algorithms in PIVlab*, *J. Open Res. Softw.* **9** (2021), no. 1.

[138] C. W. Hirt and B. D. Nichols, *Volume of fluid (VOF) method for the dynamics of free boundaries*, *Journal of Computational Physics* **39** (1981), no. 1 201–225.

[139] J. U. Brackbill, D. B. Kothe, and C. Zemach, *A continuum method for modeling surface tension*, *Journal of Computational Physics* **100** (1992), no. 2 335–354.

[140] P. Srivastava, P. Mishra, and M. C. Marchetti, *Negative stiffness and modulated states in active nematics*, *Soft Matter* **12** (2016), no. 39 8214–8225.

[141] S. Santhosh, M. R. Nejad, A. Doostmohammadi, J. M. Yeomans, and S. P. Thampi, *Activity Induced Nematic Order in Isotropic Liquid Crystals*, *Journal of Statistical Physics* **180** (2020), no. 1 699–709.

[142] P. G. De Gennes and J. Prost, *The physics of liquid crystals*. Clarendon Press, 2 ed., 1993.

[143] F. Moukalled, L. Mangani, and M. Darwish, *The Finite Volume Method in Computational Fluid Dynamics*. Fluid Mechanics and Its Applications. Springer International Publishing, 2016.

[144] S. S. Deshpande, L. Anumolu, and M. F. Trujillo, *Evaluating the performance of the two-phase flow solver interFoam*, *Computational Science & Discovery* **5** (2012), no. 1 14016.

[145] S. Safran, *Statistical Thermodynamics of Surfaces, Interfaces, and Membranes (1st ed.)*. CRC Press, 2003.

[146] M. Grant and R. C. Desai, *Fluctuating hydrodynamics and capillary waves*, *Physical Review A* **27** (may, 1983) 2577–2584.

[147] J. L. Harden, H. Pleiner, and P. A. Pincus, *Hydrodynamic surface modes on concentrated polymer solutions and gels*, *The Journal of Chemical Physics* **94** (apr, 1991) 5208–5221.

[148] E. G. Flekkøy and D. H. Rothman, *Fluctuating Fluid Interfaces*, *Physical Review Letters* **75** (jul, 1995) 260–263.

[149] E. G. Flekkøy and D. H. Rothman, *Fluctuating hydrodynamic interfaces: Theory and simulation*, *Physical Review E* **53** (feb, 1996) 1622–1643.

[150] A. J. Bray, A. Cavagna, and R. D. M. Travasso, *Interface fluctuations, Burgers equations, and coarsening under shear*, *Physical Review E* **65** (dec, 2001) 16104.

[151] A. Doostmohammadi, J. Ignés-Mullol, J. M. Yeomans, and F. Sagués, *Active nematics*, *Nature Communications 2018 9:1* **9** (aug, 2018) 1–13.

[152] D. A. Gagnon, C. Dessi, J. P. Berezney, R. Boros, D. T. Chen, Z. Dogic, and D. L. Blair, *Shear-Induced Gelation of Self-Yielding Active Networks*, *Physical Review Letters* **125** (oct, 2020) 178003, [arXiv:2004.0733].

[153] H. Kimura and H. Nakano, *Statistical Theory of Surface Tension and Molecular Orientations at the Free Surface in Nematic Liquid Crystals*, *Journal of the Physical Society of Japan* **54** (may, 1985) 1730–1736.

[154] M. L. Blow, M. Aqil, B. Liebchen, and D. Marenduzzo, *Motility of active nematic films driven by "active anchoring"*, *Soft Matter* **13** (2017), no. 36 6137–6144.

[155] R. C. V. Coelho, N. A. M. Araújo, and M. M. Telo da Gama, *Director alignment at the nematic–isotropic interface: elastic anisotropy and active anchoring*, *Philosophical Transactions of the Royal Society A: Mathematical, Physical and Engineering Sciences* **379** (oct, 2021) 20200394.

[156] J. C. Berg, *An introduction to interfaces and colloids: the bridge to nanoscience*. World Scientific, 2010.

[157] E. Wood, *Molecular cloning. a laboratory manual*, *Biochemical Education* **11** (1983).

[158] M. J. Zakhary, T. Gibaud, C. N. Kaplan, E. Barry, R. Oldenbourg, R. B. Meyer, and Z. Dogic, *Imprintable membranes from incomplete chiral coalescence*, *Nature Communications* (2014).

[159] A. W. C. Lau, A. Prasad, and Z. Dogic, *Condensation of isolated semi-flexible filaments driven by depletion interactions*, *Europhysics Letters* **87** (2009).

[160] C. Steger, *An unbiased detector of curvilinear structures.*, *EEE Transactions on Pattern Analysis and Machine Intelligence* **20** (1998).

[161] P. Cignoni, M. Callieri, M. Corsini, M. Dellepiane, F. Ganovelli, and G. Ranzuglia, *MeshLab: an Open-Source Mesh Processing Tool*, in *Eurographics Italian Chapter Conference* (V. Scarano, R. D. Chiara, and U. Erra, eds.), The Eurographics Association, 2008.

[162] U. Seifert, *Configurations of fluid membranes and vesicles*, *Advances in Physics* **46** (1997), no. 1 13–137.

[163] L. L. Jia, M. J. Zakhary, Z. Dogic, R. A. Pelcovits, and T. R. Powers, *Chiral edge fluctuations of colloidal membranes*, *Physical Review E* **95** (2017).

[164] F. Jülicher and U. Seifert, *Shape equations for axisymmetric vesicles: A clarification.*, *Physical Review E* **49** (1994).